HIGHER-ORDER INTERACTION INHIBITS BACTERIAL INVASION OF A PHOTOTROPH-PREDATOR MICROBIAL COMMUNITY

BY

HARRY MICKALIDE

DISSERTATION

Submitted in partial fulfillment of the requirements
for the degree of Doctor of Philosophy in Physics
in the Graduate College of the
University of Illinois at Urbana-Champaign, 2019

Urbana, Illinois

Doctoral Committee:

Professor Yann Chemla, Chair
Assistant Professor Seppe Kuehn, Director of Research
Professor Karin Dahmen
Associate Professor James O'Dwyer

Abstract

The composition of an ecosystem is thought to be important for determining its resistance to invasion. Studies of natural ecosystems, from plant to microbial communities, have found that more diverse communities are more resistant to invasion. It is thought that more diverse communities resist invasion by more completely consuming the resources necessary for invaders. Here we show that *Escherichia coli* can successfully invade cultures of the alga *Chlamydomonas reinhardtii* (phototroph) or the ciliate *Tetrahymena thermophila* (predator), but cannot invade a community where both are present. The invasion resistance of the algae-ciliate community arises from a higher-order (3-way) interaction that is unrelated to resource consumption. We show that the mechanism of this interaction is the algal inhibition of bacterial aggregation which leaves bacteria vulnerable to ciliate predation. This mechanism requires both the algae and the ciliate to be present and provides an example of invasion resistance through a trait-mediated higher-order interaction.

In a separate project we explore how the environment determines evolutionary trajectory when there exists a trade-off between beneficial traits. We select *Escherichia coli* for faster migration through a porous environment, a process which depends on both motility and growth. Evolving faster migration in rich medium results in slow growth and fast swimming, while evolution in minimal medium results in fast growth and slow swimming. Given that both fast growth and fast swimming would enhance migration rate, this result suggests that there is a trade-off between these two phenotypes and that the direction of evolution depends on the environment.

Acknowledgements

First and foremost, I would like to thank my parents, Tinker and Mark Mickalide. Having a nurturing home environment through childhood is a treasure that cannot be measured. My eternal gratitude to them for providing for me, to my dad for teaching me to think critically, and to my mom for giving me abundant love.

Thank you to Seppe Kuehn for investing untold time and soul into our projects. His breadth of knowledge and incredible experimental skill is a constant reminder of how much I have to grow as a scientist. His dedication to the science never ceases to inspire me.

Thank you to all the members of Kuehn lab over the years for taking this ride with me. I sat across from Jason Merritt for years and so probably spent more time with him in grad school than anyone else, sharing countless jokes and opinions. Much gratitude to him for all the time he spent helping me with computers and electronics. My custom-culture devices are based almost entirely on his design. May he find success in data science or whatever career he chooses. Thank you to David Fraebel for making the *E. coli* migration project a reality with me. Thank you to Diane Schnitkey for bringing kindness and a tenacious work ethic to the lab, and also helping with the *E. coli* migration project. Thank you to Joey Varikooty for helping design the electronics of the custom-culture devices. Thank you to Derek Ping for his adventurous spirit, both in science and in the very experience of consciousness. Karna Gowda is the rare soul who is centered enough to both be very serious in his pursuit of truth, but always warm and approachable. I thank him for all the help he has given me in the lab. Thank you to Chandana Gopalakrishnappa for brightening up every room she walks into and for the hard work she puts into the droplet project. Thank you to Kaumudi Prabhakara for fielding my strange thoughts with a smile and also for her commitment to the scientific path. Thank you to Luis Miguel de

Jesus Astacio for the good times and for continuing the legacy of the custom-culture devices.

Many thanks to all the friends I have made in Urbana-Champaign and shared the ups and downs with, the laughter and the tears. The people of this program and this town have painted my experience through and through with color. It feels like I have spent a lifetime in this town, so much has happened.

Thank you to the committee members for my prelim: James O'Dwyer, Seppe Kuehn, Yann Chemla, and Rachel Whitaker. Their suggestions set me on track and have made me a better scientist. Thank you to Karin Dahmen for stepping in and joining the committee for my thesis defense.

Additionally I would like to thank Betty Ujhelyi for helping a lot around the lab and Barbara Pilas for helping getting the flow cytometry measurements working.

To mom and dad

Table of Contents

Chapter 1

Introduction

1.1 The search for a general theory of ecology

Why study ecology? The Earth's ecosystem is an extraordinarily rich system, the study of which has the potential to yield many new insights. More importantly, however, a deep understanding of the principles that govern ecosystems would translate into better techniques and policies for preserving ecosystems, which is needed crucially right now. Even when using conservatively low and high estimates respectively for the current extinction rate and the background extinction rate, scientists calculate that humans have increased the extinction rate by 100 times [1]. The sixth mass extinction on Earth is underway [1] and presents a problem on the same scale as climate change. Interestingly, while climate change is usually framed as a problem that is just beginning to affect us, when it comes to mass extinction, most of the damage has already been done. Scientists estimate that between 1970 and 2010, total vertebrate populations on Earth decreased by 60% [2]. Such massive loss of life constitutes a profound crime by humans against animals. Moreover, a Millenium Assessment determined that"everyone in the world depends completely on Earth's ecosystems" [3] and so the mass extinction presents an existential threat to our own species.

Engineering solutions to this problem are underway. Based on studies which show that fungi restore the health of the soil [4],conservationists are using mushrooms to help reforest areas [5]. Based on studies which show that indigenous bacteria helped degrade the oil spilled by BP in the Gulf of Mexico [6], trials are underway in India to introduce bacteria to clean the River Ganga [7]. Currently, these conservation efforts operate by trial-and-error. There is no general theory to predict the results of these efforts.

A general theory would help guide conservation efforts and provide answers to fun-

damental question in ecology. For example, in order to cultivate a healthy ecosystem, is it better to add nutrients to support the growth of indigenous species as is commonly done in reforestion [8], or to remove nutrients so as to prevent invasive species from taking over [9]? Apex predators have been introduced into forests [10] due to their known beneficial effects [11], but what interspecies interactions cause them to stabilize ecosystems? If a network model is the correct framework, are ecosystems more sensitive to loss of species that form hubs or that have few connections [12]? Answers to these questions have been found in specific cases, but there is not general theory that can provide the answer for arbitrary species and environmental inputs. One goal of my research has been to help get closer to developing such a general quantitative theory and I believe it is this goal which situates the study of ecology in a physics department.

Development and testing of ecological models has mostly been limited to case studies and for good reason. The full complexity of Earth's ecosystem, billions of species, multiple climates and biomes, changing seasons, etc. necessitates that we limit ourselves to case studies for now. The question then becomes: at what scale should we conduct these case studies? I will focus on microbial ecology and highlight two scales of experiments and outline their advantages and disadvantages (1) natural communities where abundance measurements are typically performed with metagenomic sequencing, where the actual number of species present is unknown, and where the environment is uncontrolled and (2) laboratory communities where abundance measurements are typically performed with flow cytometry, plating, or imaging, where the number of species is small and known, and where the environment (e.g. growth media, temperature, and light level) is tightly controlled.

1.2 Scale 1: natural microbial communities

The primary advantage of working at scale (1) is that the system is a true representation of nature both in that it comes from nature and engages with the complexity of a natural ecosystem, or at least the microbial part of it. To measure abundances of organisms, one can use metagenomic sequencing. This process involves sequencing all the DNA from a sample and then mapping each sequence of 16S rRNA to a genus.

Pioneering work by Carl Woese showed that distance between 16S rRNA sequences is a good measure of evolutionary time and thus 16S rRNA can be used to build phylogenetic taxonomies [13]. Consequently, the 16S rRNA sequence of an organism can be accurately mapped to its genus. Abundances of different genuses (or operational taxonomic units depending on to what degree we coarse grain taxonomy) can then be estimated from abundances of corresponding 16S rRNA sequences. Abundances of genes in a community can also be estimated from metagenomic sequencing.

However, since the technique is purely genetic, there is no information about those aspects of the phenotype which are not determined by genetics but instead by the environment or interactions with other species. Additionally, many assumptions must be made when relying on metagenomics, such as total community abundance being constant [14], the gene database which sequences are annotated against being mostly complete [15], and that the DNA survives the lysis procedure at an equal rate for different species [16]. The other disadvantage of working at scale (1) is that the scientist controls nothing about the environment or the community, which introduces an unknown number of unknowns and also makes any experiment impossible to truly replicate.

Despite these limitations, many encouraging discoveries have been made when working at this scale. Namely, there is encouraging work on the topic of "functional redundancy", the ability of multiple microbes to perform the same function. Functional redundancy has the potential to drastically reduce the effective complexity of an ecosystem by collapsing the effects of many species to just a handful of functions performed by those species. The simplification provided by functional redundancy may be an important step in building a general theory of ecology. One study analyzed microbial communities sampled from the ocean and showed that environmental parameters were a better predictor of the function of those communities than they were of the taxonomic makeup [17]. Another study showed that bacterial communities sampled from the surfaces of macroalgae were much more similar in function than in taxonomy [18]. They attributed the seeming irrelevance of which actual species perform the function to a neutral lottery model. Others have disputed the relevance of neutral theory to functional redundancy, stating that cell densities are high enough that even small competitive differences lead to natural selection, thus making neutral

theory inapplicable [19].

1.3 Scale 2: laboratory microbial communites

Scale (2), working with only a handful of species in a controlled laboratory setting, is where I have chosen to do the bulk of my graduate work. The disadvantage of working at this scale is that the complexity of the system is absurdly small when compared to nature. The advantage is that this simplicity allows one to make controlled measurements of both abundance and phenotype of the chosen species in any combination. For example, by performing flow cytometry measurements on a community with three species, I perform experiments in monoculture, pairculture, and triculture, and gather accurate data on abundance, size, and fluorescence through time. Having this all this information ends up being crucial for the the conclusions I draw. Similarly, through careful measurements of both aggregation phenotype and abundance, one study was able to show how variation in a heritable phenotype (aggregation) determines abundance dynamics in a model algae-rotifer community [20]. Another study measures abundances, nutrients, and gene expression in a 3-species synthetic gut community, and in so doing makes decisive conclusions about cross-feeding, nutrient competition, and transcription interactions between specific species [21].

Working at scale (2), having a tractable number of species and accurate abundance measurements, is often necessary for testing the quantitative differential equation models that form much of theoretical ecology [20, 21]. The most common model in theoretical ecology is Lotka-Volterra, which in its generalized form appears as follows

$$\dot{x}_i = r_i x_i + \sum_{j=1}^{n} \alpha_{ij} x_i x_j \tag{1.1}$$

where x_i is the abundance of the ith organism, r_i is its growth rate, and $\dot{x}_i$ is the time derivative of its abundance. α_{ij} represents the strength of the interaction between the ith and jth organisms. By making α_{ii} negative, one would recapitulate logistic growth for the ith organism in the absence of other species. Robert May performed pioneering work in theoretical ecology in 1973 when he published "Stability and complexity in model ecosystems" and used the Lotka-Volterra model

to quantify relationships between different ecosystem properties [22]. For example, by using randomly constructed community matrices (the community matrix being the linearization of the Lotka-Volterra model around a fixed point [23]) he showed that the complexity of an ecosystem (number of species, number of interactions, and strength of interactions) is inversely proportional to the stability of that ecosystem (ability to return to equilibrium after perturbation). The relevance of these conclusions is of course dependent on Lotka-Volterra models with randomly constructed community matrices being accurate representations of natural communities. Forms of Lotka-Volterra have been validated with a model community of four ciliates [24], with a gut microbiome [14], and with a lynx-hare system [25].

There are, however, severe limitations to Lotka-Volterra. There are many cases in which the product of species abundances would not accurately reflect the interaction strength between those two species. For example, this product form would not apply if predators interfered with each other at high predator density [26], or, oppositely, if predators exhibited an Allee effect and preyed more efficiently at high densities [27]. One study showed that Lotka-Volterra is a poor fit for abundances simulated from mechanistic resource models, even when there are only two species and one resource [28].

1.4 Higher-order interactions

Another limitation of Lotka-Volterra, and the one I will focus on, is that there are no higher-order interactions. For higher-order interaction, I use the definition provided by Peter Abrams: "whenever one species affects the nature of the interaction between two others" [29]. Lotka-Volterra has no terms that depend on the abundance of more than two organisms and therefore has no higher-order interactions. An example of a higher-order interaction would be barnacles affecting the nature of the interaction between birds and limpets (aquatic snails): the barnacles blend in with the limpets, making the limpets less visible to birds, and thus reducing the predation of the birds on the limpets [30].

Worthen et al. [31] are careful to distinguish between higher-order interactions and indirect effects. An indirect effect is defined as a change in the outcome of a pairwise

interaction due to a third species. For example, when wolves prey on elk, they reduce elk populations and consequently reduce overall herbivory of elk on vegetation, thus increasing vegetation [10]. Crucially, even though the wolves have indirectly increased the vegetation, the wolves have not changed the nature of the interaction between elk and vegetation, and thus this situation does not constitute a higher-order interaction. Abundances of species through time must be measured in order to distinguish indirect effects from true higher-order interactions [31].

It is an open question of how common higher-order interactions are in nature and consequently how necessary it is to implement them in models. Multiple studies have shown models without higher-order interactions to work well [14, 24, 25], but in all these cases, either only two species were studied, or species came from the same trophic level and likely interacted primarily through nutrient competition. Antagonistic interactions common in nature, like predation and antibiotics, were mostly absent in these communities.

Some studies, like those that follow, have in fact detected higher-order interactions. A study of birds, limpets (aquatic snails), and barnacles found a higher-order interaction [30]. One study found that there were higher-order interactions in natural plant communities [32]. They based their conclusion on the better agreement between experiment and model they obtained when adding higher-order terms to their model. Since more terms will always make for better agreement, the conclusion of this study relies critically on having a correct measure of parsimony (the degree of improvement in model-experiment agreement necessary to justify additional terms). One study found higher-order interactions by testing and rejecting pairwise Lotka-Volterra models, a result which could also be explained by the Lotka-Volterra model having the wrong form of pairwise interaction term [33]. Another study found higher-order interactions in the function of starch hydrolysis [34]. They grew seven species of soil bacteria in various monoculture, pairwise, and higher combinations and, after a day of growth, filtered out the cells and measured the capability of the supernatant to hydrolize starch. They found that starch hydrolysis levels of combinations of three or more species were not predicted by starch hydrolysis levels of monoculture and pairwise combinations of bacteria, and thus concluded the existence of higher-order interactions. This conclusion is limited by the fact that the authors did not measure

species abundances after growth. Indirect effects or crossfeeding or nutrient competition between species could have changed final abundances relative to monoculture or pairculture and have consequently changed the level of starch hydrolysis relative to monoculture or pairculture. Crossfeeding and nutrient competition do not constitute higher-order interactions. .

In addition to asking how common are higher-order interactions, we must also ask how important they are. Do the presence of higher-order interactions qualitatively change predictions about global ecosystem properties like stability? Tentatively, the answer is yes. Two studies on models with higher-order interactions show increased complexity leading to increased stability, the opposite relationship derived for pairwise models. [35, 36] In both studies, higher-order interaction terms were assumed to be of product form, for example $\alpha_{123}x_1x_2x_3$ for an interaction of order 3 where x_1, x_2, and x_3 are the abundances of three organisms and α_{123} is the interaction strength between them. This term would show up in the differential equation for one of the three organisms, for example $\dot{x}_1$

Taking the points of the last few paragraphs together, in an ideal system for studying higher-order interactions we would (1) have more than two species, (2) have species from different trophic levels in order to widen the scope of interactions beyond nutrient competition, (3) take phenotypic measurements in order to determine the mechanism of higher-order interactions, and (4) measure abundances of the community in all possible combinations of species in order to distinguish higher-order interactions from indirect interactions and nail down the exact the mathematical form of the differential equations for species abundances. The experiments I perform with the ABC ecosystem fit all these criteria. The ABC ecosystem consists of the algae *C. reinhardtii* (A), the bacteria *E. coli* (B), and the ciliate *T. thermophila* (C). Respectively, these species are producers, decomposers, and predators, and thus represent different trophic levels. Communities of these species were cultured in all possible combinations. Abundance data and aggregation phenotype data were gathered with flow cytometry. With this dataset, we were able to discover and model a higher-order interaction: A inhibits B aggregation and in so doing increases predation pressure of C on B. Aggregation is B's primary defense mechanism against predation.

This higher-order interaction can prevent the invasion of B into an AC community.

We have therefore uncovered a mechanism for resistance of a microbial community to invasion. Microbial invasions are a worthy object of study in their own right, as a fundamental understanding of them is necessary for successfully designing industrial processes such as algal biofuel production [37] or controlling harmful invasions in nature such as microbial blooms [38].

1.5 Microbial invasions

A hypothesis in microbial ecology states that "everything is everywhere, but the environment selects." [39] Under this hypothesis most microbial species are present in most environments, and it is the particular qualities of a local environment that determine which species establish themselves. This hypothesis is supported by studies in oceans [40] and streams [41] which show that the composition of microbial communities is better predicted by local environmental variables than spatial location [42].

The observation that local environmental variables strongly predict community composition suggest that rates of dispersal are high, and indeed from active transport like motility [43] to passive transport like wind [44] and water currents, there are many mechanisms by which microbes disperse. Moreover, rapid dispersal suggests persistent immigration of microbes into new communities. Whether or not a given species successfully invades and establishes itself when encountering a new environment depends not just on the environment, but also on the invasion resistance of the local microbial community. Therefore, understanding the mechanisms of invasion resistance in microbial communities is central to understanding the structure of microbial communities in nature.

Our current understanding of when and why some invasions succeed and others fail is grounded in the idea that an invader must either outcompete an existing community member for an available resource (dominance) or consume a resource that is not already being consumed by the community (complementarity) [45]. Dominance and complementarity have successfully explained the outcome of invasions in a wide range of studies. For example, in laboratory populations of *Pseudomonas fluorescens*, more diverse communities resisted invasion more effectively by more completely occupying the available niches [46]. Qualitatively similar results were observed for *E.*

coli invasions of soil communities [47], wherein diversity of and resource consumption by the community were positively correlated with invasion resistance. Similarly, studies of plant root bacterial communities demonstrated that community resource competition networks could reliably predict the outcome of invasions both *in vitro* and in tomato plant root communities [48]. Similar results have been found for plant communities on a larger spatial scale [49].

Recently, theoretical work using consumer-resource models has extended this intuition and suggested that the emergent resource consumption and exchange in cross-feeding communities can be understood as a community-level fitness which provides cohesiveness and therefore invasion resistance [50]. Experimental efforts suggest that this picture can capture some features of experimental invasions in bacterial communities [51]. Collectively, this work shows that substantial insight into invasion dynamics can come from understanding resource dynamics during an invasion process.

However, in nearly all microbial communities there exist interactions that are not directly mediated by resources: for example, antagonistic interactions such as the excretion of antibiotics [52] and predation by protists [53] or phage [54]. A handful of studies have examined the role these interactions play in determining the fate of invading species [55], but, as recently pointed out by Mallon *et al.* [56], it remains an outstanding question how antagonistic interactions affect community invasion dynamics.

Here we use a model microbial community to study invasion dynamics in the presence of antagonistic interactions. Microbial communities in freshwater lakes and nearby saturated soils are occupied by primary producers who fix inorganic carbon, metabolically flexible heterotrophic bacteria who decompose organic matter, and predators who unlock nutrients held in biomass [57]. To study this canonical natural community, we use a three-species model microbial ecosystem comprised of the alga *Chlamydomonas reinhardtii* which acts as a primary producer and is an endemic phototroph in soils and freshwater [58], the bacterium *Escherichia coli* which acts as a decomposer and is common in soils [59], and the ciliate *Tetrahymena thermophila* which dwells in freshwater and preys on *E. coli*. We refer to this model ecosystem as the 'ABC' community for **A**lgae, **B**acteria and **C**iliates. The ABC community has been studied previously as a model self-sustaining closed microbial ecosystem [60–62].

Recent work has shown that long-term abundance dynamics in closed ABC ecosystems are complex and deterministic on timescales of months, exhibiting rich spatio-temporal and phenotypic dynamics [61]. The fact that the composition of the ABC community reflects the structure of some natural communities and that quantitative measurements are feasible make this a compelling model ecosystem for quantitative ecology [63].

Here we show that when *E. coli* (B) is introduced into communities of *C. reinhardtii* (A) and *T. thermophila* (C), a higher order (3-way) interaction determines the outcome of the invasion. When B invades C alone, B aggregates to avoid predation by C and successfully grows to high density. Similarly, when B invades A alone, A may stall the invasion of B, but B can still successfully invade and grow to high density. In contrast, when B is introduced into a community of C and high-density A ($> 5 \times 10^4\,\mathrm{mL}^{-1}$), B always fails to invade. We demonstrate that nutrient competition is not responsible for the invasion dynamics we observe. Instead, we find that A inhibits aggregation of B, resulting in increased predation pressure on B by C and therefore a decline in B abundances.

Chapter 2

Discovery and modeling of a higher-order interaction in the ABC community

We study the dynamics of the ABC community in batch culture conditions with the community open to gas exchange. Organisms are introduced at low initial densities into 30mL of a freshwater mimic medium [64] with undefined carbon and nitrogen sources (proteose peptone No. 3, see Methods). To initiate an experiment, all three organisms are cultured axenically in their respective growth media. Cells are washed and then their densities determined by flow cytometry. The communities are then constructed with known initial starting densities and maintained in custom culture devices which control temperature via feedback to a Peltier element (30 °C) and illumination via an LED below the vial (Fig. 2.1a).

Here we present two types of experiments: co-culture experiments and invasion experiments. Co-culture refers to experiments in which all species are simultaneously introduced at low densities ($1 \times 10^3\,\mathrm{mL}^{-1}$ for A, $5 \times 10^2\,\mathrm{mL}^{-1}$ for B, and $5 \times 10^2\,\mathrm{mL}^{-1}$ for C) and in all possible monoculture, pair-culture, and tri-culture combinations. Invasion refers to experiments in which A and/or C is introduced at low density, allowed to grow for a fixed period of time (4 or 14 days), and then inoculated with B. In all experiments, abundance dynamics are followed approximately daily by sampling 500 µL of the community and performing flow cytometry measurements. Flow cytometry permits the quantification of abundances for A, B and C by chlorophyll fluorescence, genetically encoded yellow-fluorescent protein (YFP) fluorescence and size respectively (see Methods). Since a significant number of B cells are present in aggregates, we apply an aggregate correction algorithm (see chapter 3) to estimate the true abundance of B cells and that is what we report in this study. We varied A's growth rate by performing experiments at two light levels: 'low light' (average intensity of 1600 Lux) or 'high light' (average intensity of 4200 Lux). Abundance dynamics of B and C are not altered by illumination over this range of intensities

(Fig. 3.1c&d, Fig. 3.8a). Communities are mixed by a magnetic stirrer at a rate of 450 rpm and sampled through a sterile port.

2.1 Monoculture and pair-culture dynamics.

To begin, we measured monoculture and pair-culture dynamics in the high light condition (Fig. 2.1). pair-culture dynamics between A and B suggest limited impact of A on B growth rate or carrying capacity (Fig. 2.1b,c,f). Similarly, B does not measureably impact A growth rate or carrying capacity in this high light condition (Fig. 3.1b).

In contrast, when B is pair-cultured with C, we observe an approximately 10-fold reduction in the abundances of B relative to B monoculture. This reduction is expected due to the known predation of B by C. In these BC pair-cultures, predation of B by C fails to drive B abundances below approximately $10^5\,\mathrm{mL}^{-1}$ and at longer times B abundances increase (Fig. 2.1h). Previous measurements of ciliate feeding rates [65], however, suggest that at these densities, C should be able consume most of the B present (see chapter 3). We propose that the ability of B to sustain comparatively high densities in the presence of C is driven by B aggregation [66]. Bacterial aggregation is a common defense against predation due to the fact that the oral apparatus of the ciliates has a limited range of prey sizes it can accommodate [67, 68]. Sufficiently large aggregates of B cannot be consumed by C. Indeed, we show that B aggregates much more in the presence of C than in monoculture (Fig. 2.1e). B aggregation was quantified by side-scatter measurements (Fig. 3.2). We conclude that B abundances are reduced by predation but the impact of predation is limited by aggregation. We also note that C abundances are not substantially impacted by the presence of B. This fact is in accordance with the low yield of ciliates on bacteria since previous work suggests 1×10^3 to 4×10^4 bacteria are required to produce a single ciliate (see chapter 3).

Finally, when A and C are pair-cultured, the dynamics of C are minimally impacted relative to C monoculture (Fig. 2.1d,g). Taken together, Fig. 2.1 suggests that the dominant interaction in the ABC community is predation of B by C while interactions between A and B or A and C are limited.

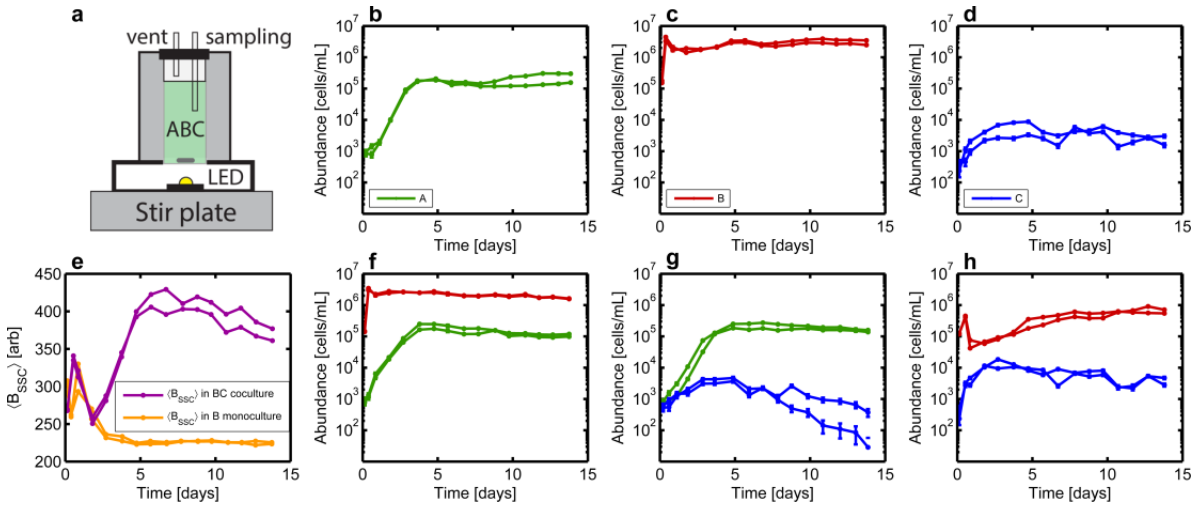

Figure 2.1: **Monoculture and pair-culture dynamics with algae, bacteria, and ciliates. a,** A schematic of the custom culture devices used in this study. **b-d,** Abundance dynamics plotted for monocultures of algae (A), bacteria (B), and ciliates (C) respectively at 4200 Lux (high light). **f-h,** Abundance dynamics for AB, AC, and BC pair-culture respectively, also at 4200 Lux. For each experiment there are two independent replicates. Abundances are measured via flow cytometry. Error bars are computed as described in Methods. For time points where error bars are not visible, errors are smaller than the size of the points. B abundances are reported as the total number of cells including planktonic cells and cells in aggregates as calculated with an aggregate correction algorithm described in chapter 3. **e**, Mean side-scatter signal of B as a function of time in B monoculture and BC pair-culture.

2.2 Bacterial invasions of ciliates.

We studied the dynamics of B invading C. We introduced B at a density of $\sim 1 \times 10^4\,\mathrm{mL}^{-1}$ into established cultures of C 4 and 14 days after the initiation of C cultures (Fig. 2.2a,d,g). We find that irrespective of the timing of the introduction of B or the light levels, B successfully grows to high densities ($> 1 \times 10^5\,\mathrm{mL}^{-1}$). As in BC pair-culture (Fig. 2.1e), side-scatter intensity for B in invasion experiments confirms B aggregation in the presence of C (Fig. 3.6). For the purposes of discussion, we define a successful B invasion as one in which B abundances exceed $7 \times 10^4\,\mathrm{mL}^{-1}$ at the end of the experiment, or, in the case of panel **c,** when B abundances rise above $7 \times 10^4\,\mathrm{mL}^{-1}$ and then remain high for several days.

2.3 Bacterial invasions of algae.

Next we studied the dynamics of B invading A (Fig. 2.2b,e,h,j). When B is introduced into a low-density ($<5 \times 10^4\,\mathrm{mL}^{-1}$) culture of A, it successfully grows to

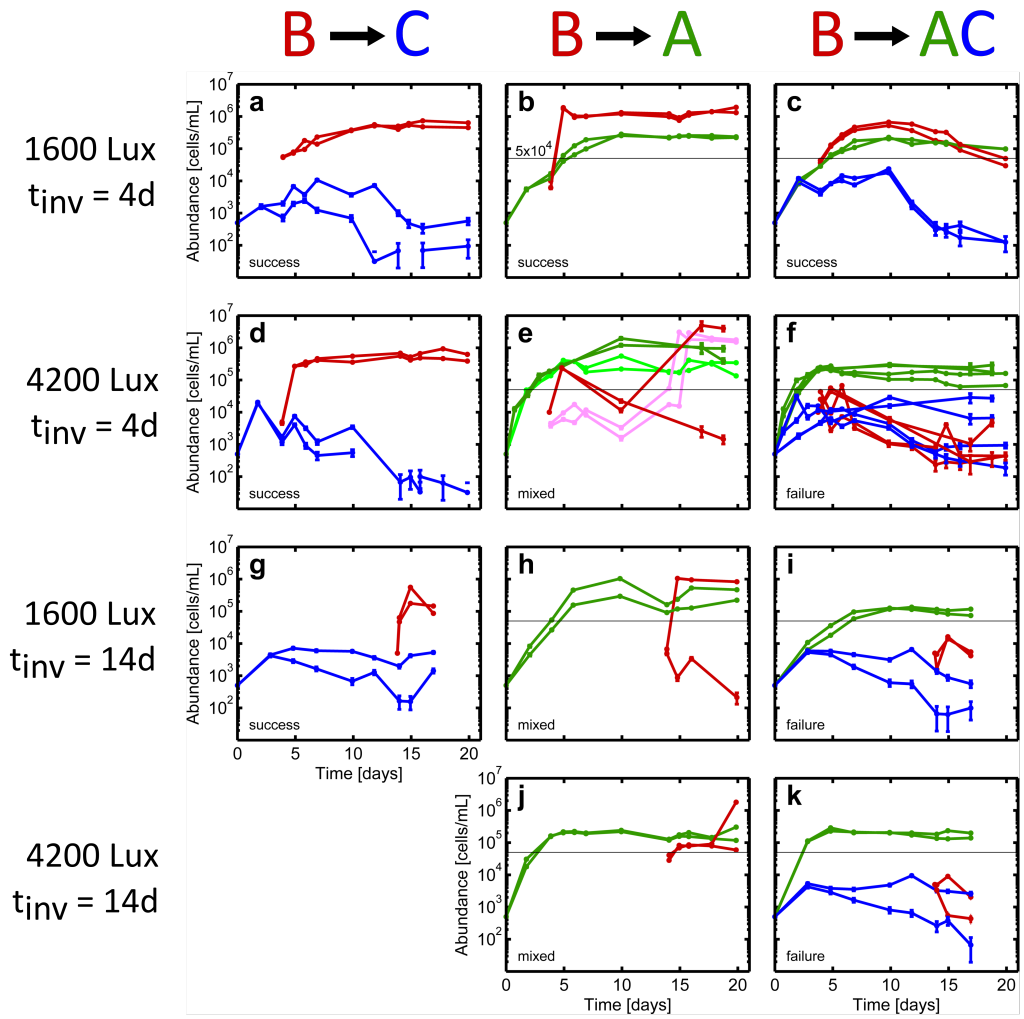

Figure 2.2: **Bacterial invasion dynamics.** A, B and C abundances are shown in green, red and blue respectively. B invasions of C (left column) or A (middle column) or AC (right column) occurred in either 1600 Lux (low light) or 4200 Lux (high light) at days 4 or 14 as indicated for each row. In each condition (community composition, light intensity, invasion time) at least two replicate communities were measured. Labels in each panel: "success", "failure", or "mixed" indicate the classification of the outcome of bacterial invasion with success defined as B exceeding a density of $7 \times 10^4\,\mathrm{mL}^{-1}$ for an extended period of time. Horizontal black line at $5 \times 10^4\,\mathrm{mL}^{-1}$ indicates a threshold on A. When A exceeds this threshold, B invasions can be inhibited. In panel (**e**), pink traces for B and light green traces for A denote experiments in which spent media measurements were performed (Fig. 3.14b). Abundances are measured via flow cytometry. Error bars are computed as described in Methods. For time points where error bars are not visible, errors are smaller than the size of the points. B abundances are reported as the total number of cells including planktonic cells and cells in aggregates as calculated with an aggregate correction algorithm described in chapter 3.

high density (Fig. 2.2b). Unexpectedly, when B is introduced into a high density ($>5 \times 10^4\,\mathrm{mL}^{-1}$) culture of A, B is strongly inhibited, exhibiting either very slow growth eventually reaching high densities more than 7 days after introduction, or crashing to low densities over a period of more than 5 days (Fig. 2.2e). In these experiments the ultimate outcome of B invasions is variable, with some succeeding and others failing, even between two identically prepared replicates (Fig. 2.2h,j). We find that inhibition of B growth by A only occurs when A is at high density and that the inhibition occurs both at low and high light levels (Fig. 2.2e,h,j). When A abundances are high at the time of B introduction, B eventually reaches high density ($>7 \times 10^4\,\mathrm{mL}^{-1}$) 50 % of the time (5 of 10 invasion experiments, Figs. 2.2e, 2.2h, 2.2j & 3.9c). However, when A densities are low at the time of B introduction, B grows to high density immediately in every replicate (8 of 8 experiments, Figs. 2.1f, 2.2b, 3.8b & 3.9b). Note that the inhibitory interaction between A and B is only apparent when B has not reached stationary phase. If B reaches stationary phase before A abundances exceed $5 \times 10^4\,\mathrm{mL}^{-1}$, we observe no inhibition of B by A, not even once A abundances exceed that density later in the experiment (compare Fig. 2.1c&f).

To confirm the dependence of B invasion success on A density, we performed a set of invasion experiments where B was introduced into A cultures at $t = 0$ days (pair-culture experiment), 1 day, 3 days, and 4 days, all at high light (4200 Lux) (Fig. 3.9). We confirmed that for those A cultures which did exceed density $5 \times 10^4\,\mathrm{mL}^{-1}$ at the time of B introduction, B growth was inhibited.

We next showed that resource competition is not the mechanism by which A inhibits B growth. We harvested spent media from an AB invasion experiment at several time points (Fig. 2.2e pink traces, Fig. 3.14b). We then filtered out both A and B and inoculated fresh B cells at low density into this spent media. Remarkably, B was able to grow to high density ($>10^5\,\mathrm{mL}^{-1}$) on spent media harvested before $\sim t = 15\,\mathrm{d}$. (Fig. 3.14d). For spent media harvested after $\sim t = 15\,\mathrm{d}$ (when B finally grows to high density), B can no longer grow to high density on the spent media. This result shows that consumable nutrients exist for B, even while B's growth is being inhibited by A. High-density populations of A do not compete with B for these nutrients, but do limit the ability of B to consume them.

2.4 Possible mechanisms of algae inhibition of bacterial growth.

We undertook a series of experiments to better understand the mechanism by which A inhibits B growth. We found that the inhibition of B growth by A requires illumination, and that the presence of A alone, in the absence of light, is not sufficient to inhibit B growth (Fig. 3.10). This result suggests that the photosynthetic metabolism of A is necessary for inhibition of B growth.

Since reactive oxygen species are produced by metabolically active plants [69] and algae including *C. reinhardtii* [70], we suspected that hydrogen peroxide may be responsible for the inhibition of B growth. In an independent experiment we measured the dependence of B growth on hydrogen peroxide concentration and found that a strong growth defect emerged only when initial hydrogen peroxide concentration exceeded 1mM with complete cessation of growth at 10mM (Fig. 3.12). We then measured the hydrogen peroxide concentration in cultures of A before and after B invasion and found levels to be undetectable ($<10^{-5}$M, the minimum level we can measure). We conclude that hydrogen peroxide is not responsible for A inhibition of B.

We found that the role of light intensity in the inhibition of B growth was dependent on the growth history of A (Fig. 3.11). For A grown to high density in a flask in a shaker, rather than in the custom-culture devices, B is able to invade immediately as long the the light level is low (1600 Lux). Contrast this result to the standard experiments in custom-culture devices (Fig. 2.2) where high-density A is sufficient to stall B invasion regardless of the light level.

Further, we considered the hypothesis that increased cell-to-cell contact due to the higher density of A could be responsible for the inhibition of B by A. A mechanism of this nature would also be consistent with the fact that A's inhibition of B disappears when A is filtered out (Fig. 3.10c). To investigate this possibility, we used the formalism of Seymour *et al.* [71] to estimate the rate at which we expect A and B to come into physical contact given the measured stirring rates in our vials. We found that bacteria encounter algae hundreds of times per second, even when densities of A are as low as $500\,\mathrm{mL}^{-1}$ (see chapter 3). This calculation suggests that

physical proximity between cells is frequent even in the regime where A abundances are low, arguing against the possibility of physical contact being important. This calculation does not rule out a contact mediated interaction which is associated with a physiological change in algae at higher abundances.

On closer inspection of our flow cytometry data, we noted that B adheres directly to A cells and these adherent populations can be measured directly (Fig. 3.13). This suggested the possibility that B adhering the A cells might either explain the apparently low density of B during failed invasions or that increased adherence of B to A during failed invasions might be responsible for the reduced growth rate of B. Neither of these hypotheses were supported by the data. Instead, we observed a small, but constant fraction ($\sim$5 %) of B cells adhered to A irrespective of whether B was inhibited by A or not.

As a final check, we confirmed that successful invasions were not a case of A detritus being misclassified as B (Fig 3.19).

Irrespective of the molecular mechanism of the antagonistic interaction between A and B, it is clear that the inhibition of B requires high density A, light, and a B population that has not reached stationary phase. Finally, the variable outcomes for B invading A are in stark contrast to the reproducible dynamics observed in Fig. 2.1 and in previous studies [61], suggesting that there may be stochastic processes at the single-cell level which are responsible for the inhibition or that the system is highly susceptible to small experimental variations near the transition between B inhibition and B growth. We now turn to the central objective of the present study, the invasion of B into AC communities.

2.5 Bacteria fail to invade algae-ciliate communities when algal densities are high.

Next we performed B invasions of AC cultures (Fig. 2.2c,f,i,k). Unexpectedly, we found that in every single case where C is present and A density exceeds $5 \times 10^4\,\mathrm{mL}^{-1}$ at time of B introduction, B fails to invade and ultimately declines to very low densities (Fig. 2.2f,i,k). This result stands in stark contrast to B's successful invasions of A or C alone. When B is introduced into an AC community with low A density

($<5 \times 10^4\,\mathrm{mL}^{-1}$), B grows to high density and then slowly declines in abundance later in the experiment (Fig. 2.2c). We conclude that if C is present and A is at high density at the time of B introduction, B cannot proliferate and ultimately declines to low abundance. B's failure to invade AC cultures is the main finding of this study.

One possible explanation for this finding is that AC communities with high A densities have exhausted a critical nutrient for B growth. Spent media experiments again show this not to be the case. We performed a series of spent media experiments where communities with A, C, or A and C were grown, samples were harvested, and then all cells were removed by filtration (example shown in Fig. 3.14a). B was then inoculated into this spent media and grown to saturation in a 96-well plate where its abundance was assayed by flow cytometry. This measurement captures the carrying capacity of bacteria on the spent media. We find that B is able to grow on the spent media of A, C, and AC communities to a saturating density that is indistinguishable from growth on fresh media, irrespective of the time at which the spent media was taken (Fig. 3.14c). This result rules out the hypothesis that nutrient competition accounts for any of the invasion outcomes in Fig. 2.2.

The results of Fig. 2.2 suggest that a higher-order effect, unexpected from pairwise interactions, governs the outcome of B invasions of AC communities. Only when A and C are both present do B invasions reliably fail. Next we sought to understand the mechanism of this effect.

2.6 Algae enhance ciliate predation of bacteria in a density-dependent fashion by inhibiting bacterial aggregation.

We propose that a higher order (3-body) interaction is responsible for the fact that B cannot invade an AC community when A abundances exceed $5 \times 10^4\,\mathrm{mL}^{-1}$: high density A induce B to remain in a planktonic (single-celled) state, robbing B of aggregation, its primary defense mechanism against predation by ciliates (Fig. 2.1e).

First, we show that B aggregation is inhibited by high density A. Note that as bacteria grow in monoculture they initially aggregate and then ultimately disaggregate

(Fig. 2.1e, orange traces). This non-monotonic change in aggregation is potentially due to substrate level dependent aggregation rates observed previously [72,73]. When A and B are grown in pair-culture, the aggregation and subsequent dispersal of B is nearly identical to what we observe in B monocultures (compare red traces in Fig. 2.3e to orange traces in Fig. 2.1e). Similar B aggregation dynamics are observed when B invades a low density A culture (Fig. 2.3b,e). However, when B invades at day 4 into a high light (4200 Lux) A culture that has reached $1 \times 10^5\,\mathrm{mL}^{-1}$, B does not grow immediately (Fig. 2.3c) and for the duration of this growth inhibition their aggregation is inhibited (Fig. 2.3e, black traces). Only once the inhibitory effects of the algae are overcome by B after ten days can B grow and aggregate. We conclude that algae inhibit bacterial aggregation in a manner that depends on the density of algae.

We investigated the inhibition of B aggregation by A further by examining the effect of A spent media on the ability of B to aggregate (Fig. 3.15). Using data from the previously described spent medium experiment, we examined the aggregation state of B (mean side-scatter) as a function of the time at which the spent media was extracted from the growing A culture. We find an inverse relationship between the extraction time of spent media and level of B aggregation when grown on that spent media. The fact that A is not physically present in the spent media suggests that its ability to inhibit B aggregation is mediated by a chemical rather than a physical interaction. Interestingly, while spent media from an A monoculture disaggregates B, it does not inhibit growth of B. This result indicates that aggregation is not necessary for B to grow in this media. The independence of aggregation and growth is supported by the fact that a B mutant deficient in aggregation ($\Delta csgA$) grows in monoculture on this media without aggregating (Fig. 3.7e). Our observation that A disaggregates B is qualitatively consistent with observations that *Chlamydomonas* can secrete signaling molecules such as auto-inducers which can interfere with biofilm formation [74].

C has the opposite effect on B in that it induces B to aggregate (Fig. 2.1e, Figs. 3.6 and 3.7). In all cases where only B and C are present, aggregation of B greatly exceeds that in B monoculture or AB pair-culture. We conclude that A and C have opposing effects on the aggregation state of B, with A inhibiting and C enhancing

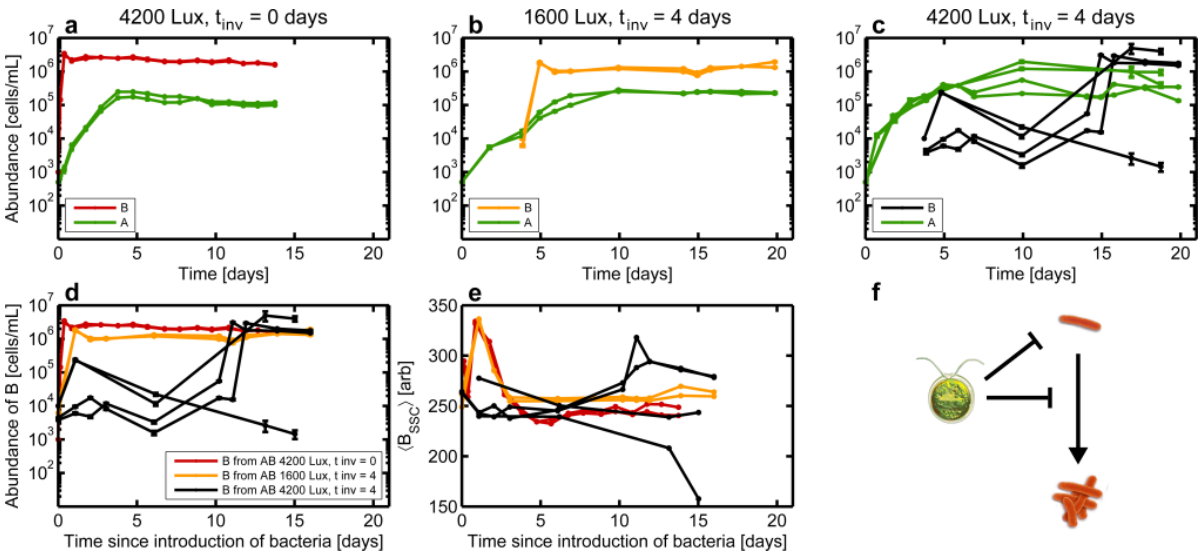

Figure 2.3: **Algae suppresses bacterial aggregation.** A abundances are shown in green. Color of B abundance trace varies in **a-c** as indicated in the legends. **a,** Abundance dynamics for two replicates of a high light (4200 Lux) AB pair-culture (t_{inv}=0 days) **b,** Abundance dynamics for two replicates of a B invasion on A in low light (1600 Lux) with t_{inv}=4 days. A density is $\sim 1 \times 10^4\,\mathrm{mL}^{-1}$ at time of B introduction **c,** Abundance dynamics for four replicates of a B invasion on A in high light (4200 Lux) with t_{inv}=4 days, A density is $> 1 \times 10^5\,\mathrm{mL}^{-1}$ at time of B introduction. Abundances are measured via flow cytometry. Error bars are computed as described in Methods. For time points where error bars are not visible, errors are smaller than the size of the points. B abundances are reported as the total number of cells including planktonic cells and cells in aggregates as calculated with an aggregate correction algorithm described in chapter 3. **d,** Overlay of B abundances from (**a,b&c**), translated so that $t = 0$ corresponds to the time of B introduction. **e,** Overlay of mean side-scatter signal of B, translated so that $t = 0$ corresponds to the time of B introduction. The low side-scatter signal at the final time-point in one of the black traces arises from a small number (20) of counts. Colors of traces in (**d,e**) correspond to panels (**a-c**). **f,** Diagram of interactions for A and B. Panel (**a**) is reproduced from Fig. 2.1**f**, (**b**) and (**c**) are reproduced from Fig. 2.2**b&e**.

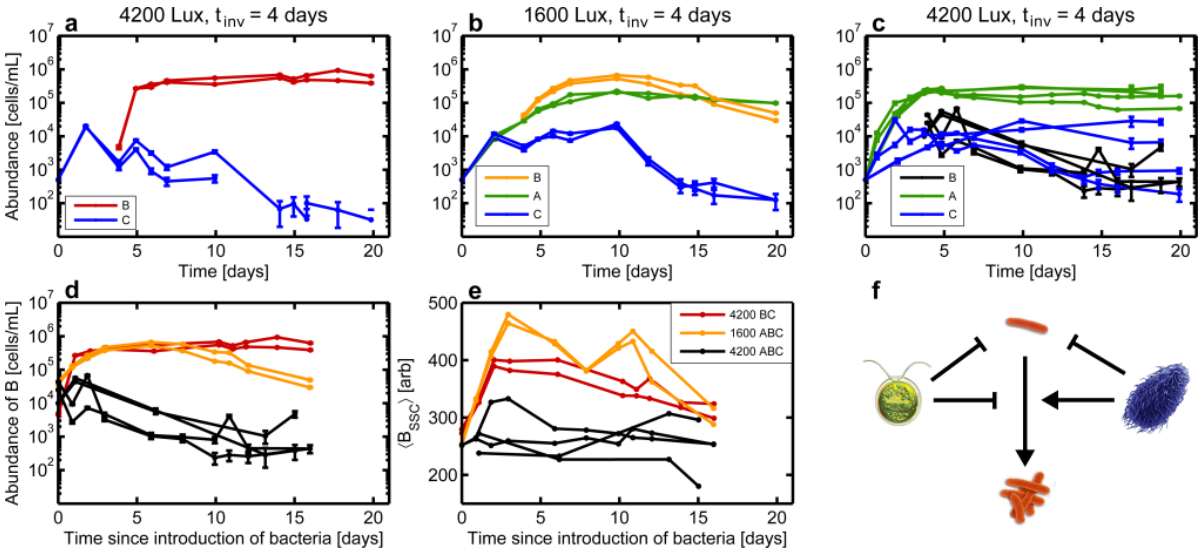

Figure 2.4: **Algae inhibit bacterial aggregation enhancing ciliate predation resulting in invasion failure.** A and C abundances are shown in green and blue respectively in all panels. Color of B traces differs between panels **a-c** as shown in the legends. **a,** Abundance dynamics for two replicates of a 4200 Lux (high light) t_{inv}=4 days B invasion on a C culture. **b,** Abundance dynamics for two replicates of a 1600 Lux (low light) t_{inv}=4 days B invasion on an AC culture. A density is $2 \times 10^4\,\mathrm{mL}^{-1}$ at time of B introduction **c,** Abundance dynamics for four replicates of a 4200 Lux (high light) t_{inv}=4 days B invasion on an AC culture. A density is $> 1 \times 10^5\,\mathrm{mL}^{-1}$ at time of B introduction. Abundances are measured via flow cytometry. Error bars are computed as described in Methods. For time points where error bars are not visible, errors are smaller than the size of the points. B abundances are reported as the total number of cells including planktonic cells and cells in aggregates as calculated with an aggregate correction algorithm described in chapter 3. **d,** Overlay of B abundances from (**a,b,c**), translated so that $t = 0$ corresponds to the time of B introduction. **e,** Overlay of mean side-scatter signal of B, translated so that $t = 0$ corresponds to the time of B introduction. Colors of traces in (**d,e**) correspond to panels (**a-c**). **f,** Diagram of interactions between A, B, and C. Panels (**a,b&c**) are reproduced from Fig. 2.2**d,c&f**.

aggregation.

We hypothesize that the failure of B to invade a culture of C and high-density A (Fig. 2.4c) is due to A inhibiting B aggregation and subsequently increasing the predation pressure of C on B. Under this hypothesis we expect that when B fails to invade an AC community, B will have failed to aggregate, and this is precisely what we observe (Fig. 2.4e). Conversely, when B successfully invades an AC community (which occurs when A is at low density at time of B introduction) B aggregates effectively as we expect, thus evading predation from C (Fig. 2.4b,e). We conclude that when A inhibits B aggregation, this results in stronger predation of B by C, thus driving bacterial abundances down in time.

In order for our hypothesis to be true, B aggregation must be a necessary condi-

tion for survival of B in the presence of C. To validate this aspect of the hypothesis, we constructed a $\Delta csgA$ strain of *E. coli* that exhibited dramatically reduced aggregation in liquid culture (Supplementary Figure 11, Laganenka *et al.* [75]). We introduced this B into a culture of C and hypothesized that it would be unable to invade. Surprisingly, $\Delta csgA$ aggregated and invaded successfully (Fig. 3.7). Because it aggregated, this strain did not ultimately test our hypothesis, but it did reveal that there are mechanisms other than curli responsible for aggregation.

Taken together, the results of Figs. 2.2, 2.3, & 2.4 show that a higher-order interaction between the three species governs the outcome of B invasions on AC. In particular, A reduces B aggregation which renders the bacteria susceptible to predation by C. We call this interaction "higher-order" because all three species must be present in order for this interaction to affect the abundance dynamics of B. This interaction also satisfies the definition of a higher-order interaction given in the introduction: "whenever one species affects the nature of the interaction between two others" [29]. In order to confirm that such an interaction would explain our data and also to generalize our result, we next sought a quantitative model of the dynamics in this community.

2.7 Mathematical model of algae-bacteria-ciliate invasion dynamics.

Our objective was to construct a model with a minimal number of free parameters that captures the dynamics we observe in Fig. 2.2. We chose to construct a purely deterministic model which describes the abundance dynamics of the algae and ciliates (x_A, x_C), non-aggregated bacteria (x_B), aggregated bacteria (A_B), and a single substrate consumed by x_B which we denote S. Our model takes the form:

$$\dot{x}_B = x_B(r_B - r_{AB}\frac{x_A}{K_A})S - Fx_Bx_C - \alpha_1 x_B x_C + \alpha_2 A_B x_A \tag{2.1}$$

$$\dot{A}_B = \alpha_1 x_B x_C - \alpha_2 A_B x_A \tag{2.2}$$

$$\dot{x}_A = r_A x_A(1 - \frac{x_A}{K_A}) \tag{2.3}$$

$$\dot{x}_C = r_C x_C(1 - \frac{x_C}{K_C}) \tag{2.4}$$

$$\dot{S} = -\frac{1}{Y}x_B(r_B - r_{AB}\frac{x_A}{K_A})S \tag{2.5}$$

dot denotes a derivative with respect to time, r_i is the growth rate of species i, r_{AB} is a parameter defining the inhibition of x_B by x_A, F is a feeding rate, α_1 and α_2 are aggregation and disaggregation rates of bacteria. Note that A_B do not grow (consume S) in this model. K_i captures the carrying capacity of species i and Y is a yield of bacteria growing on S.

For a complete discussion of the modeling decisions we made see chapter 3. Briefly, the first term in Eq. 3.1 captures the fact that x_A only impacts the growth rate of x_B and not its final abundance. Substrate is considered explicitly to enforce the fact that x_B cannot recover from predation if it had already reached saturating density (such a recovery which would occur with logistic growth). The predation of x_B by x_C is linear in prey density, an assumption justified by the relatively low densities of bacteria in our experiment. We neglect growth of x_C on x_B due to the low yield of ciliates on bacteria and the low densities of bacteria in our experiment. This assumption is supported by the data which shows no substantial difference in C densities with and without B (Fig. 3.21). Aggregation terms are consistent with our observations in Fig. 2.1 and 2.3. In this model, the mechanism by which bacteria (x_B+A_B) fail to invade communities of x_A and x_C is the disaggregation of A_B to x_B in a manner that is dependent on x_A density ($\alpha_2 A_B x_A$) and the subsequent predation of x_B by x_C (Fx_Bx_C).

The dynamics of x_A and x_C are modeled as logistic growth. For x_A, this model recapitulates the dynamics we observe very well so long as we make x_A growth rate decline as x_B or x_C are added to the community in low light as observed in experiment (Fig. 3.1a). The model neglects the decline in ciliate abundances at long times, likely

due to cell death. All parameters in the model except r_{AB}, α_1 and α_2 are measured or have been previously reported in the literature (as is the case for F). Of these three parameters r_{AB} must be on the order of r_B if we are to observe any substantial inhibition of x_B growth by x_A. α_1 can be constrained by a close examination of the BC pair-culture dynamics (Fig. 3.20) and α_2 is treated as a free parameter which we determined by performing a parameter sweep (Figs. 3.22, 3.23, & 3.24). With these parameter values (Table 3.1) we performed numerical integration of the model in Eqns. 3.1-3.5 for the invasion experiments shown in Fig. 2.2. The results are shown in Fig. 2.5 where we plot total B abundances (x_B+A_B), A abundances (x_A), and C abundances (x_C).

The reader may wonder why, if there is a higher-order (3-way) interaction in this system, no term appears in our model containing the product $x_A x_B x_C$. The answer to this question is that we explicitly model the phenotypic state of B by splitting it into two subpopulations: x_B for non-aggregated individuals and A_B for aggregated individuals. Had we chosen to use a single variable x_B for the abundance of B, as is typical in ecological models [76, 77], we could have used a term like $-\alpha x_A x_B x_C$ in the differential equation for $\dot{x}_B$. We chose not to use an effective interaction term in our model given that explicitly modeling phenotypic variation in B more faithfully captures the dynamics in our ecosystem.

The results in Fig. 2.5 should be compared to the experiments in Fig. 2.2. We note that this simple model captures the basic features of the invasion experiments: (i) B successfully invades C cultures (ii) B densities in the presence of C are lower than for B invasions of low-density A cultures (compare Fig. 2.5a,b) (iii) when B invades a high density A culture, its growth rate is attenuated (Fig. 2.5e,h,j), but B eventually reaches high density ($>1 \times 10^6\,\mathrm{mL}^{-1}$) (iv) when B is introduced into an AC culture with high density A, B declines in abundance continuously (Fig. 2.5f,i,k) (v) when B is introduced into an AC culture with low density A, B invades immediately, but slowly declines in abundance over time (Fig. 2.5c). Our deterministic model cannot capture the variability in outcomes of B invading A alone. The model describes the invasion experiments faithfully without requiring the specification of a large number of unknown parameters.

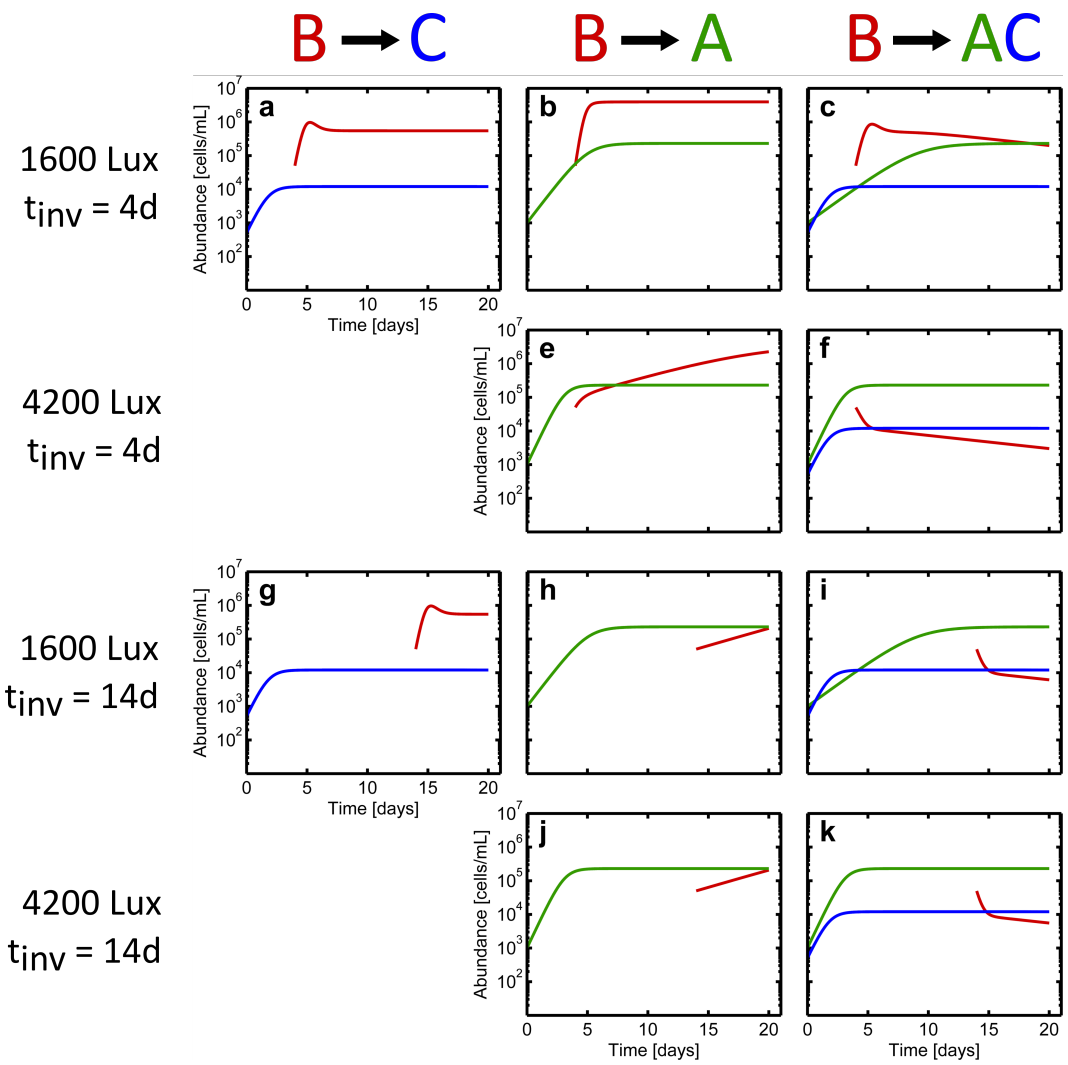

Figure 2.5: **Model of algae-bacteria-ciliate dynamics captures invasion experiment outcomes.** Simulation of the model described in the main text. Panels correspond to Fig. 2.2. Species compositions are organized by column as shown (top). Light conditions and time of invasion are organized by rows as shown (left). In all panels abundance dynamics of A (x_A), B (x_B+A_B), and C (x_C) are shown in green, red and blue respectively. The first panels in the second row and the fourth row are omitted since BC dynamics do not depend on illumination intensity in the model. Parameters of the model are as follows: $r_B = 0.3\,\mathrm{h}^{-1}$; $r_{AB} = 0.29\,\mathrm{h}^{-1}$; $r_C = 0.073\,\mathrm{h}^{-1}$; r_A (high light) $= 0.073\,\mathrm{h}^{-1}$; r_A (low light, w/BC) $= 0.016\,\mathrm{h}^{-1}$; r_A (low light, w/C) $= 0.025\,\mathrm{h}^{-1}$; r_A (low light, w/B) $= 0.031\,\mathrm{h}^{-1}$; r_A (low light, alone) $= 0.045\,\mathrm{h}^{-1}$; $K_A = 2.3 \times 10^5\,\mathrm{mL}^{-1}$; $K_C = 1.2 \times 10^4\,\mathrm{mL}^{-1}$; $F = 1 \times 10^{-5}\,\mathrm{mL\ h}^{-1}$; $\alpha_1 = 2.5 \times 10^{-6}$ mL h^{-1}; $\alpha_2 = 2 \times 10^{-8}$ mL h^{-1}. Substrate concentration is chosen to yield the observed carrying capacity of B in monoculture ($3.9 \times 10^6\,\mathrm{mL}^{-1}$).

2.8 Impact of higher-order interaction is apparent in ABC tri-culture abundance dynamics.

We next asked whether the model could provide a non-trivial prediction regarding community dynamics. To investigate, we simulated the dynamics of the ABC tri-culture under the two light regimes. The model predicts that under high light conditions, where x_A rapidly approaches K_A bacterial abundances (x_B+A_B) are attenuated at long times. In contrast, for low light conditions where x_A does not reach high density until the very end of the experiment, our model predicts limited attenuation of bacterial abundances (compare Fig. 2.6c,d). The lower bacterial abundances observed in our simulation at high light arise from reduced bacterial aggregation and increased predation of x_B by x_C (Fig. 2.6f).

To test the predictions of the model we performed tri-culture experiments with the full ABC community at low and high light levels. The dynamics are shown in Fig. 2.6i,j. In the full ABC ecosystem, the growth rate of A differs dramatically between the two light levels ($0.016\,\mathrm{h}^{-1}$ for low light versus $0.073\,\mathrm{h}^{-1}$ for high light). The slow growth rate of A in low light results in A reaching saturation only after 14 d. In contrast, in high light, A reaches saturating densities in 4 days. When we compare the dynamics of B in the full ABC ecosystem in low and high light we observe that high light results in a substantial decline in bacterial abundances by the end of the experiment (Fig. 2.6k, purple and black traces). In contrast, when B is grown with only C (and not A) in high light there is no decline in B abundances at long times (Fig. 2.6k, orange and purple traces). When we examine the bacterial aggregation state in the ABC low light and high light conditions we find less B aggregation in the high light condition (Fig. 2.6l). We therefore conclude that in the high light condition the rapid rise of A drives substantial disaggregation of B and subsequent predation of B by C. Note that the effect is not driven by light alone since changing light levels does not alter the abundance dynamics of B in monoculture, AB pair-culture or BC pair-culture (Fig. 3.8). The predictions of the model are confirmed and so we conclude that rapid growth of A to high density substantially impacts B in the presence of C via the same higher order interaction which inhibits B invasion of AC communities with high A abundances.

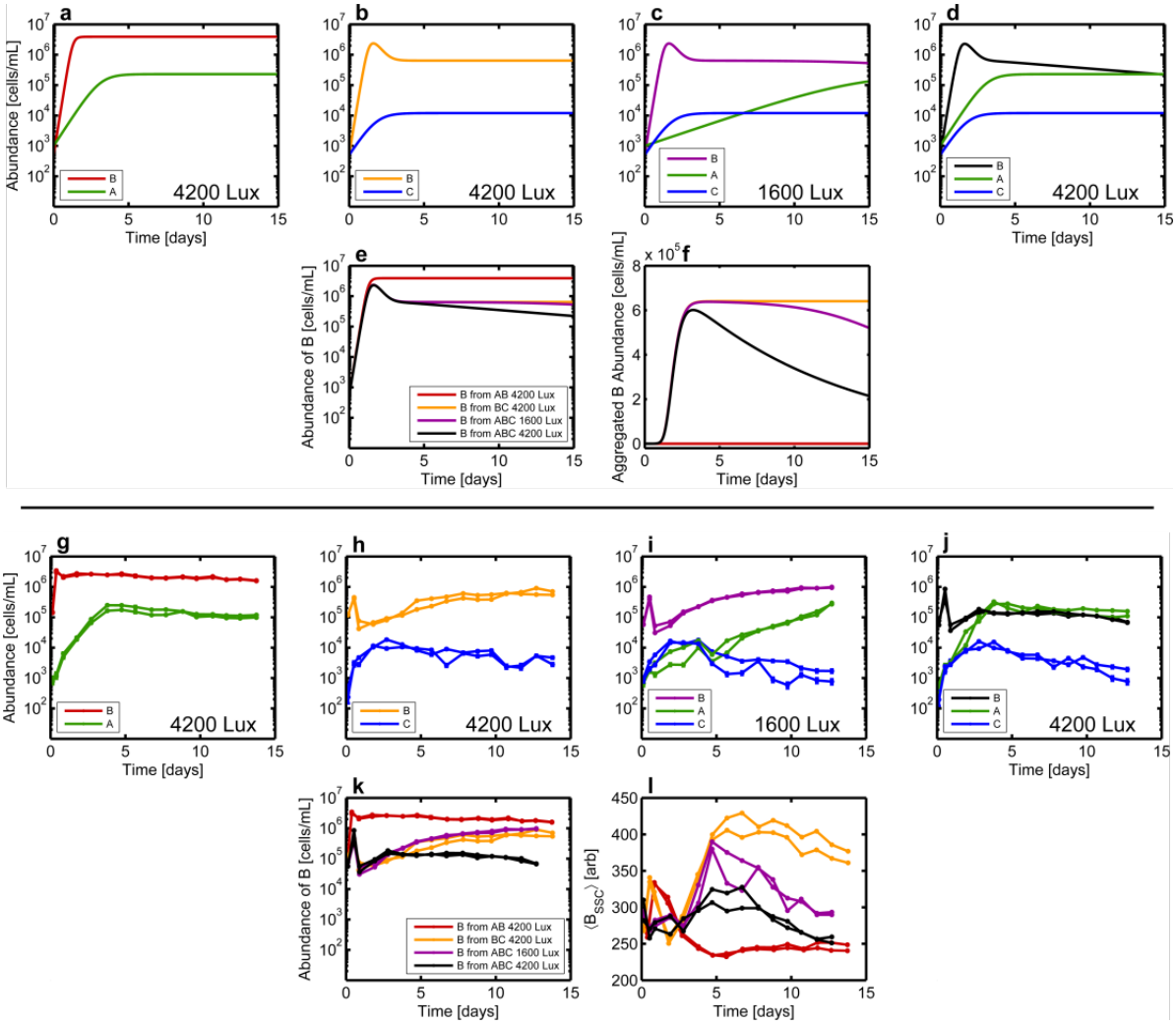

Figure 2.6: **Higher-order interaction impacts algae-bacteria-ciliate tri-culture abundance dynamics. a-f,** Simulations of abundance dynamics in tri-culture conditions where all species are introduced at low density at $t = 0$ days. All model parameters are given in Table 3.1 . In all panels x_A and x_C are shown in green and blue respectively. The color of B ($x_B + A_B$) varies as indicated in the legends of (**a-d**) to facilitate the overlay plots in (**e,f**) which show total B abundances ($x_B + A_B$, **e**) and aggregating cell abundances (A_B only, **f**). Legend from (**e**) applies to (**f**). **g-l**, Experimental measurements of tri-culture abundance dynamics corresponding to panels (**a-f**). Replicate communities are shown in each condition. Abundances are measured via flow cytometry. Error bars are computed as described in Methods. For time points where error bars are not visible, errors are smaller than the size of the points. B abundances are reported as the total number of cells including planktonic cells and cells in aggregates as calculated with an aggregate correction algorithm described in chapter 3. Note that the color of the traces for B abundances in (**g-j**) correspond to those in (**a-d**) and are indicated in the legends. **k**, Overlay of abundance dynamics for B from (**g-j**). **j**, Mean side-scatter (which is a proxy for level of aggregation) of the B population from panels (**g-j**). Legend from (**k**) applies to (**l**).

2.9 Discussion

Our results show that phototrophs can indirectly inhibit the growth of heterotrophic bacteria through higher order interactions with predators. Phototroph-heterotroph interactions are known to be mediated by competition and cross feeding [78], but our data provide a new mechanism by which phototrophs might keep faster growing heterotrophs from consuming available nutrients such as nitrogen or phosphorous.

In the context of the invasion literature (recently summarized be Mallon *et al.* [56]) our results show that resource competition alone is insufficient for predicting the outcome of invasions in communities where antagonistic interactions are present. The result has important implications for understanding community structure from coral reefs to wastewater treatment facilities where such interactions are known to be present [54, 55].

Further, recent theoretical work suggests that higher-order interactions (3-way and higher) enhance the stability of complex communities whereas communities described by pairwise interactions alone become less stable as complexity increases [76, 77]. While several studies have previously detected the presence of higher-order interactions [79, 80], direct measurements of the impact of higher-order interactions on ecosystem dynamics or invasions is limited. In contrast, several studies of dynamics in communities where interactions are mediated by resource competition have shown that pairwise interactions are sufficient to describe community dynamics [81,82]. Our study shows definitively that for a model community which includes predation and little or no competition for resources, higher order interactions are not only present, but have substantial impacts on dynamics (Fig. 2.6). To move theory closer to observation and experiment, it will be critical to investigate whether higher-order interactions are more common when antagonism is present or not.

Two previous studies on the ABC community, or a closely related ecosystem with *C. reinhardtii* replaced with *Euglena gracilis*, under hermetically sealed conditions have looked at interactions between these species. One study compared interactions inferred from abundance fluctuations in the full three species community to interactions measured via pair-culture experiments [83]. A second study also used pairwise experiments [84]. In the case of the pairwise experiments, both studies detected evidence for the antagonistic effect of A and C on B. Interestingly, inference of pairwise

interactions from abundance fluctuations in an ensemble of ABC communities did not identify these negative interactions [83], and instead inferred positive effects between all three species. This result points to the challenge of inferring interactions from fluctuations in time series data [85–87]. Inferring interactions from fluctuations should work well near a fixed point of the community dynamics. However, understanding the full non-linear dynamics governing the community is likely a necessity for predicting the outcome of processes like invasion where abundances can change by several orders of magnitude. Finally, neither previous study of the ABC system made a statement about the presence of higher-order effects in the community or the mechanisms mediating these interactions.

More broadly, our study provides a stark example of the level of complexity present in even a comparatively simple model microbial community. Our discovery that a phenotypic trait of the bacteria (aggregation) is modulated by the algae and dramatically impacts the success of bacterial invasion points to both the power of studying model communities like the ABC system and the challenge of predicting dynamics in more complex ecosystems.

2.10 Methods

Strains The algae is *C. reinhardtii*, strain UTEX2244 obtained from the UT Austin Culture Collection of Algae `utex.org`. All *C. reinhardtii* cells are of a single mating type mt+ and grow vegetatively. Algae are cryogenically preserved and stored in liquid nitrogen `https://utex.org/pages/cryopreservation#liquid`. The *E.coli* strain is MG1655 Δ *flu*, Δ *fimA* and was constructed previously [60]. A constitutively expressed yellow fluorescent protein (YFP, promoter $\lambda \mathrm{P}_R$) was transduced into the genome with phage P1. The donor strain for YFP fluorescence has the YFP gene inserted in the *intC* locus along with a chloramphenicol antibiotic resistance marker [88]. The $\Delta csgA$ strain was constructed by P1 transduction from KEIO collection [89] mutant into MG1655 (WT) background. The same YFP construct was also transduced into this strain. The ciliate is *T. thermophila*, strain CU428.2 obtained from the Cornell University Tetrahymena Stock Center `https://tetrahymena.vet.cornell.edu/`. All *T. thermophila* cells are of mating type VII so there is only asexual

reproduction. This strain grows vegetatively indefinitely without sexual reproduction. Ciliates were cryogenically frozen and stored in liquid nitrogen [90].

Culturing Before beginning the experiment, each of the organisms is cultured separately in distinct media. *A* is cultured in a 30 °C shaker-incubator with ∼3000 Lux illumination in Tris-Acetate-Phosphate (TAP) media inoculated directly from a freezer stock. Algae used in co-culture experiments (low-light), A, AC, ABC and (high light) A, AC and ABC were grown at 25 °C prior to the experiment. TAP is a defined media with acetic acid as a carbon source `https://www.chlamycollection.org/methods/media-recipes/tap-and-tris-minimal/`. *C* is cultured in a 30 °C stationary incubator in (undefined) SPP media inoculated directly from a freezer stock. *B* was cultured in a 30 °C shaker-incubator in 1/2x Taub 0.03% proteose peptone No. 3 inoculated from a single colony grown on an lysogeny broth (LB) plate.

Control of initial conditions The cultures of each of the three organisms are washed twice into 1/2x Taub .01% Proteose Peptone No. 3. Flow cytometry is performed on a sample from each washed culture to estimate cell densities. The cultures are then diluted into 1/2x Taub .01% proteose peptone No. 3 in order to achieve nominal densities of 500 ± 22 mL^{-1} for *A*, 1000 ± 32 mL^{-1} for *B*, and 500 ± 22 mL^{-1} for *C*. Error bars are assumed from Poisson counting error. Organisms are always started at these densities at the beginning of an experiment, regardless of whether that experiment is monoculture, pair-culture, or tri-culture. For B invasion experiments the starting density was $1 \times 10^4\,\mathrm{mL}^{-1}$.

Experimental conditions All experiments are performed in 1/2x Taub .01% proteose peptone No. 3. This media is used because it is similar to media used in previous studies with the ABC community [60, 61] and because each of the three organisms can grow on this media in monoculture, pair-culture, and tri-culture. Taub media is a freshwater mimic media that was originally created to support co-cultures of *Daphnia pulex* and *Chlorella pyrenoidosa* [91,92]. It contains 15μM H_3BO_3; 0.5μM $ZnSO_4$; 3.5μM $MnCl_2$; 0.5μM Na_2MoO_4; 0.1μM $CuSO_4$; 0.5μM $Co(NO_3)_2$; 100μM $MgSO_4$; 100μM KH_2PO_4; 5.6μM EDTA; 5.6μM $FeSO_4$; 1.5mM NaCl; and 1mM $CaCl_2$. Proteose peptone No. 3 is an undefined nutrient source that is an enzymatic digest of protein and supplies nitrogen and carbon [`http://www.bdbiosciences.`

com/ds/ab/others/Proteose_Peptone_No_2_3_4.pdf]. The media is titrated to pH 7 before use.

Culture devices and conditions During the experiment, 30 mL of culture are grown in a glass vial (Chemglass CG-4902-08 40 mL volume). A 0.1 µm filter allows gas exchange between the culture and the atmosphere. We expect this gas exchange (venting) coupled with stirring allows the community to be rapidly equilibrated with atmospheric O_2 and CO_2 concentrations. Eight vials are run in parallel.

Each of the eight vials are kept in an experimental apparatus for the duration of the experiment. The vial fits snugly into a metal block that is held at 30 °C via PID control. Temperature is measured by a thermometer embedded in the metal block and heating/cooling is performed by a Peltier element [72]. The temperature within a vial fluctuates with standard deviation 0.02 °C as determined by the feedback thermometer embedded in the metal block housing the vial. The temperature across the eight vials varies with standard deviation 0.08 °C as measured in a control experiment where each vial is filled with water and the temperature is measured using a high-accuracy Fisher Scientific Traceable Thermometer (p/n: 15-081-102) and taking the standard deviation across vials.

The vial is illuminated by a single LED (Cree XLamp XP-E2 Single 1 Up Neutral White 4000 K color temperature, LED Supply p/n: CREEXPE2-740-1) from below. The LED is driven by an LED driver (BuckPuck DC LED Driver LED Supply p/n: 03021-D-E-350) and the intensity of these LEDs was found to be too high for bacterial growth and is decreased through the use of a neutral density filter. The illuminance is further modulated by applying a voltage to the control pin of the LED Driver. Experiments are performed at either low light (1600 ± 140 Lux) or high light (4200 ± 330 Lux). These values represent the time-averaged illuminance an organism would experience assuming it spends an equal amount of time at each height in the vial. These values are calculated based on measurements of illuminance taken from the top of the metal block with a light meter (LED Light Meter p/n: PCE-LED 20). Error bars are standard deviation across systems. The light levels are on the same order of magnitude as those used in a previous study of the ABC ecosystem [61]. The experimental apparatus is mounted on a stir-plate (Thermo Scientific Cimarec-i Mono Direct Stirrer 50095601) that keeps cultures stirred at 444 ± 4 RPM. This

rotation speed was measured with a custom Hall Probe. Error is standard deviation across systems.

Sampling of communities for flow cytometry Samples of communities are taken via a syringe attached to a sterile port. 500 µL are drawn from the vial for each sample. This process constitutes destructive sampling of the community. Over the course of a typical experiment, 16 samples are taken from the vial which corresponds to 8 mL being removed from the vial. The depth of liquid in the vial decreases by 1.65 cm from its initial depth of 6.25 cm.

Abundance measurement by flow cytometry Flow cytometry is performed using a Becton-Dickson LSR II. To count bacteria, YFP fluorescence is plotted versus side-scatter (SSC) and cells are gated manually. To count algae, Chlorophyll-b fluorescence is plotted versus YFP fluorescence and gated manually. To count ciliates, CFP fluorescence is plotted versus SSC and the gate is drawn manually. Correct gating is confirmed by making measurements on monocultures. Because of the size difference between bacteria and ciliates, the two organisms scatter vastly different amounts of light and so a different gain is appropriate for the SSC channel for each. We therefore run every flow sample on two different settings. Settings 1 is used for ciliates and gain voltages are 498 for CFP and 203 for SSC. Settings 2 is used for algae and bacteria and gain voltages are 501 for YFP, 275 for chlorophyll-b, and 250 for SSC.

Calibration of flow rate to infer densities To report densities we calibrate the liquid flow rate through the flow cytometer using Spherotech Accucount fluorescent beads (ACFP-50-5, 5.0-5.9 μm) which come at a known concentration of $2 \times 10^6\,\mathrm{mL}^{-1}$. The beads are diluted tenfold and run for 30 s, the same duration of time that ecosystem samples are run. From the number of beads detected in 30 s we compute a flow rate. For every time point in the abundance data, we perform three replicates of this volume calibration. We assume that the volume calibration applies to all samples run at that time point (within $\sim$1 hour of the calibration of the cytometer). Over the course of this study (2 years) we observed a decrease in the LSR II flow rate by 60%.

Error bars on abundance measurements Error bars on abundances are calculated by performing propagation of two forms of error: (1) the Poisson error inherent

in counting a finite number of cells and (2) the uncertainty in volume run through the flow cytometer. The uncertainty in flow rate is taken as the standard deviation across the three replicates of bead calibration on the day the abundance was measured.

Spent media experiments In spent media experiments, cultures are prepared and grown as normal. To obtain spent media, several hundred microliters are extracted from the culture and filtered through a 0.22 µm polyethersulfone (PES) filter. Spent media is stored at 4 °C until all spent media extractions are complete. Spent media was then added to a 96-well microtiter plate and inoculated with bacteria and, depending on the experiment, ciliates. The plate was shaken and incubated at 30 °C for two or three days so that bacteria can grow to saturation. Bacterial abundance is then measured via flow cytometry.

Simulations Numerical integration of the model was performed using custom written Matlab scripts. Time steps of 1 minute were used to ensure numerical stability and accuracy. Organisms that fell below a density of $1\,\mathrm{mL}^{-1}$ were assumed extinct and could not recover. Invasions were accomplished by instantaneously adding a fixed density of B at t_{inv}. Parameters of the model and details of the modeling choices are available in the SI.

Chapter 3

Supplementary Results

3.1 Algae and Ciliate growth rates

We calculated growth rates for algae and ciliates in all coculture experiments. Growth rate was calculated by fitting a line to the linear portion of the natural logarithm of that species' abundance in time. Algae growth rates at 1600 Lux (low light) were significantly different for different species compositions and we thus report a growth rate for each species composition (Fig. 3.1a). For algae at 4200 Lux (high light), or ciliates at either light level, growth rates were not significantly different across species compositions and we thus report a single growth rate over all species compositions (Fig. 3.1b,c&d). We do not report growth rates here for bacteria since the time resolution of our flow cytometry measurement is too coarse to reliably measure bacterial growth rates. Bacterial growth rate is instead measured using continuous absorbance measurements in a plate reader.

3.2 Bacterial aggregation

In the main text we report that side scatter signal of bacteria (YFP fluorescence) reflects the aggregation of bacteria, with higher side scatter levels indicating larger bacterial aggregates. Here we support this claim experimentally.

3.2.1 Vortex experiment confirms side-scatter measures aggregation

High side-scatter bacterial objects were originally suspected to be aggregates of bacteria for two reasons. 1) Side-scatter is a measure of how much light is scattered at a 90 degree angle when an object passes through the flow cytometer and larger objects tend to scatter more light. Indeed the ciliates, the largest of the three organisms,

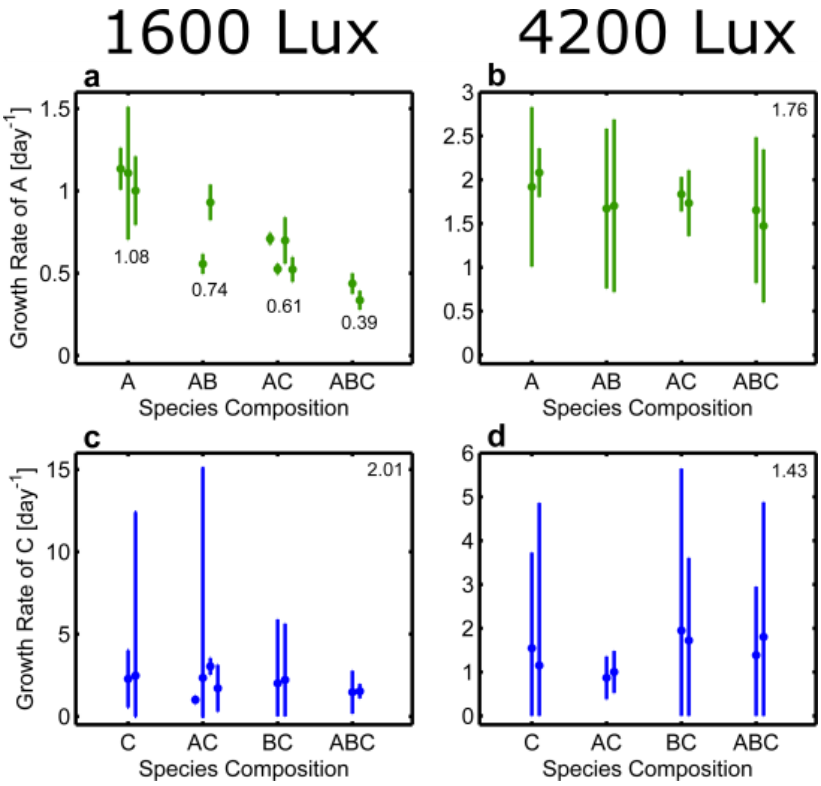

Figure 3.1: **Algae and Ciliate growth rates a,** Growth rate of algae plotted for all relevant species compositions for experiments performed at 1600 Lux (low light). The growth rate was calculated for each replicate. Error bars are 95 % confidence intervals. Numbers reported are the mean growth rate across replicates for that species composition. **b,** Growth rate of algae plotted for all relevant species compositions for experiments performed at 4200 Lux (high light). Number reported in the top right represents the mean growth rate across all replicates of all species compositions. **c,** Growth rate of ciliates plotted for all relevant species compositions for experiments performed at 1600 Lux (low light). Number reported in the top right represents the mean growth rate across all replicates of all species compositions. **d,** Growth rate of ciliates plotted for all relevant species compositions for experiments performed at 4200 Lux (high light). Number reported in the top right represents the mean growth rate across all replicates of all species compositions.

has the highest side-scatter signal. Since aggregates of bacteria are larger than single cells, they should have higher side-scatter signal. 2) The high side-scatter portion of the bacterial population stays present throughout an experiment only when ciliates are present and ciliates are known to induce bacteria to aggregate (see main text for discussion).

We performed a vortexing experiment to test if high side-scatter signal bacterial objects were indeed aggregates. In the experiment we performed flow cytometry on a sample of bacteria (Fig. 3.2a-d), vortexed the sample, and then performed flow cytometry again (Fig. 3.2e-h). We hypothesized that vortexing would break up aggregates. This hypothesis lead to two clear predictions: (1) that the number of bacterial objects would increase, due to aggregates being broken up into multiple objects, and (2) that vortexing would reduce the number of high side-scatter objects. Both predictions were confirmed. By comparing the bacterial object abundances from before and after vortexing, one can see that abundances increased after vortexing (compare densities reported in upper left corner of Fig. 3.2a-d to panels e-h). By comparing the histograms of side scatter signal of bacterial objects (Fig. 3.2i-l), one can see that the number of high side-scatter bacterial objects decreased after vortexing. In additional, one can see that vortexing does not affect the location of the peak of the histogram, which therefore presumably corresponds to single-celled bacteria and which are not disrupted by vortexing.

3.2.2 Construction of bacterial aggregate correction algorithm

In order to estimate the true number of bacterial cells, we devised a technique to estimate the number of bacterial cells in an aggregate. Having confirmed in the previous section that side-scatter signal correlates with the number of bacteria in an aggregate, we seek an expression for the number of bacteria (N) as a function of the magnitude of the side scatter signal for each object (S). We assume that for objects below a threshold value of $S < t$ then $N(S) = 1$. We set t to a value which corresponds to the right shoulder of the left mode of the distribution in Fig. 3.3b. For aggregates, that is objects with $S > t$, we take the ansatz that $N(S) = \alpha S^{\beta}$

β is an exponent which represents how the number of cells in an aggregate scales with the side-scatter signal and α is a prefactor. We chose this form because it

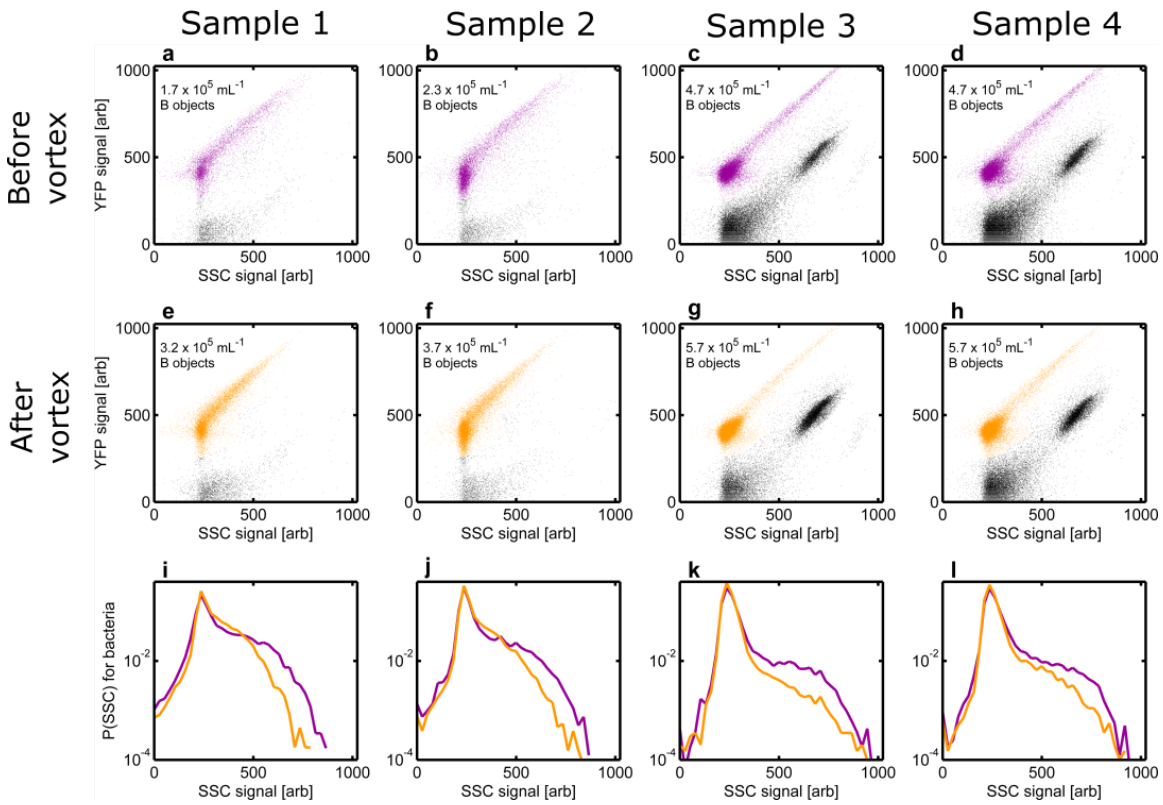

Figure 3.2: **Vortex experiments shows high SSC objects are bacterial aggregates a-d,** Yellow fluorescence signal (YFP) plotted versus side-scatter signal (SSC) for flow cytometry data from day 12 of a 1600 Lux BC coculture (**a,b**) and a 1600 Lux ABC coculture (**c,d**). Points colored purple are classified as bacterial objects. The number reported in the plot indicates abundance of bacterial objects. **e-h**, Flow cytometry data from those same samples, but after vortexing. Points colored yellow are classified as bacterial objects. In all cases the abundance of objects classified as bacteria increases after vortexing. **i-j,** Overlays of histograms of side-scatter signal of bacterial objects from before and after vortexing.

is monotonic with S, it is possible to infer these parameters from our data and scattering theory for simple objects (e.g. spheres) shows that the scaling of scattered light intensity is polynomial in particle size.

The first step in determining α and β is to define t. t should be the value of side-scatter past which bacterial objects are predominantly aggregates. We estimate this value by plotting a histogram of side-scatter signal of bacteria and marking the point at which the approximately Gaussian curve (representing single cells) turns into a tail (Fig. 3.3b). Based on visual inspection of histograms of side-scatter, we set $t = 300$.

In all flow cytometry data reported up to this point, what is reported is the *log* of the fluorescence or scattered intensity. When data files of the format used in this study (fcs2.0) are exported from the flow cytometer, all fluorescence/scattering intensities are given as integers on a scale from 0 to 1023 (10-bit ADC), where 0 represents no signal and 1023 represents a signal which saturates the photomultiplier tube. The user is given the option of whether they want the data to be log-transformed or not. Our data are log-transformed since this affords us a larger dynamic range. Therefore, our flow data report $log(S)$ rather than S. In order to follow our ansatz above it is necessary to transform our flow cytometry data from a logarithmic to a linear scale. However, the coefficients of the exponential transformation are not given by the manufacturer of the instrument, so it was necessary to infer the parameters of this transformation. To accomplish this we exported a single dataset on a linear and log scale (e.g. S and $log(S)$). From these two datasets we inferred that:

$$S = 0.0899e^{.0092log(S)}$$

(Fig. 3.3c). Therefore, our threshold on $log(S)$ of 300 is 1.41 on a linear scale.

We next inferred α and β from the vortexing experiment shown in Fig. 3.2. The key insight is that the *total* number of bacterial cells cannot change due to vortexing (although the number of detected objects does change due to vortexing disrupting aggregates). We employed the following method to determine α and β.

For a given run of the flow cytometer consider the M objects which are detected and classified as bacteria to be indexed by i. The side scatter signal from the ith

object is then S_i which contains a number of bacterial cells $N(S_i)$. For sample k we denote the side scatter signals from all M objects *prior* to vortexing as $S_{i,p,k}$. For the same sample we refer to the side scatter for all objects *after* vortexing as $S_{i,v,k}$ where i now runs to M' with $M < M'$. For example, the distribution of $log(S_{i,p,k})$ is given by the purple traces in the bottom row of panels in Fig. 3.2 and the distribution of $log(S_{i,v,k})$ by the yellow traces.

Under the assumption that the number of cells (not objects) cannot change due to vortexing the following equality must hold:

$$\sum_{i}^{M} N(S_{i,p,k}) = \sum_{i}^{M'} N(S_{i,v,k})$$

from this we find that:

$$q = \frac{\sum_{i}^{M} \alpha(S_{i,p,k})^{\beta}}{\sum_{i}^{M'} \alpha(S_{i,v,k})^{\beta}} = 1$$

Our objective then is to determine the values for α and β such that $q = 1$. We now consider $q(\alpha, \beta, k)$ which shows how the ratio of the number of inferred bacterial cells depends on α and β. A heatmap of $q(\alpha, \beta, 1)$ is shown in Fig. 3.3d with the important modification that we plot $1/q$ for values of $q < 1$. Local minima in this heatmap near 1 reveal values of α and β where our assumptions are satisfied. Note how the pairs of α and β along the ascending diagonal of this heatmap have $q \approx 1$. We now compute the same heatmap for $k = [1, 2, 3, 4]$ and compute

$$\sum_{k=1}^{4} q(\alpha, \beta, k)^2$$

again taking $1/q$ when $q < 1$ (Fig. 3.3e). This plot reveals a range of both α and β for which this sum is 4 where our assumptions are satisfied for all four samples in our vortex experiment. We applied the square to each element in the sum to especially penalize samples which had high q at the given α and β.

To narrow the range of parameters we apply a final criterion. Given our assumption that the lower mode of the distribution of S comes from single cells, we know that $N(S < 1.41) \approx 1$. Therefore we computed $N(S = 1.41)$ as a function of α and β and the result is shown in Fig. 3.3f. These criteria alone do not uniquely determine α and

β so we proceed by selecting $\alpha = 0.9$ and $\beta = 0.7$ where $N(S = 1.41) = 1.14$. This decision is subjective, but does not dramatically alter our results. For all bacterial abundances reported in the main text we use this aggregate correction algorithm.

The success of the aggregation correction algorithm can be seen in how it eliminates a spurious drop in bacterial abundances that was caused by aggregation. In Fig. 3.3h, we have plotted an abundance curve for bacteria in a 1600 Lux (low light) monoculture before and after the aggregate correction algorithm is applied. Before correction, all bacterial objects are weighted equally, meaning that an aggregate and a single cell are both counted as a single bacterium. This equal weighting leads to a spurious fall in bacterial abundance after reaching the initial peak. Notice how the apparent decline in bacterial abundance at day 1 corresponds in time to an increased level of aggregation (Fig. 3.3g). Once the bacteria eventually disaggregate, around day 5 or so, the curve returns to its peak value. These apparent changes in bacterial density are due to aggregation and disaggregation, not an actual change in bacterial cell concentration. Our aggregate correction formula successfully eliminates these spurious abundance changes.

In Fig. 3.4 and Fig. 3.5 we reproduce Figures 2 & 4 from the main text to show that the primary results of this work do not depend on the application of the aggregate correction algorithm. The only case in which there is qualitative disagreement between aggregate-corrected B abundance and not-aggregate-corrected B abundance is the 1600 Lux (low light) t_{inv}=4d invasion of bacteria on AC as depicted in panel (c) of both Fig. 2 (main text) and Fig. 3.4. In the aggregate-corrected case, Fig. 2c (main text), B invades and rises to an abundance of $\sim 7 \times 10^5\,\mathrm{mL}^{-1}$. In contrast, in the not-aggregate-corrected case, Fig. 3.4c, B does not rise significantly above its abundance at introduction and only reaches $\sim 1 \times 10^5\,\mathrm{mL}^{-1}$. The two possible explanations for this disagreement are (1) the B in this case are highly aggregated and the aggregate correction algorithm has successfully estimated the true B abundance or (2) high SSC detritus from A and/or C has bled into the flow cytometry gate used to count B and has erroneously inflated the measure of B abundance by $\sim 6 \times 10^5\,\mathrm{mL}^{-1}$.

In order to test explanation (2), we applied the flow cytometry gate used to count B to 1600 Lux (low light) AC coculture data. At almost all timepoints in this data,

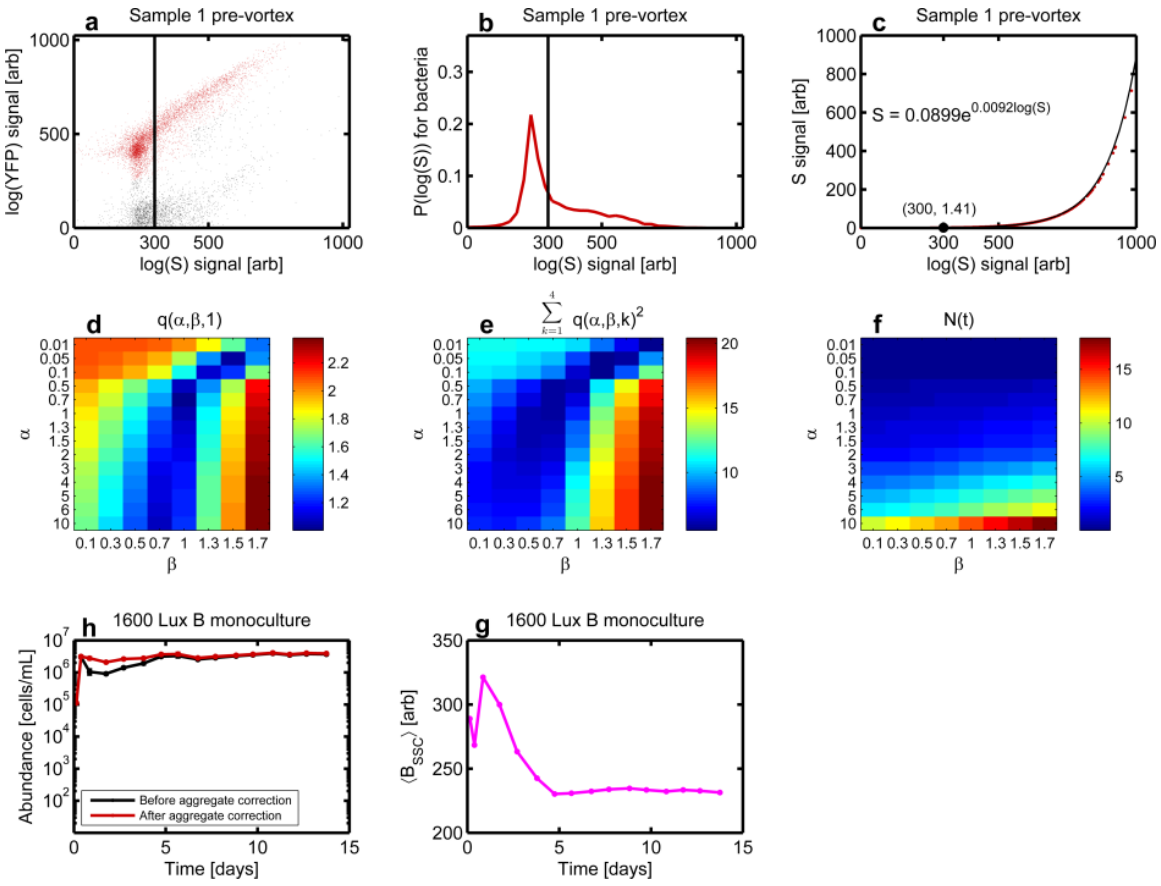

Figure 3.3: **Constructing the aggregate correction algorithm a,** YFP plotted versus SSC for flow cytometry data for sample 1 prior to vortexing (Fig. 3.2a). Red points indicate objects we have labeled bacteria. The black line indicates the threshold between single cells and aggregates at $t = 300$. **b,** Histogram of $log(S_{i,p,1})$ signal for bacteria with the threshold indicated by the line. **c,** Plotting $S_{i,p,1}$ vs $log(S_{i,p,1})$ (red) with the fitted curve (black). The threshold is indicated by the black labeled point. **d,** A heat map of $q(\alpha, \beta, 1)$ where we have plotted $1/q$ when $q < 1$. **e,** A heatmap of $\sum_{k=1}^{4} q(\alpha, \beta, k)^2$ where again we take $1/q$ for values of α and β where $q < 1$. **f,** $N(S = 1.41)$ as a function of α and β (recall $t = 1.41$). **h,** Abundance dynamics for a 1600 Lux (low light) B monoculture before (black) and after (red) aggregate correction. **g,** Mean SSC (aggregation) plotted versus time for that same 1600 Lux B monoculture.

no detritus fell within this gate. In just two cases did any AC detritus bleed into this gate and at most, $3 \times 10^3\,\mathrm{mL}^{-1}$ B abundance (aggregate-corrected) was erroneously measured. This value is two orders of magnitude smaller than necessary to explain the mismatch between Fig. 2c (main text) and Fig. 3.4c and so we therefore conclude that the successful invasion depicted in Fig. 2c (main text) is real.

3.2.3 Ciliates cause bacteria to aggregate

When bacteria from a 1600 Lux (low light) B monoculture (Fig. 3.6a) are compared to bacteria from a 1600 Lux B invasion of C (Fig. 3.6b), histograms of the side-scatter signal of bacteria show increased aggregation in the presence of the ciliates (Fig. 3.6g). Note that both histograms have a peak at low side scatter signal which corresponds to planktonic bacterial cells.

3.2.4 Ciliate induces aggregation in a Δ*csgA* *E. coli* mutant

In order to investigate the seeming necessity of bacterial aggregation in order to survive ciliate predation, we constructed a $\Delta csgA$ strain (in an MG1655 background). *csgA* encodes a structural subunit of the curli fimbrae which mediate cell-cell adhesion at temperatures below 37 °C (our experiments were all undertaken at 30 °C) [93]. As expected, monocultures of this mutant aggregate much less than monocultures of the strain used in all other experiments ($\Delta flu \Delta fimA$) (Fig. 3.7e). See the Methods section of the main text for details of strain construction and genotypes.

Because of its lack of aggregation, we hypothesized that this non-aggregating mutant would be unable to invade a culture of ciliates. Surprisingly, we found that not only did the $\Delta csgA$ bacteria invade the ciliates (Fig. 3.7d), but they also showed enhance aggregation in the presence of C as compared to monoculture (Fig. 3.7e&f).

3.3 Light level does not affect bacterial or ciliate abundance dynamics

Experiments throughout the paper are performed at 1600 Lux (low light) and 4200 Lux (high light). Here we show that the abundance dynamics of B and C are not impacted

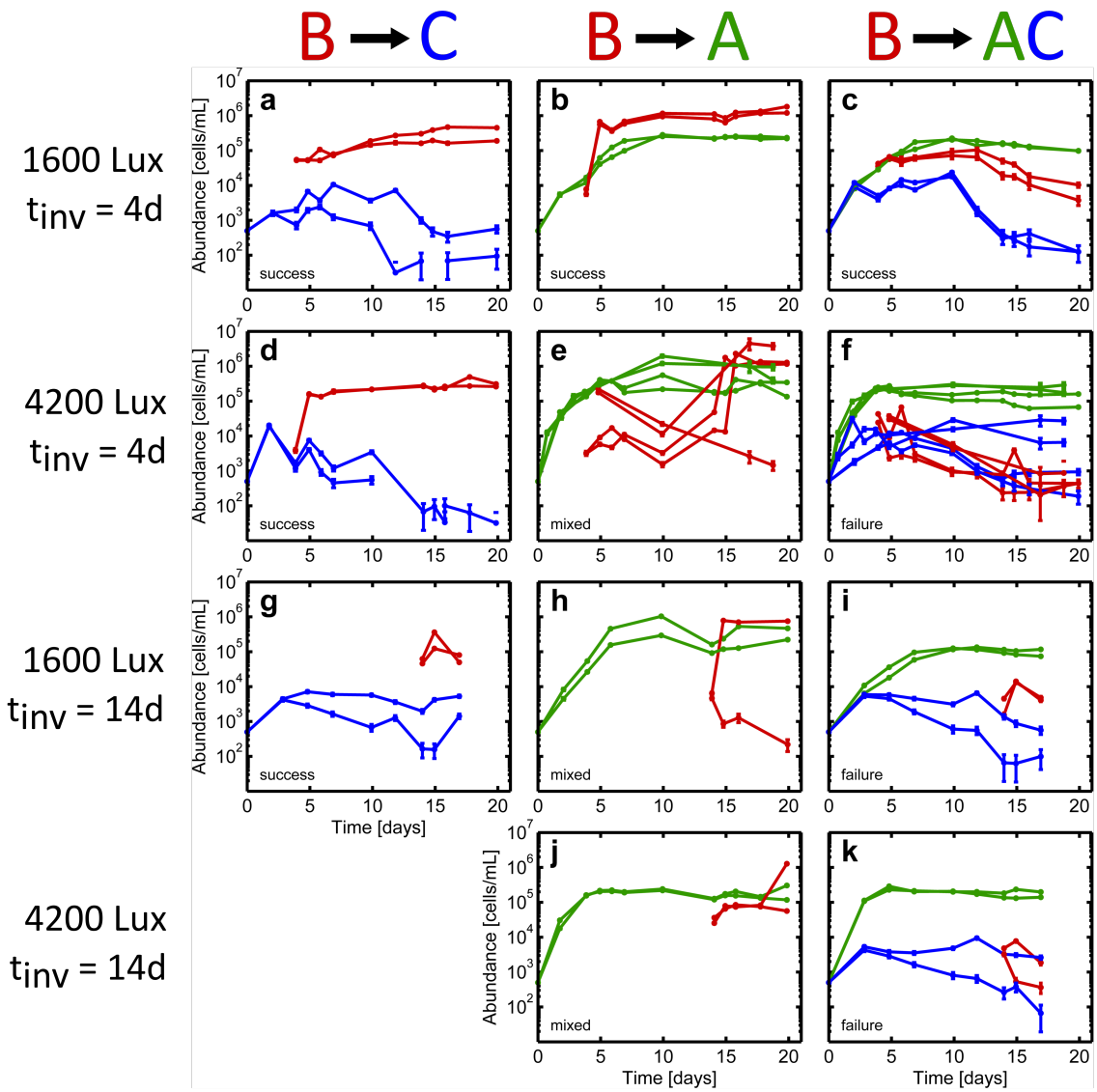

Figure 3.4: **Figure 2 from the main text but without the aggregate correction algorithm applied** Panels are identical to Figure 2 of the main text.

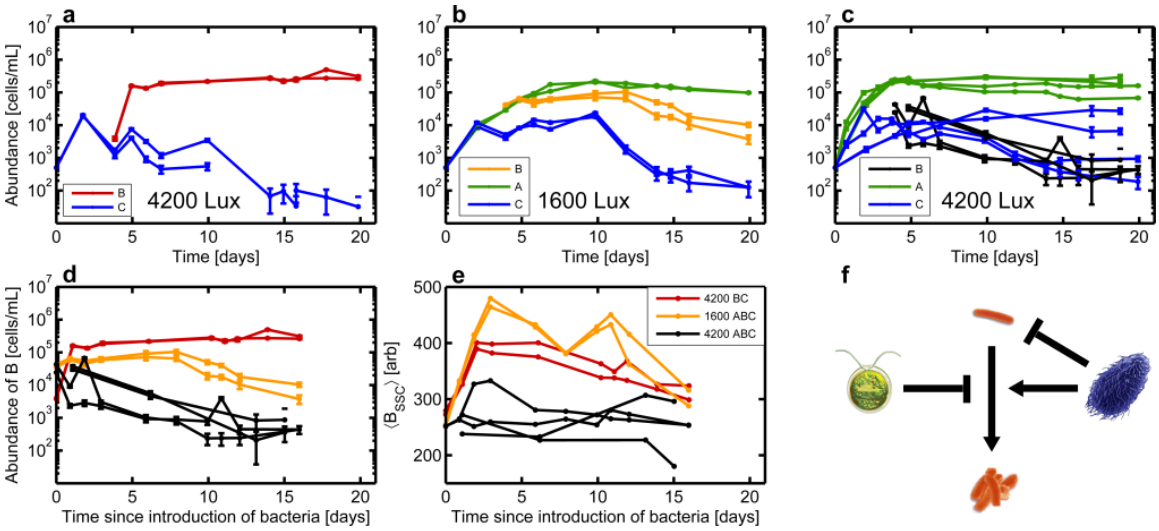

Figure 3.5: **Figure 4 from the main text but without aggregation correction algorithm applied** Panels are identical to Figure 4 of the main text.

by illumination at either level of illumination. When comparing bacterial abundance dynamics between low light and high light conditions for the co-culture experiments, B behaves identically across light levels regardless of the species composition: B monoculture, AB co-culture, or BC co-culture (Fig. 3.8a,b&c). The only species composition in which B behaves differently across light levels is the ABC co-culture (Fig. 3.8d). We argue in the main text that this effect is due to a higher-order interaction in the community.

The same independence of dynamics relative to light level is true for ciliates (Fig. 3.8). We note that there is substantial variability in the C abundance dynamics. We believe that these differences reflect differences in the state of the ciliate population prior to starting the experiment (e.g. small variations in the growth phase at time the experiment was initiated).

3.4 Algae-bacteria interactions

3.4.1 When algae is at sufficiently high density, it stochastically prevents bacterial invasion

To further investigate the inhibition of B by A we performed a set of invasion experiments where B was introduced to A at $t = 0$ days (co-culture), 1 day, 3 days

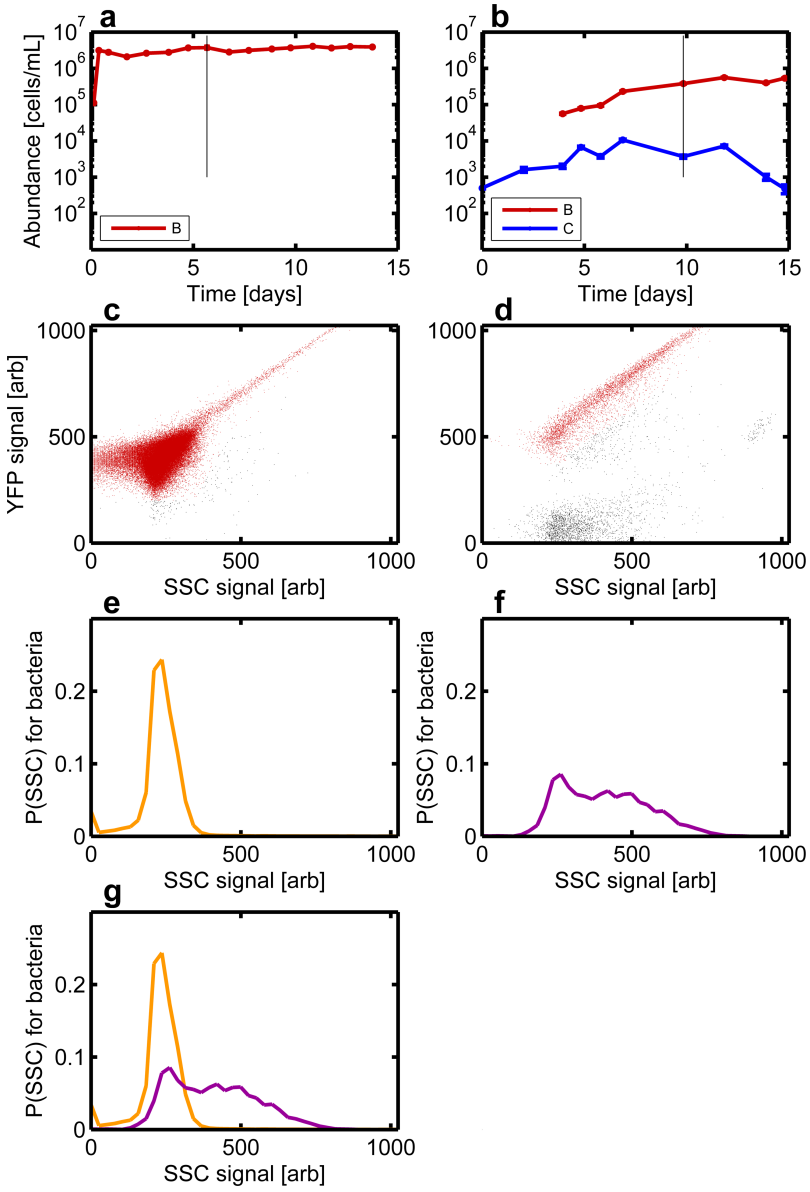

Figure 3.6: **Ciliates induce bacteria to aggregate a,** Abundance dynamics for a 1600 Lux (low light) monoculture of B. Black line indicates the time point for which we plot flow cytometry data in **c. b,** Abundance dynamics for a 1600 Lux (low light) B invasion of C. The black line indicates the time point for which we plot flow cytometry data in **d. c,d** Plotting yellow fluorescence (YFP) versus side-scatter (SSC) for flow cytometry data taken from the indicated day in **a** and **b** respectively. Red-colored points indicate objects we have labeled as bacteria. **e,f**, Histograms of the SSC signal for all objects labeled as bacteria in **c** or **d**. **g,** Overlay of the histograms.

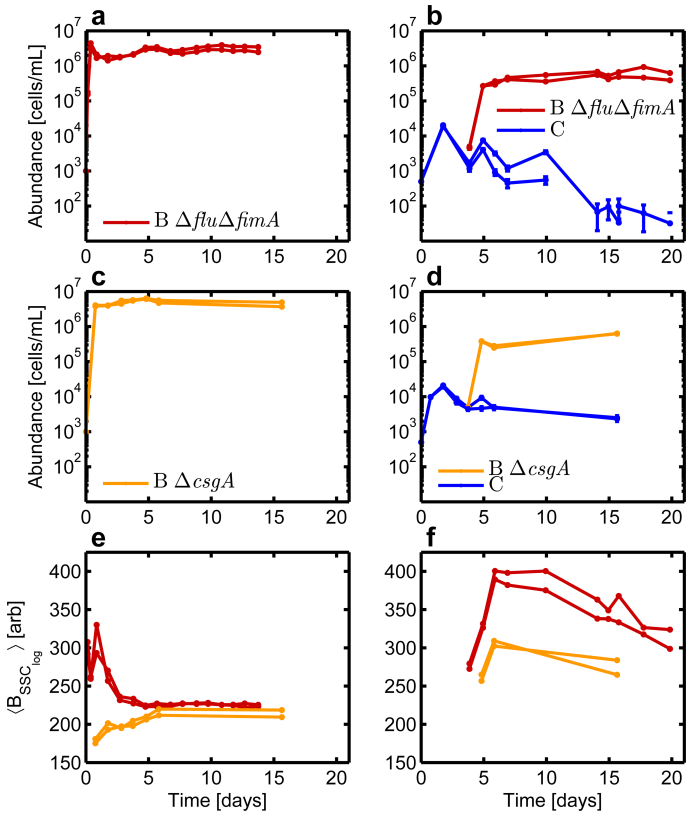

Figure 3.7: **Ciliate induces aggregation in Δ*csgA* *E. coli*** All experiments in this figure are at 4200 Lux (high light). **a,** Abundance dynamics for two replicates of a B monoculture, using strain $\Delta flu \Delta fimA$. This is the strain used throughout this study. **b,** Abundance dynamics for two replicates of a B invasion on C, also using the $\Delta flu \Delta fimA$ strain of B. **c,** Abundance dynamics for two replicates of a B monoculture, using strain $\Delta csgA$. **d,** Abundance dynamics for two replicates of a B invasion on C, also using the $\Delta csgA$ strain of B. **e,** Mean side-scatter plotted versus time for the bacteria in panels **a** and **c**. **f,** Mean side-scatter plotted versus time for the bacteria in panels **b** and **d**.

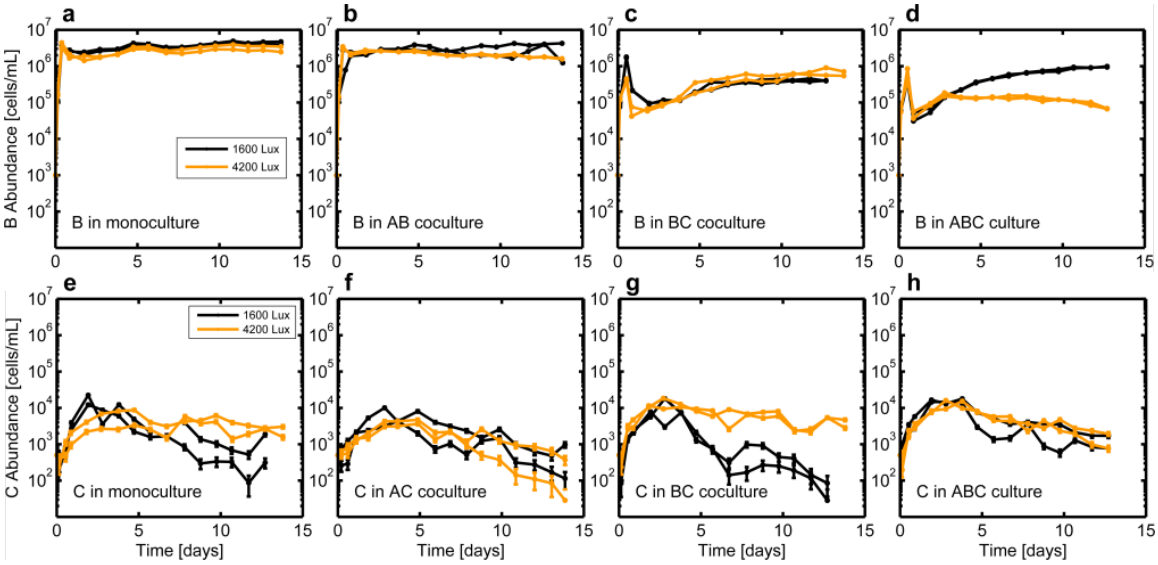

Figure 3.8: **Bacterial or ciliate abundance dynamics with different light levels and community composition a-d,** Abundance dynamics for two replicates each of B in 1600 Lux and in 4200 Lux B monoculture (**a**), AB co-culture (**b**), BC co-culture (**c**), and ABC culture (**d**). Legend in **a** applies to **b-d**. **e-h,** Abundance dynamics for two replicates each of C in 1600 Lux and in 4200 Lux C monoculture (**e**), AC co-culture (**f**), BC co-culture (**g**), and ABC co-culture (**h**). Legend in **e** applies to **f-h**.

and 4 days all in high light (4200 Lux) conditions. We found that A did not suppress B when A was at densities below $1 \times 10^5\,\mathrm{mL}^{-1}$ at time of bacterial introduction (Fig. 3.9 a,b), but that suppression did occur when B was introduced to high density A (Fig. 3.9 c,d). Of those six high-density A cultures which suppressed bacterial invasion, three completely prevented bacterial invasion (low bacterial densities of $\sim 1 \times 10^3\,\mathrm{mL}^{-1}$ even after two weeks), while the other three high-density A cultures allowed bacteria to grow to high density over the period of approximately two weeks following bacterial introduction.

3.4.2 Algae must be physically present and illuminated to inhibit bacterial invasion

We performed an experiment to test the importance of the physical presence of algae in the suppression of bacterial invasions. A culture of algae was grown in a 1 L Erlenmeyer flask for ten days in a shaker incubator at approximately 4000 Lux, 30 °C, and 175 RPM. The algae culture was then transferred to vials and inoculated with bacteria at a density of $1 \times 10^5\,\mathrm{mL}^{-1}$. These vials were placed in the culture devices

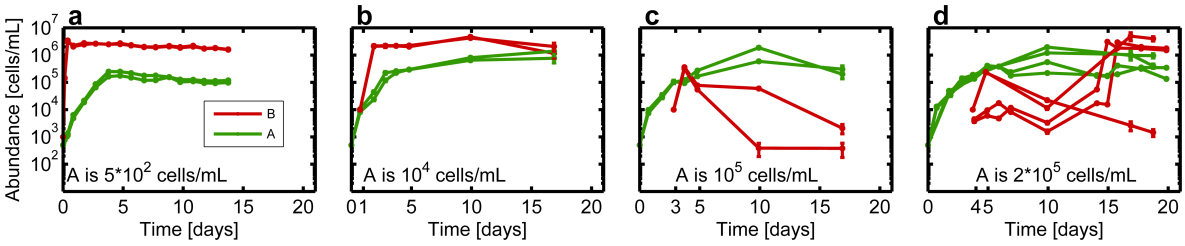

Figure 3.9: **Outcome of bacterial invasion in high density algal cultures is stochastic** Abundance dynamics of algae and bacteria when bacteria is grown in co-culture with algae (**a**), or introduced into an algae monoculture at day 1 (**b**), day 3 (**c**), or day 4 (**d**). Text inside panels indicates density of algae at time of introduction of bacteria. All experiments in this figure performed at 4200 Lux (high light).

used for the experiments shown in the main text. In two replicates the brightness was set to 4200 Lux (high light) (Fig. 3.10a) while in the other two replicates the brightness was set to 0 Lux (no light) (Fig. 3.10b). Bacteria and algae abundance were then measured by flow cytometry.

In the other half of the experiment, the algae culture was filtered through a 0.22μm PES membrane filter before being distributed across vials and inoculating bacteria. Once again the vials were set to 4200 Lux (Fig. 3.10c) and 0 Lux (Fig. 3.10d).

The only condition in which bacterial invasion was inhibited was the condition with lights on and algae physically present (Fig. 3.10a). In all other cases: lights-off, algae filtered out, or both, bacteria invaded immediately. The necessity of light implies that algae's photosynthetic metabolism must be active to suppress bacterial invasion.

The mechanism by which the physical presence of algae is necessary to inhibit invasion remains unclear. However, we present a few possible interpretations of this result: (1) Algae suppresses bacterial invasion by secreting a toxic compound, one that they only begin producing when they sense the presence of bacteria (microbes can be stimulated to emit toxins by presence of other microbes [94]) (2) Algae suppresses bacterial invasion by secreting a toxic compound which can be degraded by bacteria. In this scenario the toxin in the spent algal medium is rapidly degraded by the bacteria, but in the case where algae are present the production rate of the toxin exceeds the bacterial degradation rate of that toxin. This possibility motivated us to test H_2O_2 as the mechanism since algae produce reactive oxygen species and bacteria degrade them via catalase. Our experiments showed that hydrogen peroxide is not the

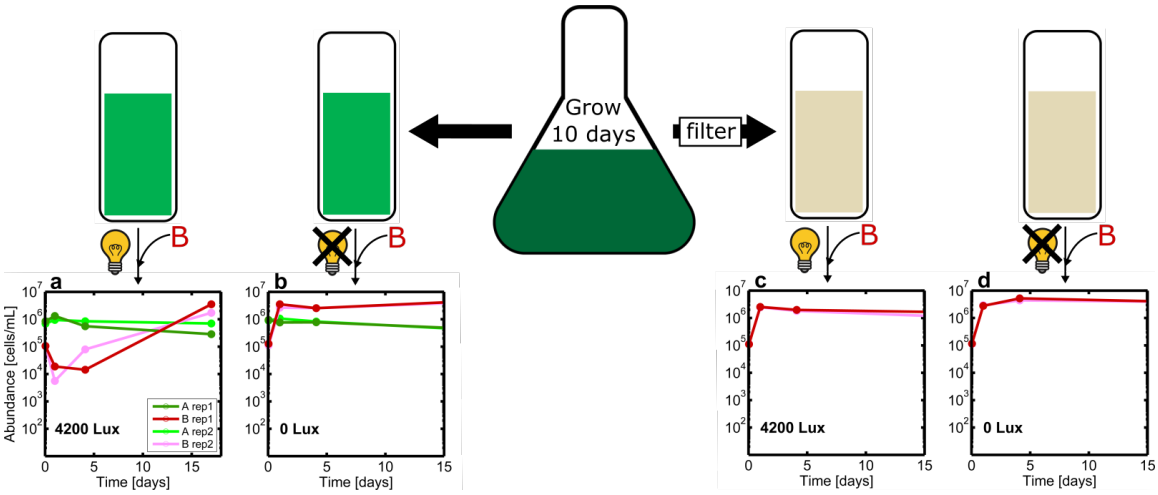

Figure 3.10: **Algae must be physically present and illuminated to inhibit bacterial invasion** Algae are grown for 10 days in large volume in a flask of 1/2xTaub .01%pp3 at 30 °C in a shaker-incubator while being illuminated at approximately 4000 Lux. Half the culture is filtered. Then unfiltered (**a,b**) and filtered (**c,d**) algae culture is distributed across vials. Bacteria is inoculated at density 1×10^5 mL^{-1} and the vials are then grown at 4200 Lux (high light) (**a,c**) or 0 Lux (no light) (**b,d**). Abundance dynamics after inoculation with bacteria are plotted. There are two replicates for each condition.

mechanism of inhibition (see discussion below and Fig. 3.12). (3) Physical contact between algae and bacteria is necessary for the mechanism of invasion suppression (flagella have been seen to mediate interactions between microbes [95]). (4) The most pathological possibility: algae suppresses bacterial invasion by secreting a toxic compound that is larger than the pores of the 0.22μm filter.

3.4.3 There exists a threshold light level below which algae cannot suppress bacterial invasion

We performed an experiment to test the importance of light when it comes to algae suppressing bacterial invasion. A culture of algae was grown in a flask (1 L) for ten days in a shaker incubator at approximately 4000 Lux, 30 °C, and 175 RPM. The algae culture was then transferred to vials and inoculated with bacteria at bacterial density 2×10^4 mL^{-1}. These vials were placed in the temperature/light-control systems that the invasion and co-culture experiments in the main text were performed in. In sets of two replicates the brightness was set to 600 Lux (extra low light) (Fig. 3.11a), 1600 Lux (low light) (Fig. 3.11b), 2900 Lux (medium light) (Fig. 3.11c), and 4200 Lux (high light) (Fig. 3.11d). Bacteria and algae abundance were then measured by flow

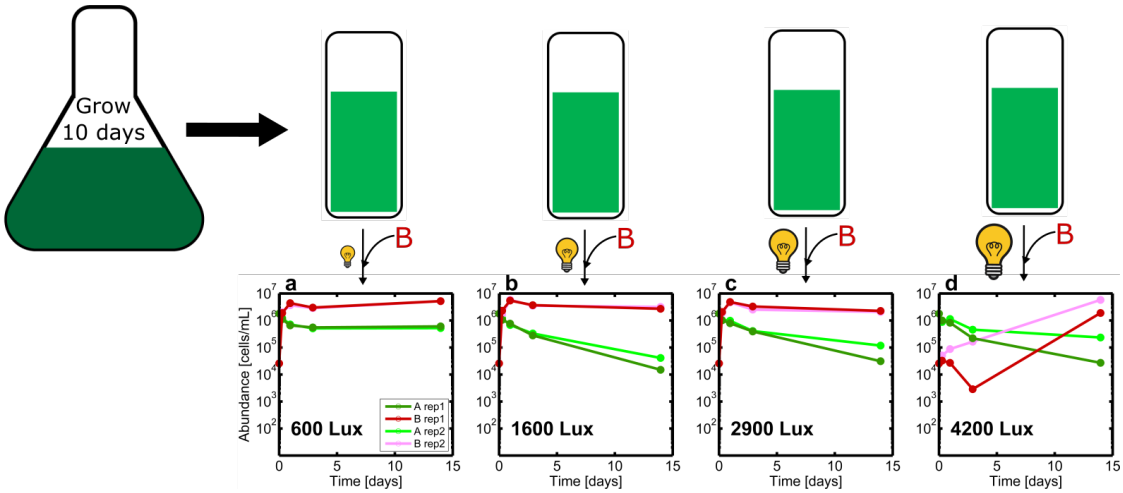

Figure 3.11: **There exists a threshold light level below which algae cannot suppress bacterial invasion** Algae are grown for 10 days in large volume in a flask of 1/2xTaub .01% proteose peptone No.3 at 30 °C in a shaker incubator while being illuminated at approximately 4000 Lux. Algae culture is then distributed across vials. Bacteria is inoculated at density $2 \times 10^4\,\mathrm{mL}^{-1}$ and the vials are then grown at 600 Lux (extra low light) (**a**), 1600 Lux (low light) (**b**), 2900 Lux (medium light) (**c**), or 4200 Lux (high light) (**d**). Abundance dynamics after inoculation with bacteria are plotted. There are two replicates for each condition.

cytometry.

Algae was only able to suppress bacterial invasion at the highest light level (Fig. 3.11d). At all other light levels the bacteria invaded immediately. This contradicts the results of the main text in the sense that in experiments reported in the main text, 1600 Lux monocultures of algae were able to suppress bacterial invasion as long as the algae density was high enough, whereas here, for example (Fig. 3.11b), a 1600 Lux monoculture of high-density algae was not able to suppress bacterial invasion. This result implies that the physiology of algae grown in the flask in the shaker-incubator is significantly different from the physiology of algae grown in the temperature/light-control systems and that the suppression of bacterial growth by algae depend on the growth history of the algal culture or the precise culture conditions.

3.4.4 Hydrogen peroxide is not responsible for A inhibiting B invasion

Because metabolically active algae are known to produce reactive oxygen species [96], we tested if H_2O_2 was responsible for algae's ability to suppress bacterial invasion. To measure H_2O_2 we used the iodine based absorbance method of Junglee et. al. [97]. Absorbance values from cultures were compared to those taken for solutions with

known concentrations of hydrogen peroxide.

In a control experiment we determined the concentration of H_2O_2 necessary to inhibit bacterial growth. Bacteria were inoculated into a 96-well plate in wells that contained 1/2x Taub .01% proteose peptone No. 3 and H_2O_2 in concentrations that ranged from 1M to 1nM. We inoculated bacteria at both $1 \times 10^4\,\mathrm{mL}^{-1}$ and $1 \times 10^5\,\mathrm{mL}^{-1}$. The bacteria were grown in a plate reader at 30 °C and abundance was measured continuously via absorbance at 600 nm. For the low B inoculum, 1mM initial H_2O_2 concentration was necessary to prevent growth while for the high B inoculum 10mM initial H_2O_2 concentration was necessary to prevent growth (Fig. 3.12a). Measurements of H_2O_2 in these cultures one day after inoculation showed that bacteria who successfully grew eliminated the H_2O_2 (Fig. 3.12b).

We then measured the H_2O_2 in conditions where B successfully invaded A and also conditions where its invasion was inhibited by A. Specifically, we took H_2O_2 measurements in the experiment from Fig. 3.11. No H_2O_2 was detected at any point in any of the systems, and thus we conclude that H_2O_2 is not the mechanism by which algae suppresses bacterial invasion. We cannot rule out other reactive oxygen species by this assay.

3.4.5 Algal-bacterial adhesion and invasion supression

By closely examining flow cytometry data from the experiment in Fig. 3.11, it can be seen that bacteria are sticking to algae. Recall that in this experiment algae were grown in a flask for ten days and were then distributed across vials. These vials were inoculated with bacteria and then placed in the temperature/light-control systems at four different light levels. By looking at flow cytometry data taken 6 hours into the experiment, one can see that some of the bacteria have stuck to algae. This is evident from the presence of a small cloud of objects distinct from algal signals that are both high YFP and chlorophyll. At this time-point, the bacteria form a tight cloud around YFP = 500 (Fig. 3.13b,e). When YFP signal is plotted versus Chlorophyll signal for flow cytometry from this same time point, one can see that there is a cloud with that same YFP value, that also has high chlorophyll, and is distinct from the main cloud of algae points (beige points, Fig. 3.13c,f). These facts taken together indicate a fraction of the bacteria have stuck to the algae. The reader may wonder why,

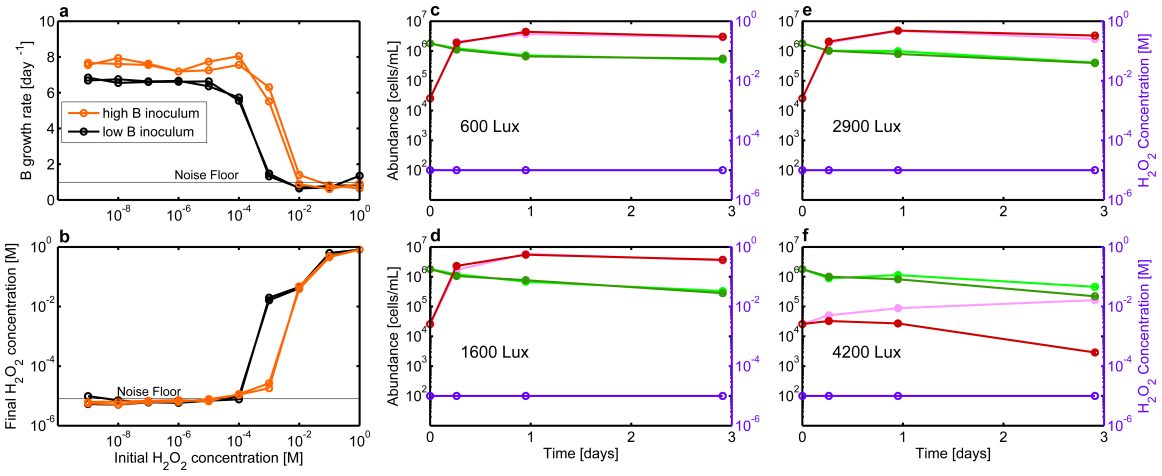

Figure 3.12: **H_2O_2 is not the mechanism through which A inhibits B growth a,** Growth rate of bacteria as a function of the initial H_2O_2 concentration for both high and low inoculum. Growth media is 1/2x Taub .01% proteose peptone No. 3. High B inoculum is $1 \times 10^5\,\mathrm{mL}^{-1}$, while low B inoculum is $1 \times 10^4\,\mathrm{mL}^{-1}$. Noise floor in growth rate was calculated by measuring the growth rate (via regression) on synthetic data generated from a normal distribution with the same mean and variance as observed experimentally (e.g. absorbance fluctuations in wells where no growth occurs). **b,** Final H_2O_2 concentration as function of the initial H_2O_2 concentration in the same experiment as **a**. When final H_2O_2 concentrations are calculated based on absorbance measurements, background noise in the absorbance always leads to at least 1×10^{-5}M concentration of H_2O_2 being calculated and so that is where we set our noise floor. **c-f** Abundance curves from the experiment in Fig. 3.11. At each time point, a sample was taken and its H_2O_2 level was measured. H_2O_2 levels were below our limit of detection at all time points.

when both bacteria and algae have significant YFP signal, the cloud of B-stuck-to-A objects does not appear on the plot to have a YFP value that is the sum of both. Recall from the aggregate correction section of this supplement that flow cytometry signals for an object should be understood as the log of an object's intensity for a given scattering/fluorescence channel, and thus values do not add linearly on these plots.

We next asked: does the degree of bacteria sticking to algae depend on the degree to which the invasion is inhibited? Could differential sticking be responsible for invasion suppression? In the experiment from Fig. 3.11, there were six immediately successful invasions, one of which is depicted in Fig. 3.13a, and two suppressed invasions, one of which is depicted in Fig. 3.13d. We used a strict gate to determine the size of the population of bacteria stuck to algae (Fig. 3.13c&f). For the six systems shown in Fig. 3.11 where bacteria invade successfully immediately, we find that the fractional abundances of bacteria stuck to algae ($\frac{B-stuck-to-algae}{B-not-stuck-to-algae}$) are: 3.7 $\pm$ 0.1%, 3.7 $\pm$ 0.1%, 2.8 $\pm$ 0.1%, 2.5 $\pm$ 0.1%, and 2.9 $\pm$ 0.1%. Error bars are estimated assuming Poisson counting error. For the two systems where the invasions were suppressed, we find 4.8 $\pm$ 0.9% and 7.7 $\pm$ 1.4%. A two-sample t-test assuming unequal variances fails to reject the null hypothesis that the average fraction of B cells stuck to A differs between successful and inhibited invasions ($p = 0.28$). We note the small samples size means this result should not be taken too seriously. However, based on the inconsistency between the two values in the case of the suppressed invasions, and the near-overlap between the error bars of one of the values for suppressed invasion (4.8 $\pm$ 0.9%), and two of the values for immediately successful invasion (both 3.7 $\pm$ 0.1%), we suggest it is not reasonable to believe that there is a substantially larger fraction of B adhered to A when B invasions are supressed.

3.4.6 Physical collisions between bacteria and algae are frequent even when algal density is low

In the main text we conjectured that the density dependence of algal inhibition of bacteria might arise from more frequent cell-to-cell contact when algal densities are high. Here we estimate the frequency of this contact and find that bacteria come in contact with algae with high frequency even at low algal densities.

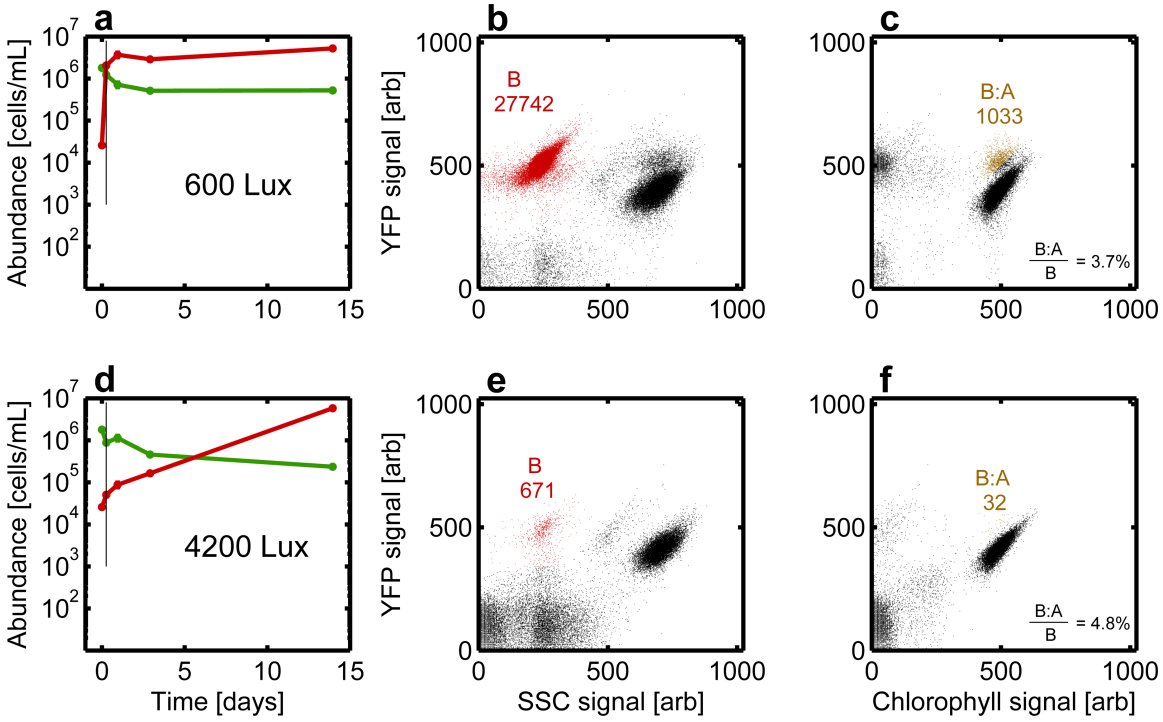

Figure 3.13: **A small fraction of bacteria adhere to algae a,** Abundance curves for algae and bacteria taken from one of the 600 Lux replicates of the algae flask experiment in Fig. 3.11. The black line marks the time point for which flow cytometry data is plotted in **b&c. b,** YFP signal plotted versus SSC signal for flow cytometry data from aforementioned timepoint. Points in red mark objects classified as bacteria. Number indicates the number of these objects. **c,** YFP signal plotted versus Chlorophyll signal for flow cytometry data from that same timepoint. Points in gold mark objects classified as algae with bacteria stuck to them. Number indicates the number of these objects. Percentage indicates how many of these algae-stuck-to-bacteria objects there are as a fraction of the normal bacteria. **d,e&f,** The same analysis as in the top row of this figure, but instead with one of the 4200 Lux replicates from Fig. 3.11.

We calculate the number of algae that a bacterium encounters in one second. From Stocker et. al, $E_B = 4\pi N_A(D_A + D_B)(r_A + r_B)T$ where E_B is the number of algae a single bacterium encounters in time T, N_A is the concentration of algae, D_A and D_B are the diffusivity of algae and bacteria respectively, and r_A and r_B are the radii of algae and bacteria respectively. Taking T to be 1 second, we will attempt to calculate a lower bound on E_B, the number of algae a bacterium encounters in one second. For N_A, we use $500\,\mathrm{mL}^{-1}$ ($5 \times 10^8\,\mathrm{m}^{-3}$), the starting concentration of algae, and therefore the lower bound. From Stocker, $D_B = \frac{U^2\tau}{3}$ where U is the speed of the bacterium and τ is the turning rate. We take τ to be one turn per second [98]. In our systems, U is not the swimming speed, but rather the speed imparted on the bacterium through stirring. The stir-bar in the vial turns at 450 RPM and is of diameter 1.5 cm. Assuming that the average bacterium will move at the same speed as the point halfway along the radius of the stir-bar, we obtain speed $0.17\,\mathrm{m\,s}^{-1}$. This value is consistent with the observation that a drop of food coloring applied to the top of the vial while the vial is being stirred distributes throughout the vial instantaneously by eye. D_B is therefore 0.0096 $\frac{\mathrm{m}^2}{\mathrm{s}}$. We set $D_A = 0$ in the interest of establishing a lower bound. We take r_B to be 1 µm and r_A to be 1 µm. Taken together, we calculate $\frac{E_B}{T}$ to be 180 collisions per second. That is 180 algae encountered per second by a single bacterium.

3.4.7 There may be a volatile chemical responsible for algae inhibition of bacteria

At one point we performed an experiment in which we sampled every half hour after the invasion of bacteria on to algae and looked at the culture under the microscope. The point of the experiment was to see if we could visually identify the difference between cultures where bacteria were successfully invading versus cultures in which they did not. Unfortunately, every time we tried this experiment, the bacteria would always successfully invade immediately, even at light levels and algae densities where they had always been unsuccessful in the past.

The takeaway of that experiment is that something about sampling frequently allows bacteria to invade successfully. Perhaps sampling replenishes oxygen and helps the bacteria grow or gets rid of a volatile harmful chemical the algae excretes.

3.5 Spent Media Experiments

3.5.1 Neither algae nor ciliates compete with bacteria for nutrients

We considered the possibility that nutrient competition could account for the inhibition of B by A and the failure of B to invade AC communities. In the undefined medium used here it is possible that A and C alone do not consume all of the available carbon and nitrogen but in co-culture they consume an essential nutrient for bacterial growth. To investigate this possibility we performed a series of spent media experiments where communities were grown in our growth chambers, samples were harvested and then all cells were removed by filtration (example shown in Fig. 3.14a). B was then inoculated into this spent medium and grown to saturation K_B in a 96-well plate where its density was assayed by flow cytometry after two days of growth (Fig. 3.14a). We find that B is able to grow on the spent medium of A, C and AC communities to a saturating density that is identical to growth on fresh medium irrespective of the time at which the spent media was taken (Fig. 3.14c). This result rules out the presence of nutrient competition between these three species as the source of the invasion outcomes in the main text. In addition, the fact that B grows rapidly to maximum density in spent medium harvested from A communities at high algal densities shows that nutrient competition is not the cause of A inhibiting B invasions.

To further investigate the role of nutrients in the inhibition of B by A we harvested spent medium from an A community after a B invasion at several time points (Fig. 3.14b). We then filtered out both A and B and then inoculated fresh B cells at low density in this spent medium. Remarkably, B was able to grow on spent medium from an AB invasion experiment so long as the spent medium was taken prior to the invading B population reaching high density. After the point where invading B reach high density, B can no longer grow to high density on spent medium (Fig. 3.14d). This result shows that the inhibition of B by high density populations of A limits the ability of B to consume nutrients. This experiment further suggests that the inhibition of B by A may be caused by a volatile compound or direct physical contact rather than a soluble toxin.

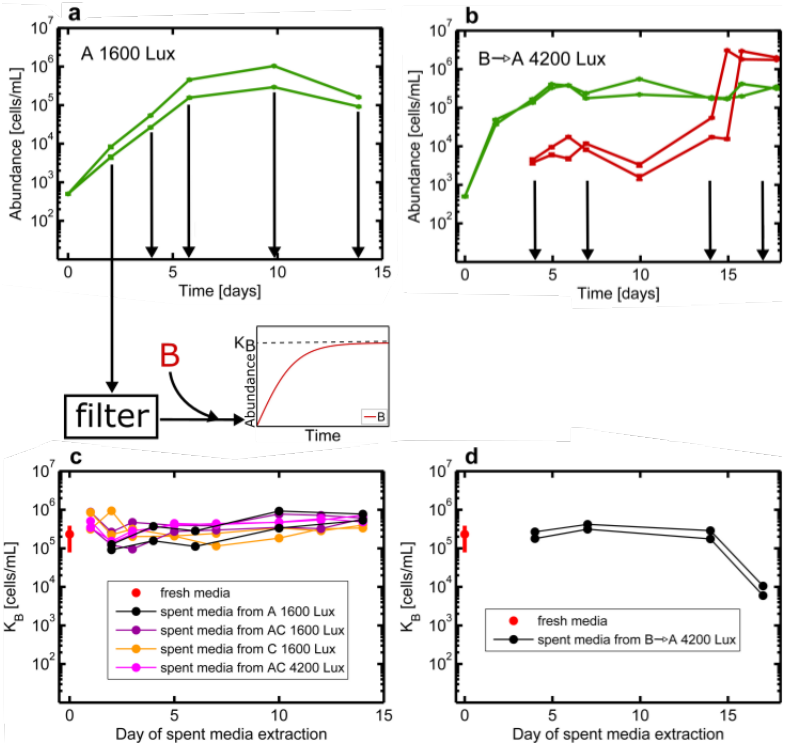

Figure 3.14: **Algae and ciliates do not consume bacterial nutrients a,** Abundance plotted versus time for two replicates of an algae monoculture at 1600 Lux (low light). Black arrows indicate the time points when media is extracted and filtered. Bacteria is then grown on this spent media in a microtiter plate until it reaches saturation. The saturating density K_B is measured via flow cytometry. This experiment is also performed on a 1600 Lux C monoculture, a 1600 Lux AC coculture, and a 4200 Lux AC coculture. **c,** K_B is plotted for all the conditions. The x-axis indicates the day of extraction of spent media. **b,** The same spent media extraction experiment is performed on a monoculture of algae that is invaded with bacteria. This means that the spent media taken from this culture has already been exposed to bacteria. **d,** K_B plotted versus day of spent media extraction for the experiment in **b.**

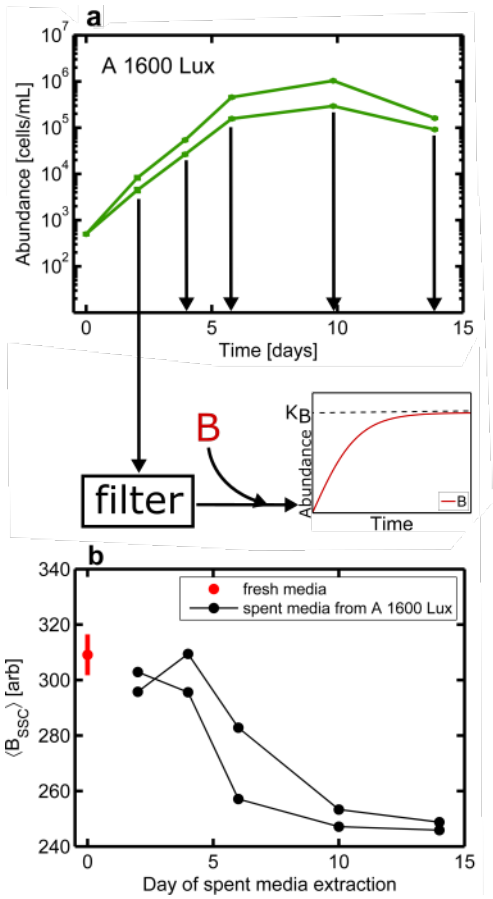

Figure 3.15: **Algae spent media de-aggregates bacteria a,** Abundance plotted versus time for two replicates of an algae monoculture at 1600 Lux (low light). Black arrows indicate the time points at which media is extracted and filtered. Bacteria is then grown on this spent media in a microtiter plate until it reaches saturating density K_B **b,** Mean side-scatter of the bacteria after they reach K_B is plotted versus time of spent media extraction. The point at time zero represents the mean-side scatter of bacteria that were grown on fresh media.

3.5.2 Algae spent media de-aggregates bacteria

The spent media experiment shown in Fig. 3.14a can also be analyzed to show that algae spent media has a de-aggregating effect on B. Two replicates of a 1600 Lux (low light) A monoculture were grown in the temperature/light-control systems. Samples were harvested at multiple time points and all algae cells were removed by filtration. B was then inoculated into this spent media (Fig. 3.15a) and grown to saturation in a 96-well plate where B's density K_B was assayed by flow cytometry after two days of growth. The mean side-scatter signal of bacteria decreased as a function of time of spent media extraction in both replicates (Fig. 3.15b). The longer the duration of algal growth the greater is the de-aggregation of B grown on spent medium.

3.5.3 Ciliates present in algal spent media is not sufficient to prevent bacterial invasion

In the main text we show that a 3-body interaction between algae, bacteria, and ciliates prevents the invasion of the bacteria. We thought to ask if this interaction requires the physical presence of the algae or if spent media from the algae is sufficient. Our objective was to determine whether the impact of algal spent medium de-aggregation altered the predation pressure of B by C.

The experiment was performed in a similar manner to the spent media experiments in the main text. Two replicates of a 1600 Lux (low light) A monoculture were grown in the temperature/light-control systems. Samples were harvested at multiple time points and all algae cells were removed by filtration. B along with C was then inoculated into this spent media (Fig. 3.16a) and grown to saturation in a 96-well plate where B's density K_B was assayed by flow cytometry after two days of growth. K_B did not vary with the time of spent media extraction from the algae monocultures and K_B in algae spent media was only, on average, 46% lower than for fresh media (Fig. 3.16b).

3.6 Live-dead staining experiments

When gating on clouds of points of flow cytometry data, an assumption is made that the cells which are fluorescent are alive and thus a good measure of true abundance of live cells. We base this assumption on the fact that algae cells fluoresce significantly differently in chlorophyll when alive as compared to dead [99]. Nevertheless, we attempt here to use Sytox Green Dye to assay the number of dead cells. Sytox Green is a nucleic acid stain. Sytox Green stains dead cells positively in the YFP channel.

We performed the Sytox experiment on algae in four cases, two replicates of a day 4, 1600 Lux (low light) ABC co-culture, and two replicates of a day 4, 4200 Lux (high light) ABC co-culture. In each case, flow cytometry data was taken before the application of Sytox (Fig. 3.17a), then Sytox Green was added at a concentration of 100nM, incubated for 10 minutes, and then flow cytometry was performed again (Fig. 3.17b). In each case, a new "dead algae" cloud with saturating YFP signal emerged after application of Sytox. Across the four cases, these dead cells made up 31 $\pm$ 11%

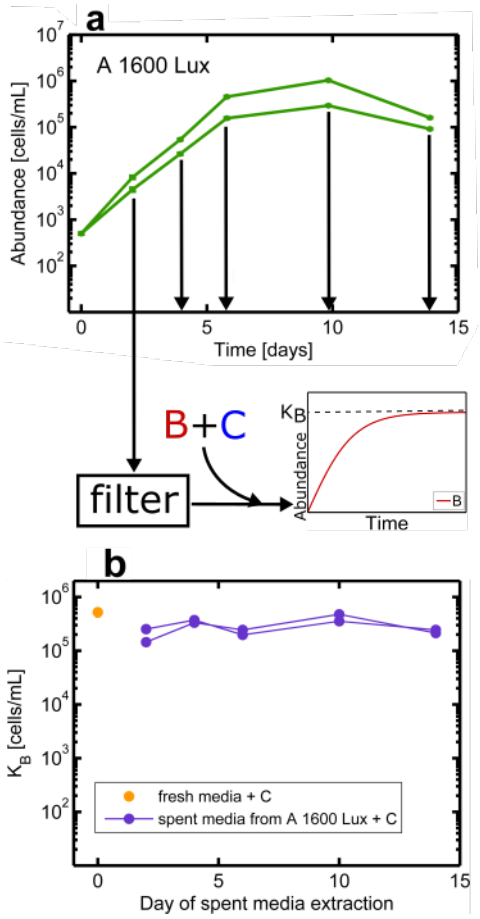

Figure 3.16: **Algae spent media alone does not largely alter C predation on B a,** Abundance plotted versus time for two replicates of an algae monoculture at 1600 Lux (low light). Black arrows indicate the time points at which media is extracted and filtered. Bacteria and ciliates are then grown together on this spent media in a microtiter plate, allowing B to reach saturating density K_B. **b,** K_B, measured by flow cytometry, is plotted versus time of spent media extraction.

of the total algae cells, suggesting up to a third of algal cells are dead. This estimate is likely to be an overestimate due to high stain concentrations as explained below.

The Sytox experiment was also performed on bacteria in four cases, two replicates of a day 14, 1600 Lux B monoculture, and two replicates of a day 14, 4200 Lux B monoculture. Once again a high YFP portion separated out from the main cloud after application of Sytox (Fig. 3.17c&d). In the case of bacteria, dead cells made up 3.6± 2.1% of the total bacterial cells (average and standard deviation across four replicate systems). The Sytox experiment was also performed on ciliates, but the results are impossible to interpret given that Sytox just translated the entire cloud of ciliates to a higher YFP region (Fig. 3.17e&f) and no separation is observed.

We believe that in the case of algae and ciliates, Sytox concentration was too high, and thus the estimate of dead cells is an overestimate. Note what happens when a 5-fold higher Sytox concentration is used to stain algae (Fig. 3.18c). The estimate of percentage of dead cells increases from 31 ± 11% to 51 ± 21% (average and standard deviation across four replicates). This increase indicates that we are in a regime of high Sytox concentration where even live cells are being stained with Sytox Green. Further supporting this conclusion is the fact that the main cloud of algae points in Fig. 3.18b&c is also becoming distorted toward high YFP, this arises from excess Sytox staining live cells.

The Sytox Green staining protocol suggests performing repeated staining experiments at varying concentrations of dye and choosing the highest concentration where a subset of the presumably live cells are not stained. Further, the ability of cells to expel the dye depends on their physiological state (e.g. exponential versus stationary phase). Since this state varies throughout our experiment we deemed it infeasible to perform Sytox staining at many time points for the many different conditions studied here. However, the staining data we do have supports the claim for algae and bacteria that less than ∼30 % of the algal population or ∼5 % of the bacterial population are dead. We note that these fractions are small relative the the changes in abundances that occur during our experiment.

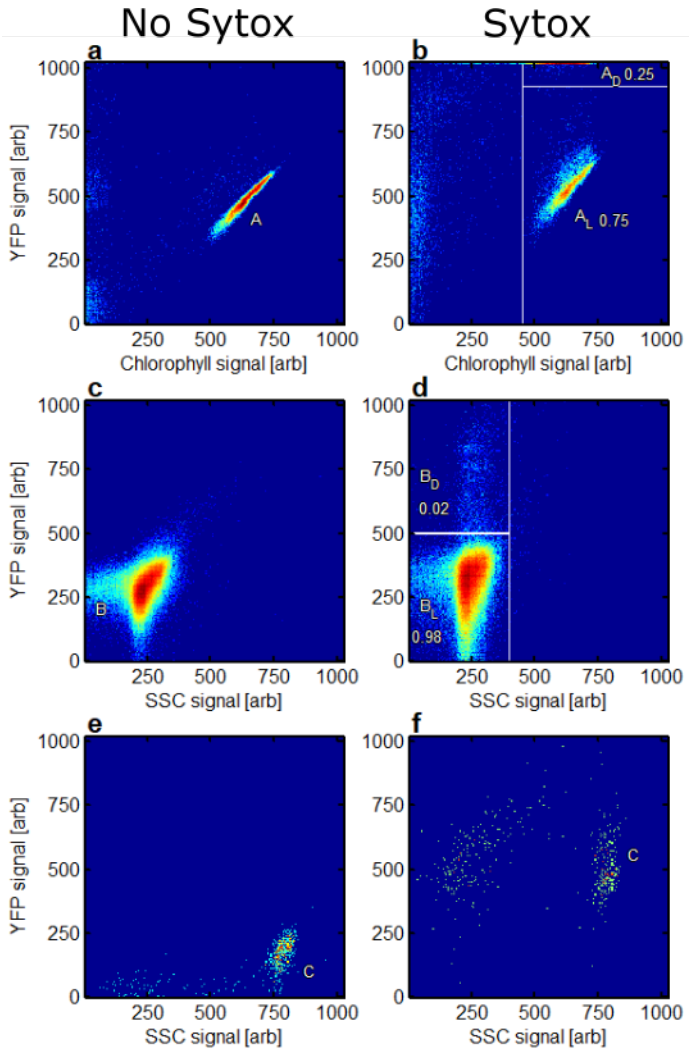

Figure 3.17: **Live-dead staining of algae and bacteria a,** YFP signal plotted versus Chlorophyll signal for flow cytometry data taken from day 4 of a 4200 Lux ABC coculture. The cloud labeled A is known to be algae **b,** YFP signal plotted versus Chlorophyll signal for that same sample but after the application of 100 nM Sytox. At sufficiently low concentration, Sytox selectively increases the YFP signal of dead cells. Note how a cloud with saturating YFP signal, thought to be dead algae A_D, has separated from the main cloud of live algae A_L. Numbers indicate fraction of counts within corresponding white rectangle divided by total counts across both white rectangles. **c,d** A similar analysis is performed on bacteria by plotting YFP signal versus SSC signal. In this case, the sample is taken from day 14 of a 4200 Lux B monoculture and in panel **d** 500 nM Sytox is used. **e,f** A similar analysis is performed on ciliates. In this case, the sample is taken from day 4 of a 1600 Lux C monoculture. Unstained cells are shown in **e** and cells stained with 100 nM Sytox in panel **f**. Note how the entire ciliate cloud shifts in YFP rather than separating out into high YFP and low YFP clouds, thus making quantification of dead cells impossible.

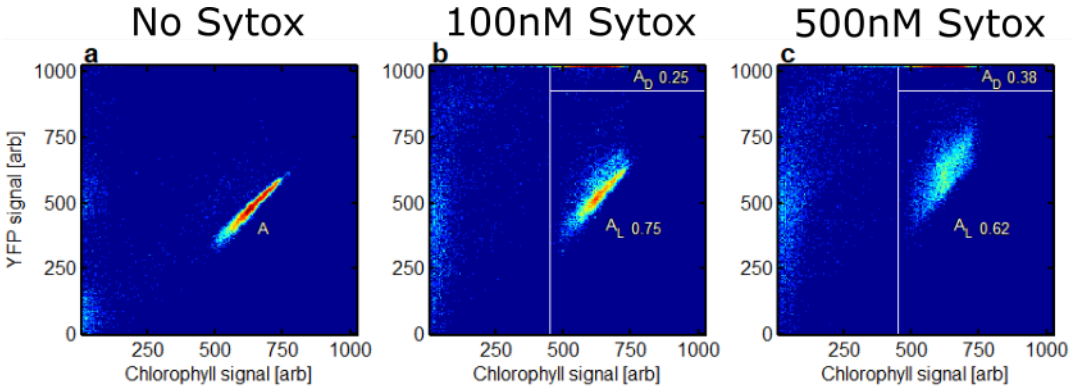

Figure 3.18: **Sytox staining overestimates fraction of algal cells that are dead a,** YFP signal plotted versus Chlorophyll signal for flow cytometry data taken from day 4 of a 4200 Lux ABC coculture. The cloud labeled"A" is known to be algae **b,** YFP signal plotted versus Chlorophyll signal for that same sample but after the application of 100 nM Sytox. Note how a cloud with saturating YFP signal comprised of dead algae A_D, has separated from the main cloud of live algae A_L. Numbers indicate fraction of counts within corresponding white rectangle divided by total counts across both white rectangles. **c,** Same sample and analysis as panel **b** except in this case 500 nM Sytox has been used. Note how the additional Sytox significantly changes the ratio between live and dead cells.

3.7 Successful bacterial invasions are not an artifact of mis-classifing algae detritus as bacteria

Given that detritus accumulates over the course of experiments, we looked closer at flow cytometry data to confirm that accumulating algae detritus was not being mislabeled as a successfully invading bacterial population, especially in the case of the stalled bacterial invasion. First we plotted YFP signal versus SSC signal for time points at the beginning, middle, and end of a 1600 Lux (low light) algae monoculture (Fig. 3.19a-d). We then examined the number of objects that pass a gate for bacteria as a function of time. Over the course of this algae monoculture, only a small number of objects (<100) passed this gate. The same was true for a 4200 Lux (high light) algae monoculture (Fig. 3.19e-h). In contrast, there were approximately a thousand times as many objects in this gate at the end of a 1600 Lux B invasion on A (Fig. 3.19i-l) and a 4200 Lux B invasion on A (Fig. 3.19m-p). These results suggest that algal detritus is not a strong contributor to the number of counts of B we observe by flow cytometry.

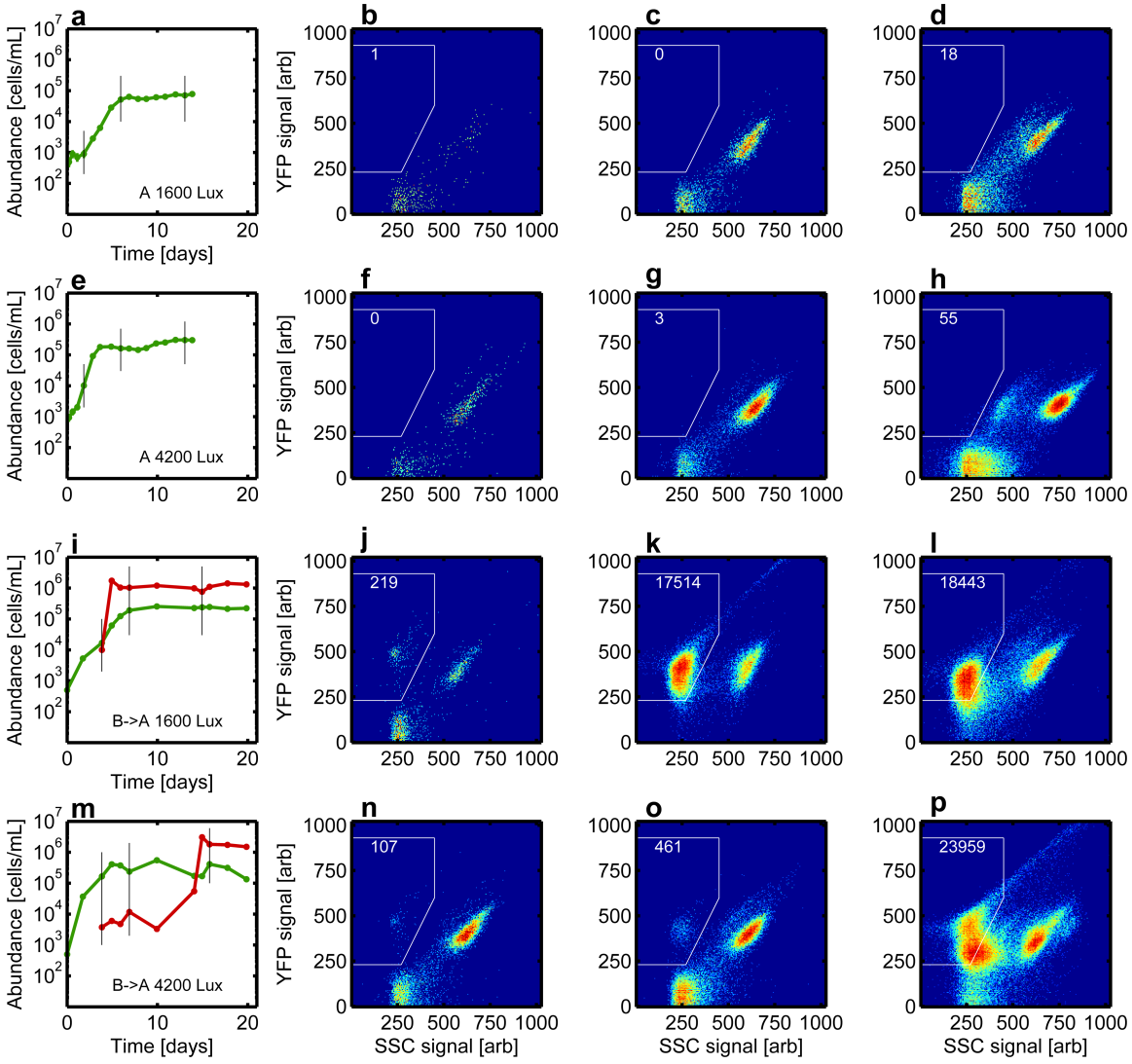

Figure 3.19: **Accumulating algae detritus is not being misclassified as bacteria a,** Abundance dynamics for a 1600 Lux (low light) algae monoculture. The three black lines mark the three time points for which flow cytometry data is plotted in **b,c,&d**. **b,** Heatmap for flow cytometry data taken from first marked time point with YFP signal plotted versus SSC signal. Number represents number of counts inside white polygon which is the gate used to detect bacteria. **c,** Same plot for second time point. **d,** Same plot for third time point. Subsequent rows in this figure depict the same analysis, but for a 4200 Lux (high light) algae monoculture, a 1600 Lux B invasion on A, and a 4200 Lux B invasion on A. In all panels with flow cytometry data, the same gate is used.

3.8 Details of model of ABC dynamics with higher order interactions

We present a simple, deterministic, ODE based model of population dynamics in the ABC community that reproduces the core features of our data. These features are as follows:

- Bacteria successfully invade AC communities with low algal densities
- Bacteria fail to invade AC communities when A is at high density
- Bacteria invade A and C monocultures with slower invasions of A monocultures at high A densities
- C induces B aggregation
- A inhibits B aggregation
- There is no competition for nutrients in the system that is responsible for these observations

In order to capture these features with a minimum of freely varying parameters, we constructed the following model in which most parameters can be estimated directly from data.

$$\dot{x}_B = x_B(r_B - r_{AB}\frac{x_A}{K_A})S - Fx_Bx_C - \alpha_1 x_B x_C + \alpha_2 A_B x_A \tag{3.1}$$

$$\dot{A}_B = \alpha_1 x_B x_C - \alpha_2 A_B x_A \tag{3.2}$$

$$\dot{x}_A = r_A x_A(1 - \frac{x_A}{K_A}) \tag{3.3}$$

$$\dot{x}_C = r_C x_C(1 - \frac{x_C}{K_C}) \tag{3.4}$$

$$\dot{S} = -\frac{x_B}{Y}(r_B - r_{AB}\frac{x_A}{K_A})S \tag{3.5}$$

$$\tag{3.6}$$

x_B is the density of planktonic (single-celled) bacteria, while A_B is the density of bacteria in aggregates. x_A and x_C are the density of algae and ciliates respectively.

Note that the substrate which drives bacterial growth S is assumed unitless without loss of generality with an initial value of 1. Y then is the carrying capacity of bacteria in the medium used here ($3.9 \times 10^6\,\mathrm{mL}^{-1}$). Only planktonic bacterial cells (x_B) can grow on the substrate S. We assume that aggregated bacterial cells (A_B) do not grow since *E. coli* biofilms are known to exhibit a physiological state similar to stationary phase [100]. Note that the model makes no claim on how many aggregates there are, nor how many bacteria make up a given aggregate; A_B simply denotes how many cells of bacteria are in an aggregated state. We then obtain the total number of bacterial cells $T_B = x_B + A_B$. T_B is what is plotted for bacterial abundances in all figures in the main text and is the output of our aggregate correction algorithm discussed above. Below we justify the functional forms used in this model and the parameter values we chose for numerical simulation.

The parameters of the model are described in the following table with their corresponding values. We are able to directly measure or use previous work to constrain all parameters except r_{AB}, α_1 and α_2. r_{AB} must be on the same order as r_B in order to observe substantial inhibition of B growth by A so we set this parameter accordingly. α_1 is inferred indirectly from the data. We treat α_2 as the only free parameter in the model and study our model behavior over a range of values (see below).

Values for all parameters in our simulation are given in Table 3.1.

Table 3.1: Model parameter values

Parameter	Value	Source
r_B	$0.3\,\mathrm{h}^{-1}$	This study
r_{AB}	$0.29\,\mathrm{h}^{-1}$	Inferred
r_C	$0.073\,\mathrm{h}^{-1}$	This study
r_A (high light)	$0.073\,\mathrm{h}^{-1}$	Fig. 3.1
r_A (low light, w/BC)	$0.016\,\mathrm{h}^{-1}$	Fig. 3.1
r_A (low light, w/C)	$0.025\,\mathrm{h}^{-1}$	Fig. 3.1
r_A (low light, w/B)	$0.031\,\mathrm{h}^{-1}$	Fig. 3.1
r_A (low light, alone)	$0.045\,\mathrm{h}^{-1}$	Fig. 3.1
K_A	$2.3 \times 10^5\mathrm{mL}^{-1}$	This study
K_C	$1.2 \times 10^4\mathrm{mL}^{-1}$	This study
Y	$3.9 \times 10^6\mathrm{mL}^{-1}$	This study
F	1×10^{-5} mL h^{-1}	[65] [101] [102], Inferred
α_1	2.5×10^{-6} mL h^{-1}	This study
α_2	2×10^{-8} mL h^{-1}	Free parameter

3.8.1 Bacteria-ciliate interactions

To begin, we ignore the algae and examine the interaction between the bacteria and the ciliates. This interaction is characterized by five parameters: r_B, Y, α_1, F, r_C and K_C. Of these parameters, r_B, Y, r_C, K_C and F can be inferred from data acquired for this study. For a more detailed discussion of the estimate of F, the feeding rate, from our data, see below. This leaves α_1, the rate at which the ciliates induce B aggregation, unknown. We therefore performed simulations on a co-culture of B and C while varying the parameter α_1 in order to see which value of α_1 best reproduces the data. The results of these simulation are shown in Fig. 3.20. The simulations show an intuitive result. In all cases, the bacteria (T_B) grow to a high density before the ciliates (x_C) have grown to an appreciable density. The aggregation rate α_1 then determines how much the bacterial density crashes after that peak. If the aggregation rate α_1 is low, the bacteria fail to aggregate sufficiently quickly to avoid predation and the total bacterial density T_B crashes severely. Conversely, if α_1 is set high, bacteria aggregate quickly and avoid predation and experience only a very mild fall after the abundance peak. Typically in data when B is grown in coculture with C, we observe bacterial densities peaking to just above $1 \times 10^6\,\mathrm{mL}^{-1}$ before dropping to about $1 \times 10^5\,\mathrm{mL}^{-1}$ (Fig. 3.8c). Matching simulations to these values is one criteria for choosing α_1. The other criteria is as follows. In BC co-culture experiments we observe a transient spike (i.e. the peak followed by crash) in bacterial density while in invasion experiments of B on C the bacterial density does not exhibit a spike (e.g. Fig. 2 , main text). The absence of the spike in bacterial abundances in invasion experiments is likely due to increased initial bacterial aggregation in invasion experiments which is itself driven by the fact that the ciliates are at higher density in invasion experiments at the time of bacterial introduction. Taking both criteria into account, we want the aggregation rate α_1 to be low enough that bacterial density drops to 1×10^5 mL^{-1} in BC co-culture simulations, but high enough that the bacteria do not exhibit a spike in B-invasion-of-C simulations (Fig. 3.20 bottom right panel). We take $\alpha_1 = 2.5 \times 10^{-6}$ mL h^{-1} as the best compromise between these two criteria and fix this parameter at that value for all future simulations.

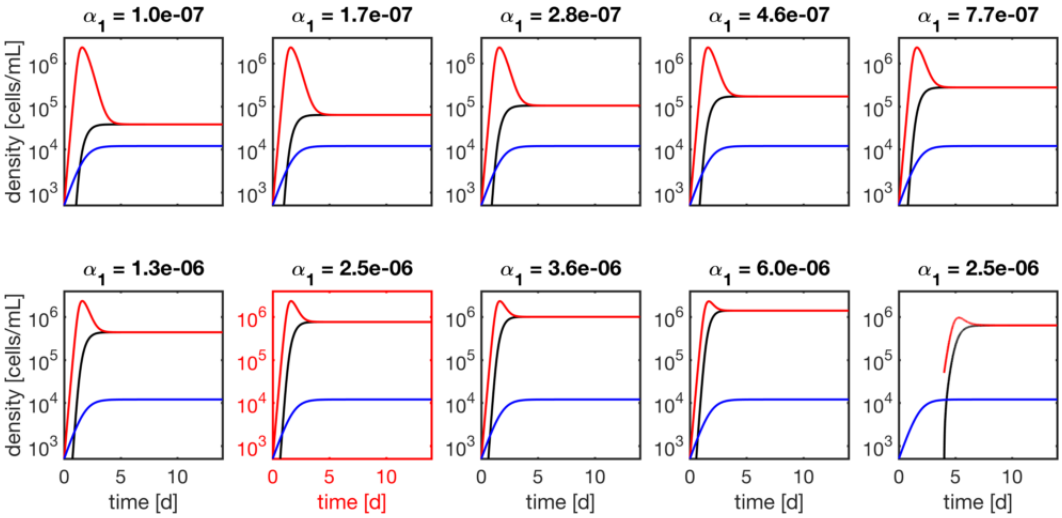

Figure 3.20: Abundance dynamics of B and C in co-culture simulated using the model discussed above. Parameter values are as shown in Table 3.1 with the exception of α_1 which is varied as indicated in the title of each panel (units are mL h^{-1}). In each panel, the total bacteria T_B is in red, the ciliates x_C in blue, and aggregating bacteria A_B in black. The bottom right panel shows abundance dynamics of B and C in invasion rather than co-culture. The red line and black line overlap at long times ($T_B = A_B$) because the ciliates eventually induce all bacteria to aggregate.

3.8.2 Predation rates and functional form

Here we justify three modeling assumptions regarding the predator-prey interaction between C and B: (1) the functional response (B loss term) is linear in bacterial densities, (2) the numerical response (growth of C due to predation on B) is negligible, (3) the feeding rate is estimated to be 1×10^{-5} mL h^{-1}.

First, there is substantial evidence that the functional response of *T. thermophila* consuming bacterial prey is sigmoidal (e.g. $f_{max} x_B x_C/(U + x_B)$ where f_{max} and U are constants). The typical justification for this is the presence of a prey handling time which limits the absolute rate at which a predator can consume a prey [103]. Measurements of C feeding rates as a function of bacterial density show clear saturation at higher bacterial densities [104]. The sigmoidal dependence of ciliate uptake rates on prey concentration is further supported by studies of ciliate uptake of latex microspheres [67]. These studies give a half-velocity constant (U) for the sigmoidal prey uptake rate in the case of *T. thermophila* of 10^7 bacteria mL^{-1}. Further studies show limited growth of *T. vorax* for *E. coli* densities below 2×10^7 mL^{-1} [105]. Therefore, the literature supports the conclusion that in our experiment, where bacterial densities never rise above 4×10^6 mL^{-1}, the functional response is well approximated by

a linear model ($x_B << U$). We therefore use the term Fx_Bx_C to describe the impact of C on the (planktonic) bacterial densities. In this linear model, following previous convention [67] we refer to the feeding rate as the per ciliate uptake rate of bacteria at low bacterial densities e.g. $F = f_{max}/U$.

Second, we claim that the feeding rate of ciliates on bacteria (F) has a value of 1×10^{-5} mL h^{-1}. This claim is supported again by the literature. Fenchel estimated a feeding rate of *Tetrahymena* of approximately 10^{-5} mL h^{-1} [65]. Hatzis *et al.* measured uptake rates in *Tetrahymena* of fluorescently labeled 2.74 µm diameter latex beads (at low bead concentration) and found rates between 10^{-5} to 10^{-4} mL h^{-1} while noting substantial population level heterogeneity in bead uptake [101]. We note that studies with passive particles (latex spheres) avoid possible artifacts from prey aggregation. In a follow-up study the same authors note that the fraction of feeding ciliates declines substantially from about 80 % to 20 % as the ciliates enter stationary phase [102]. This is likely a contributor to the dynamics we observe in our study. However, we neglect this time dependent feeding rate in order to keep the model simple. Finally, we can make crude estimates of this rate from our data as well. If we neglect aggregation and algae, the dynamics of bacteria are given by $\dot{x}_B/x_B = (r_B - Fx_C)$. We measure r_B =0.3 h^{-1}. We note that the growing bacteria are limited in their maximum density due to predation, at the crossover point (when predation and growth are balanced) $r_B = Fx_C$, or $F = r_B/x_C$. If we assume that this crossover point occurs when $x_C \sim 1 \times 10^4$ mL^{-1} (and before bacteria have consumed all substrate) this gives an estimate of $F \approx 3 \times 10^{-5}$ mL h^{-1}, in good agreement with previous estimates. Due to the dependence of C feeding rates on growth state of the population and particle sizes, both of which are changing in our experiment as C enters stationary phase and B aggregates, we fixed the feeding rate on the lower end of the reported range: 10^{-5} mL h^{-1}. Note that this feeding rate only applies to planktonic bacteria, x_B. In order to replicate the inability of ciliates to eat aggregates of bacteria, there is no feeding of ciliates on aggregating bacteria A_B in the model.

Third, we claim that the numerical response of the predator in response to predation is negligible and we therefore make C abundance dynamics independent of x_B (Eqn. 3.4). The results of Seta and Tazaki [105] show no growth of *T. vorax* on *E. coli* when the abundance of the latter is below 2×10^7 mL^{-1}. In fact, these

authors estimate a ciliate yield of 4×10^4 bacteria/ciliate (e.g. one ciliate is produced from the consumption of 4×10^4 bacterial cells). Further, Curds and Cockburn [104] measure the dry weight of *T. pyriformis* (1.3×10^{-10} g cell^{-1} and the yield on bacteria (*Klebsiella aerogenes*) to be 50 % by dry weight. If we take the dry weight of *E. coli* to be 280 fg (`bionumbers.hms.harvard.edu`BNID: 103904) we estimate approximately 1×10^3 bacteria/ciliate. Therefore, we expect the yield of C on B to be between 1×10^3 to 4×10^4 bacteria/ciliate. Our data show that C predation reduces bacterial abundances from approximately 1×10^6 to 1×10^5 mL^{-1} (Fig. 3.8c). Based on this reduction in B density, and the range of yields, we expect predation to produce between 50 and 1000 ciliates. Given the carrying capacity of C on this medium is 1.2×10^4 mL^{-1} we conclude that the numerical response generates at most 10 % of the maximum C population. Finally, when we compare abundance dynamics of C in the presence and absence of B we see no significant difference (Fig. 3.21). These results support the modeling decision to omit any numerical response from our description of the community dynamics.

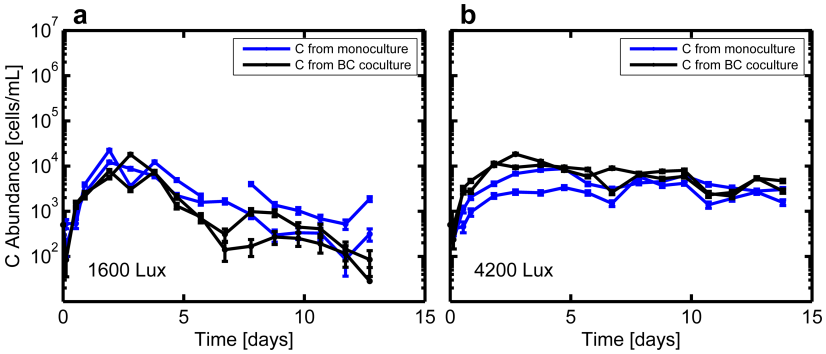

Figure 3.21: Abundance dynamics of C in monoculture and in co-culture with B at 1600 Lux (**a**) and 4200 Lux (**b**).

3.8.3 Algae-bacteria interactions

Modeling AB interactions and dynamics requires three assumptions: (1) A growth rate depends only on light level and composition of the community, (2) A inhibits growth of B but not carrying capacity and (3) the de-aggregation rate of B due to the presence of A takes a value of $\alpha_2 = 2 \times 10^{-8}$ mL h^{-1}.

First, Fig. 3.1 shows measured growth rates of A as a function of light level and community composition. At low light algal growth rate decreases substantially with

the addition of B and/or C. At high light, to within the precision of our measurement, A growth rate does not depend on community composition. Rather than construct a functional form with its own parameters that relates algal growth rate to light and community composition, we simply set the algal growth rate for each combination of light level and community composition. Since the dynamics of B are the focus of our study, and A dynamics are always well described by a logistic model, this modeling choice is well justified and removes unnecessary parameters from our model.

Second, as shown in Eqn. 3.1, we assume that A impacts the growth rate of B in a density dependent fashion ($r_B S - r_{AB} x_A / K_A$), but also that A has no impact on the carrying capacity of B. Our data support this assumption since we see no impact of the presence of A on the carrying capacity of B. In the situation where B invades a high density ($>1 \times 10^5$ mL^{-1}) algae culture, we find that the bacterial growth is strongly inhibited in about half of the cases we observed. We therefore capture this growth inhibition using the term shown above. We note that this purely deterministic model will not capture the stochastic outcomes we observe experimentally (that would require a more detailed model of the A inhibition of B and likely the predation process). We set r_{AB} to be on the same order as r_B. We make this assumption since our data clearly show that A is capable of nearly completely, or completely, inhibiting the growth of B (e.g. when $x_A = K_A$ near-complete inhibition will occur if $r_{AB} \approx r_B$).

Third, we must specify the unknown parameter α_2. To do so, we treat it as a free parameter in our simulation since we have no direct measure of the rate at which A induces B to de-aggregate. We performed three simulations of the full three species (ABC) community: AC, high light $t_{inv} = 4$ d; ABC high light, co-culture; AC low-light,$t_{inv} = 4$ d. For each condition we swept α_2 over a range of logarithmically spaced values. Our expectation is that for a single value of α_2 we should find that B fails to invade in AC high light at 4 d, successfully grows in co-culture with AC, and successfully invades AC low light at 4 d. The results of these three simulations are shown in Figs. 3.22,3.23,3.24. From these simulations we find that $\alpha_2 = 2 \times 10^{-8}$ mL h^{-1} captures the experimentally observed dynamics in all three conditions (see panels with red axes in Figs. 3.22,3.23,3.24).

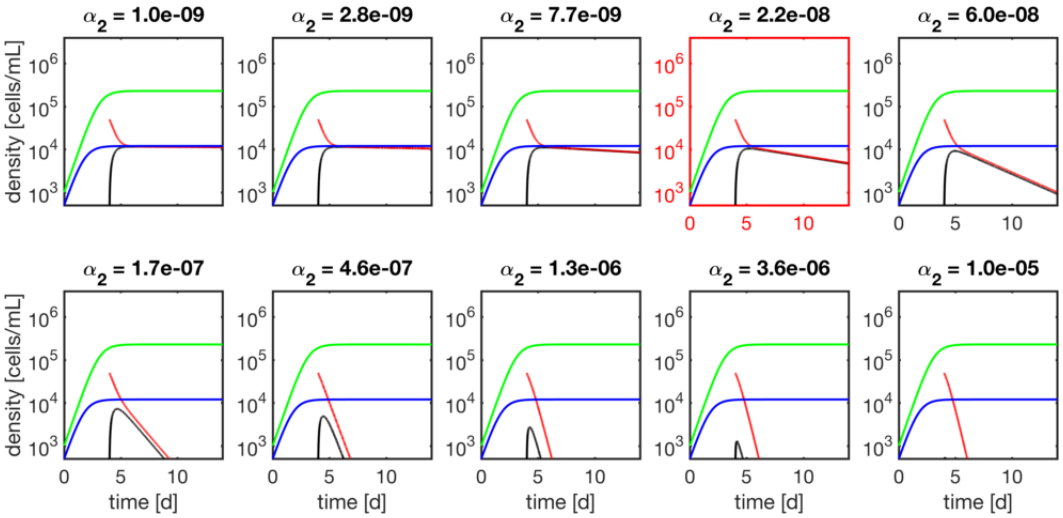

Figure 3.22: Abundance dynamics of A, B and C in high light conditions with $t_{inv} = 4\,\mathrm{d}$. Parameter values are as shown in Table 3.1 with the exception of α_2 which is varied as indicated in the title of each panel. In each panel x_A is in green, x_C in blue, T_B in red, and A_B in black. The units of α_2 are mL h^{-1}.

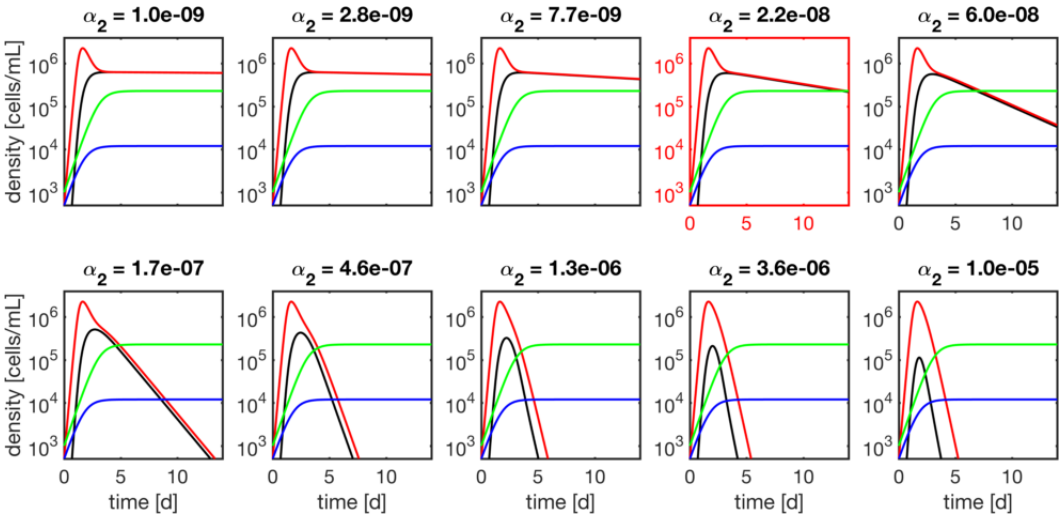

Figure 3.23: Abundance dynamics of A, B and C in high-light, co-culture conditions simulated using the model discussed above. Parameter values are as shown in Table 3.1 with the exception of α_2 which is varied as indicated in the title of each panel. In each panel x_A is in green, x_C in blue, T_B in red, and A_B in black. The units of α_2 are mL h^{-1}

3.8.4 Aspects of the dynamics not captured by the model

The model presented here is necessarily simplified to limit the number of free parameters in the simulation to one (α_2). As a result there are several qualitative aspects of the data that are not captured by the modeling framework. Here we enumerate these.

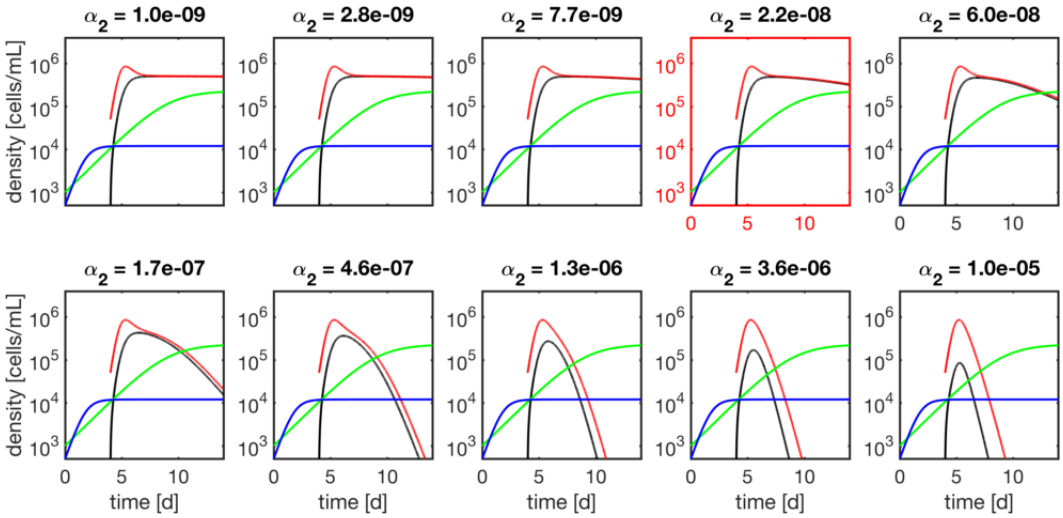

Figure 3.24: Abundance dynamics of A, B and C in low light conditions for $t_{inv} = 4\,\mathrm{d}$ simulated using the model discussed above. Parameter values are as shown in Table 3.1 with the exception of α_2 which is varied as indicated in the title of each panel. The growth rate for A in this simulation is taken to be the low light growth rate in the presence of C alone (r_A =0.025 h^{-1}). In each panel x_A is in green, x_C in blue, T_B in red, and A_B in black. The units of α_2 are mL h^{-1}

- B exhibits a transient spike in aggregation as it enters stationary phase even in the absence of A or C. (e.g. Fig. 3.3g). This process has been examined previously in our group and explained using a substrate dependent aggregation process. [73] We neglect this aspect of the bacterial aggregation dynamics.

- In co-culture conditions with B in the presence of C, after the peak in bacterial abundance and then subsequent fall due to predation, the abundances of B rise over the last ∼10 days of the experiment. (Fig. 6 h, main text). This rise could be explained by slow growth of aggregated bacteria or by growth of B on the detritus of dying C. Our model fails to capture the rise and we have not included it since we have no direct evidence for either of these processes.

- The deterministic ODE framework does not capture the stochasticity we observe in the outcome of B invading A alone (Fig. 3.9). This stochasticity could be captured by an effective randomness in the parameter r_{AB}. We have not included it here since the process is likely driven by population structure in either A or B which is not present in the current model (e.g. phenotypic heterogeneity in the response of B to inhibition by A). In the absence of direct mechanistic insight into this stochasticity process, we omitted it from our model.

- The decline in C abundances after approximately 4 days is not modeled here. This decline could be addressed by inferring a death rate from the data, but it would not qualitatively impact the agreement between the model and the simulation.

Chapter 4

Environment determines evolutionary trajectory in a constrained phenotypic space

Constraints on phenotypic variation limit the capacity of organisms to adapt to the multiple selection pressures encountered in natural environments. To better understand evolutionary dynamics in this context, we select *Escherichia coli* for faster migration through a porous environment, a process which depends on both motility and growth. We find that a trade-off between swimming speed and growth rate constrains the evolution of faster migration. I was responsible for developing the apparatus for measuring swimming speed. Evolving faster migration in rich medium results in slow growth and fast swimming, while evolution in minimal medium results in fast growth and slow swimming. This result demonstrates how, when a trade-off between two phenotypes exists, the environment can determine the evolutionary trajectory.

4.1 Introduction

In nature organisms adapt to complex environments where many biotic and abiotic factors affect survival. For microbes these factors include demands on metabolism [106], motility [107] and antibiotic resistance [52]. In this context, evolution involves the simultaneous adaptation of many phenotypic traits. Organisms under complex selection pressures often cannot vary traits independently and instead exhibit trade-offs [108].

Trade-offs constrain adaptive responses to selection. For example, phage exhibit a trade-off between fecundity and virulence which depends on the relative duration of periods of horizontal and vertical transmission [109]. Bacterial populations selected for efficient conversion of nutrients to biomass exhibit a trade-off between yield and growth rate [110].

Predicting evolution in complex environments requires quantifying both trade-offs and selection pressures [111]. In wild populations of birds [112] and fish [113], phenotypic constraints and selection pressures have been inferred from measurements of phenotypic variation. However, in wild populations of higher organisms it is challenging to observe evolution, determine selection pressures and elucidate mechanisms constraining phenotypes. To better understand the interplay between trade-offs, selection and evolution, it is necessary to study genetically tractable, rapidly evolving microbial populations in the laboratory.

However, laboratory-based experimental evolution of microbes typically selects for a single phenotype such as growth rate [114]. There is evidence that metabolic trade-offs arise in these experiments from the decay of traits that are not subject to selection [115] rather than a compromise between multiple selection pressures. Other experiments explore how phenotypes restricted by trade-offs evolve under alternating selection for individual traits [109, 116]. Less is known about evolutionary dynamics in the naturally relevant regime where selection pressures are multifaceted.

To address this, we selected *Escherichia coli* for faster migration through a porous environment. We showed that the evolution of faster migration is constrained by a trade-off between swimming speed and growth rate. Evolution of faster migration in rich medium is driven by faster swimming despite slower growth, while faster migration in minimal medium is achieved through faster growth despite slower swimming. Our results show that when selection acts simultaneously on two traits governed by a trade-off, the environment determines the evolutionary trajectory.

4.2 Results

4.2.1 Experimental evolution of migration rate

E. coli inoculated at the center of a low viscosity agar plate consume nutrients locally, creating a spatial nutrient gradient which drives chemotaxis through the porous agar matrix [117, 118] and subsequent nutrient consumption [119–121]. As a result, the outermost edge of the expanding colony is driven by both growth and motility [122]. The result is a three-dimensional bacterial colony that expands radially across the plate as individuals swim and divide in the porous environment. We refer to the

outermost edge of an expanding colony as the migrating front. We tracked these migrating fronts using webcams and light-emitting diode (LED) illumination. The front migrates at a constant speed S after an initial growth phase [119, 120].

We performed experimental evolution by repeating rounds of allowing a colony to expand for a fixed time interval, selecting a small population of cells from the migrating front and using them to inoculate a fresh low viscosity agar plate (Fig. 4.1a). By isolating cells from the migrating front, our procedure selects both for motility and growth rate. We performed selection experiments in this way for two distinct nutrient conditions. First, we used rich medium (lysogeny broth (LB), 0.3 % w/v agar, 30 °C) where all amino acids are available. In this medium the population forms concentric rings (Fig. 1b) that consume amino acids sequentially. The outermost ring consumes L-serine and most of the oxygen [119]. Second, we used minimal medium (M63, 0.18 mM galactose, 0.3 % w/v agar, 30 °C) where populations migrate towards and metabolize galactose with a single migrating front.

In rich medium, colonies of wild-type bacteria (MG1655-motile, founding strain) expand with a front migration speed S of about 0.3 cmhr^{-1} and cells were sampled from the front after 12 hr (Fig. 4.1b). A portion of this sample was used to immediately inoculate a fresh plate while the remainder was preserved cryogenically. The process was repeated every 12 hr for 15 rounds. We observed a nearly 50% increase in S over the course of the first 5 rounds of selection. The increase in S was largely reproducible across five independent selection experiments (Fig. 4.1c).

We then performed selection experiments in a minimal medium where growth and migration are substantially slower than in rich medium (Fig. 4.1d). In this condition we allowed 48 hr for each round of expansion. In the first round, the population formed small, approximately 1.5 cm diameter colonies without a well defined front. Populations formed well defined fronts in subsequent rounds of selection (Fig. 4.1d), reflecting a transition from growth and diffusion dominated transport to chemotaxis dominated migration [121]. We observed an approximately 3-fold increase in S over the course of 10 rounds of selection.

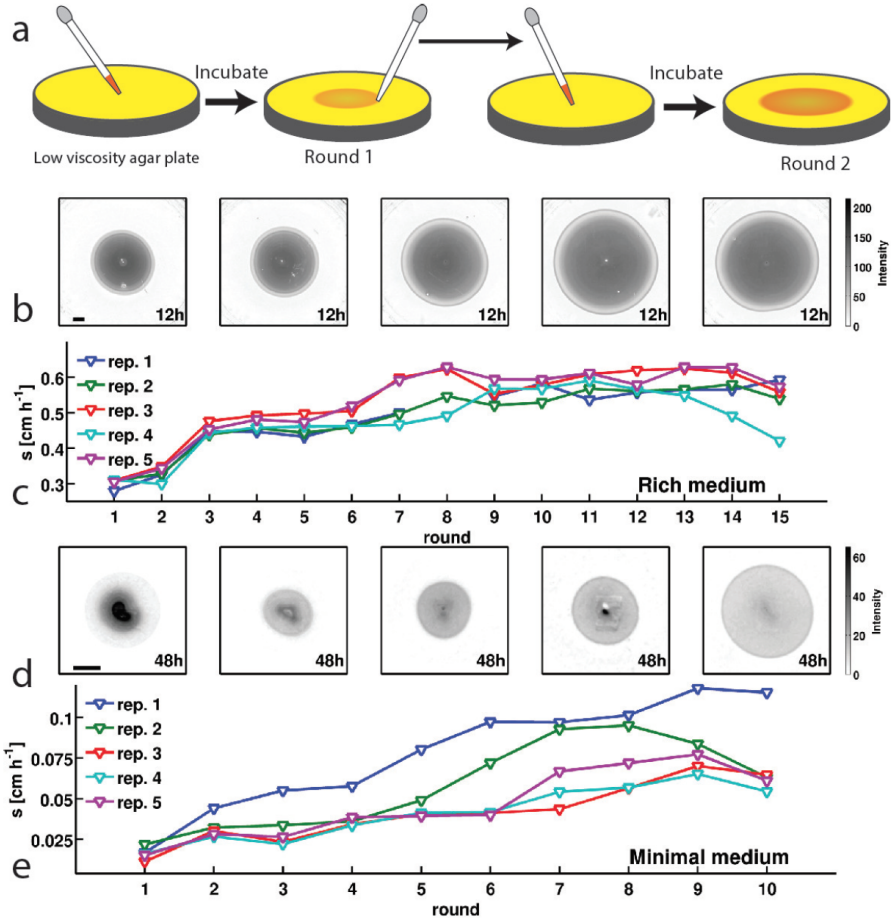

Figure 4.1: ***E. coli* evolves faster migration through a porous environment in rich and minimal media.** **a**, A schematic of the selection procedure. *E. coli* are inoculated into the center of a low viscosity (0.3 % w/v) agar plate where they form an expanding colony driven by metabolism and motility. After a fixed period of incubation, samples are taken from eight locations around the outer edge of the expanded colony, mixed, and used to inoculate a fresh plate. **b**, Shows expanded colonies in rich medium (LB) plates after 12 hr of incubation over five successive rounds of selection. The color bar to the right applies to all panels in (**b**), with darker gray indicating higher cell density. Image intensity is assumed to be monotonic but not linear with cell density in the plate. Scale bar in the left panel is 1 cm and applies to all panels in (**b**). **c**, Shows the rate of migration as a function of round of selection over 15 rounds for five replicate selection experiments in rich medium. No rate is reported for replicate 1 round 8 due to failure of the imaging device. Errors in measured rates of migration are smaller than the size of the markers. **d**, Shows colonies (gray regions) in minimal medium (M63, 0.18 mM galactose) after 48 hr of incubation. The color bar to the right applies to all panels in (**d**). The scale bar in the left panel is 1 cm. **e**, Shows the rate of migration as a function of round of selection over 10 rounds for five replicate selection experiments in minimal medium. Errors in migration rates were smaller than the size of markers.

4.2.2 Increasing swimming speed and growth rate increase migration rate

To characterize the adaptation we observed in Fig. 4.1c,e, we studied a reaction-diffusion model of migrating bacterial fronts of the type pioneered by Keller and Segel [123] and reviewed in Tindall et al. [124]. A full description of the model and the predictions we made using it is available in our paper [125]. We found that increases in run speed ($|v_r|$) and growth rate (k_g) had the largest impact on S. Run speed increases the migration rate because strains that run faster can chemotax toward nutrients faster. Growth rate increases migration rate because strains that grow faster more rapidly establish the nutrient gradient necessary to perform chemotaxis. We therefore would predict that the selection for migration rate performed in this study would induce a strain to increase both its swimming speed and its growth rate.

4.2.3 A trade-off constrains the evolution of faster migration

To test the predictions of the reaction-diffusion model, we experimentally interrogated how the motility and growth phenotypes of our populations evolved over the course of selection. We performed single-cell tracking experiments using a microfluidic method similar to one described previously [126]. This method permitted us to acquire 5 min swimming trajectories from hundreds of individuals from strains isolated prior to selection (founder) and after 5, 10 and 15 rounds of selection in rich media (replicate 1, Fig. 4.1c) and for the founder and strains isolated after 5 and 10 rounds of selection in minimal media (replicate 1, Fig. 4.1e). For tracking, cells were grown in the medium in which they were selected. This technique permitted us to capture more than 280,000 run-tumble events from approximately 1500 individuals.

We identified run and tumble events for all individuals [127, 128]. Fig. 4.2ab shows that run durations declined over the course of selection in both rich and minimal media. We show the complementary cumulative distribution function ($c(\tau_r)$) of run durations (τ_r) aggregated across all run events detected for the founding or evolved strains. ($c(\tau_r)$) quantifies the fraction of all runs longer than a time τ_r. These distributions show that the evolved strains exhibited a reduction in the probability of executing long runs. We observed opposite trends for tumble duration, with de-

creasing tumble duration in rich medium and increasing duration in minimal medium (Figure 4.2). To summarize these changes in run-tumble statistics, we computed the tumble bias (fraction of time spent tumbling) and the tumble frequency (tumbles per second, Fig. 4.2cd). In both conditions, we observe an increase in the tumble frequency. This is expected since previous studies showed that mutants with increased tumble frequencies have faster migration rates through agar, likely due to tumbles freeing cells from being trapped in the agar [120]. In rich medium we observed a decline in tumble bias, while selection in minimal medium increased the tumble bias.

Fig. 4.2ef show the probability distributions of run speeds for founding and selected strains in both nutrient conditions. In rich medium we observed a nearly 50% increase in the run speed ($|v_r|$) between founder and rounds 10 to 15. Tracking strains isolated after 15 rounds from independent selection experiments (replicates 3 and 4, Fig. 4.1c) showed that this increase in run speed was reproducible across independent evolution experiments (Fig. 4.2).

Surprisingly, when we performed single-cell tracking for strains evolved in minimal media we observed the opposite trend. In these conditions we observed a 50% reduction in run speed (Fig. 4.2f). Again, we found that this result was reproducible across independently evolved strains (Fig. 4.2).

We then measured the growth rates of founding and evolved strains from both selection conditions in well mixed liquid corresponding to the medium used for selection. We observed a decline of about 10% in the maximum growth rate with selection in rich medium and a three-fold increase in the maximum growth rate after 10 rounds of selection in minimal medium (Fig. 4.2g-h). We found that these changes in growth rate are reproducible across independently evolved strains in both environmental conditions (Fig. 4.2).

We conclude that there is a trade-off between run speed and growth rate in *E. coli* which constrains the evolution of faster migration through low viscosity agar.

One additional result worth noting is that evolved strains were seen to be much less sticky than founder strains. Founder strains became stuck to the microfluidic device much more frequently and necessitated that the microfluidic be switched out more often. Being less sticky would likely make it easier to travel through the agar.

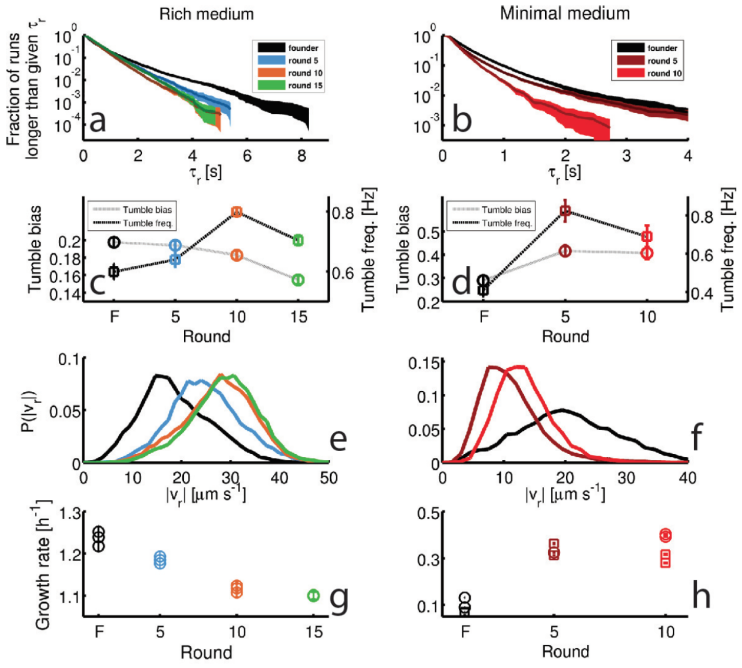

Figure 4.2: **Dynamics of phenotypic evolution in rich and minimal media. af,** Show single-cell swimming phenotypes (run duration (τ_r), run speed ($|v_r|$), tumble bias and tumble frequency). Tracking was performed for founding strain (140 cells, 19,597 run events), strains isolated after 5 (79 cells, 12,217 run events), 10 (97 cells, 18,505 run events) and 15 (96 cells, 15,928 run events) rounds in rich media and in minimal media for the founding strain (72 cells, 7556 run events), round 5 (45 cells, 9724 run events) and round 10 (25 cells, 4892 run events). **a,** Shows the fraction of runs longer than a given τ_r for strains evolved in rich media (95% confidence intervals from bootstrapping). The mean and standard deviation in run duration for founder is 0.66 ± 0.78 s, for round 5: 0.63 ± 0.61 s, for round 10: 0.58 ± 0.50 s and for round 15: 0.65 ± 0.57 s. Round 5, 10 and 15 strains exhibit shorter average run durations than founder ($p<0.05$). **b,** Shows the same distribution for strains in minimal medium with founder exhibiting average run duration 0.49 ± 0.52 s, round 5: 0.44 ± 0.48 s and round 10: 0.33 ± 0.28 s. Rounds 5 and 10 exhibit shorter average run durations than founder ($p<10^{-8}$). **cd** Show average fraction of time spent tumbling (tumble bias) and tumble frequency (tumbles per second) for rich medium and minimal medium respectively. Note the two vertical axes. In rich medium only the round 15 tumble bias is significantly different from founder ($p<0.001$), but the tumble frequency is higher than founder for both rounds 10 and 15 ($p<0.001$). In minimal medium all tumble biases and frequencies are significantly different from founder for all strains ($p<0.001$). **e,** Shows run speed distributions for strains evolved in rich medium, legend in (**a**) applies. The average ± standard deviation run speeds are, for founder: 18.7 ± 7.1 μm s^{-1}, round 5: 24.9 ± 7.1 μm s^{-1}, round 10: 27.6 ± 7.0 μm s^{-1}, and for round 15: 28.7 ± 6.8 μm s^{-1}. Average run speeds for rounds 5, 10 and 15 are greater than founder **f,** Shows the same distributions for strains evolved in minimal medium, average run speed for founder: 20.7 ± 10.8 μm s^{-1}, for round 5: 11.2 ± 4.8 μm s^{-1} and for round 10: 13.3 ± 4.4 μm s^{-1}. Both rounds 5 and 10 exhibit slower average run speeds than founder, the legend in (**b**) applies. **gh** Show growth rates in well mixed liquid culture for all strains studied in panels **af** in the medium in which the strains were selected. **g,** triplicate measurements from each of the four strains isolated in rich medium. Rounds 5, 10 and 15 exhibit slower growth than founder ($p<0.01$). **h,** growth rates for strains isolated from minimal medium selection experiment. Four replicate measurements were made for founder and round 10 and three replicate measurements for round 5. Squares and circles demarcate measurements made on separate days. Rounds 5 and 10 have higher growth rates than founder ($p<10^{-5}$).

4.3 Discussion

The most striking observation of our study is the divergent trajectories of phenotypic evolution. This observation shows that the evolution of faster migration results in environmentally dependent phenotypic outcomes. This result has important implications for interpreting phenotypic variation in natural populations.

Previous experimental evolution studies have revealed a similar trade-off to the one presented here. Comparing the results of these studies to our own demonstrates the impact of how selection is performed on the phenotypic outcomes. For example, Yi and Dean [116] selected *E. coli* alternately for growth in well mixed conditions and chemotaxis using a capillary assay and observed a trade-off between growth rate and swimming speed which was circumvented by phenotypic plasticity. We observe no evolution beyond the Pareto frontier in our study, possibly because our conditions simultaneously select for growth and motility rather than alternating between selection pressures. This suggests that evolutionarily persistent trade-offs may reflect selection pressures that occur simultaneously in nature. In addition, van Ditmarsch et al. [129] and Deforet et al. [130] select *Pseudomonas aeruginosa* for a hyperswarming phenotype on hard agar. Rather than sampling from the population at a specific location in a swarming colony, they allow the population to swarm for a fixed time interval, remove the entire colony from the plate and inoculate a second plate from a mixed sample of the entire colony. This procedure likely selects both for swarming speed and for growth in the bulk of the colony. Phenotypically, hyperswarmers selected in this way exhibit a decline in growth rate and swimming speed in liquid and a deficit in biofilm formation [129,130]. In light of our study, these results suggest that evolved phenotypes can depend on whether selection occurs at well defined spatial locations in a structured population (e.g. migrating fronts) or through periodic removal of spatial structure.

The mechanism of the trade-off between growth rate and swimming speed has, to our knowledge, not been determined. However, over-expression of motility operons could drive the reductions in growth rate we observe in rich medium. Subsequent increases in speed could then arise passively from reductions in cell size which reduce hydrodynamic drag [131]. Similarly, increases in growth rate in minimal medium should increase cell size and hydrodynamic drag. Using the data of Taheri-Araghi et

al. [131], we estimated changes in cell size due to mea- sured changes in growth rate for populations evolved in rich and minimal medium. We could not account for the large change in swimming speed we observe through growth rate mediated changes in cell size alone. Since we have not measured cell size directly, we cannot conclusively rule out this mechanism. To definitively characterize the mechanism of this trade-off will require measurements of cell size, gene expression, flagellar length and proton motive force.

Our study shows how evolutionary dynamics are defined by the complex interplay between genetic architecture, phenotypic constraints and the environment. Our hope is that a general approach to predicting evolution can emerge from a more complete understanding of this interplay.

Chapter 5

References

[1] Gerardo Ceballos, Paul R. Ehrlich, Anthony D. Barnosky, Andrs Garca, Robert M. Pringle, and Todd M. Palmer. Accelerated modern humaninduced species losses: Entering the sixth mass extinction. *Science Advances*, 1(5):e1400253, Jun 2015.

[2] M. Grooten and R.E.A Almond, editors. *Living Planet Report 2018. Aiming Higher.*, Gland, Switzerland, 2018. WWF.

[3] Millennium ecosystem assessment. In *Ecosystems and Human Well-being: Synthesis*, Washington, DC, 2005. Island Press.

[4] Walter C. Shortle and Kevin T. Smith. Wood decay fungi restore essential calcium to acidic soils in northern new england. *Forests*, 6(8):25712587, Aug 2015.

[5] *Mysterious mushroom mixture set to to boost reforestation of the Highlands*, 2018 (accessed April 16, 2019).

[6] Terry C. Hazen, Eric A. Dubinsky, Todd Z. DeSantis, Gary L. Andersen, Yvette M. Piceno, Navjeet Singh, Janet K. Jansson, Alexander Probst, Sharon E. Borglin, Julian L. Fortney, and et al. Deep-sea oil plume enriches indigenous oil-degrading bacteria. *Science*, 330(6001):204208, Oct 2010.

[7] Mayank Aggarwal. *How microbes can clean polluted water, from drains to rivers*, 2015 (accessed April 16, 2019).

[8] G. Glatzel, K. Haselwandter, K. Katzensteiner, H. Sterba, and J. Weibacher. The use of organic and mineral fertilizers in reforestation and in revitalization of declining protective forests in the alps. *Water, Air, and Soil Pollution*, 54(1):567576, Mar 1990.

[9] Cyrus Alexander Mallon, Jan Dirk van Elsas, and Joana Falco Salles. Microbial invasions: The process, patterns, and mechanisms. *Trends in Microbiology*, 23(11):719729, Nov 2015.

[10] William J. Ripple and Robert L. Beschta. Trophic cascades in yellowstone: The first 15 years after wolf reintroduction. *Biological Conservation*, 145(1):205213, Jan 2012.

[11] William J. Ripple, James A. Estes, Robert L. Beschta, Christopher C. Wilmers, Euan G. Ritchie, Mark Hebblewhite, Joel Berger, Bodil Elmhagen, Mike Letnic, Michael P. Nelson, and et al. Status and ecological effects of the worlds largest carnivores. *Science*, 343(6167):1241484, Jan 2014.

[12] Mehdi Layeghifard, David M. Hwang, and David S. Guttman. Disentangling interactions in the microbiome: A network perspective. *Trends in Microbiology*, 25(3):217228, Mar 2017.

[13] J. Michael Janda and Sharon L. Abbott. 16s rrna gene sequencing for bacterial identification in the diagnostic laboratory: Pluses, perils, and pitfalls. *Journal of Clinical Microbiology*, 45(9):27612764, Sep 2007.

[14] Richard R. Stein, Vanni Bucci, Nora C. Toussaint, Charlie G. Buffie, Gunnar Rtsch, Eric G. Pamer, Chris Sander, and Joo B. Xavier. Ecological modeling from time-series inference: Insight into dynamics and stability of intestinal microbiota. *PLOS Computational Biology*, 9(12):e1003388, Dec 2013.

[15] Shinichi Sunagawa, Luis Pedro Coelho, Samuel Chaffron, Jens Roat Kultima, Karine Labadie, Guillem Salazar, Bardya Djahanschiri, Georg Zeller, Daniel R. Mende, Adriana Alberti, and et al. Structure and function of the global ocean microbiome. *Science*, 348(6237):1261359, May 2015.

[16] Edi Prifti and Jean-Daniel Zucker. *The New Science of Metagenomics and the Challenges of Its Use in Both Developed and Developing Countries*, page 191216. Springer Singapore, 2015.

[17] Stilianos Louca, Laura Wegener Parfrey, and Michael Doebeli. Decoupling function and taxonomy in the global ocean microbiome. *Science*, 353(6305):12721277, Sep 2016.

[18] Catherine Burke, Peter Steinberg, Doug Rusch, Staffan Kjelleberg, and Torsten Thomas. Bacterial community assembly based on functional genes rather than species. *Proceedings of the National Academy of Sciences*, 108(34):1428814293, Aug 2011.

[19] Stilianos Louca, Martin F. Polz, Florent Mazel, Michaeline B. N. Albright, Julie A. Huber, Mary I. OConnor, Martin Ackermann, Aria S. Hahn, Diane S. Srivastava, Sean A. Crowe, and et al. Function and functional redundancy in microbial systems. *Nature Ecology & Evolution*, 2(6):936943, 2018.

[20] Lutz Becks, Stephen P. Ellner, Laura E. Jones, and Nelson G. Hairston. Reduction of adaptive genetic diversity radically alters eco-evolutionary community dynamics. *Ecology Letters*, 13(8):989997, Aug 2010.

[21] Kevin Dhoe, Stefan Vet, Karoline Faust, Frdric Moens, Gwen Falony, Didier Gonze, Vernica Llorns-Rico, Lendert Gelens, Jan Danckaert, Luc De Vuyst, and et al. Integrated culturing, modeling and transcriptomics uncovers complex interactions and emergent behavior in a three-species synthetic gut community. *eLife*, 7:e37090, Oct 2018.

[22] Robert M. May. *Stability and complexity in model ecosystems*. Monographs in population biology. Princeton University Press, 1973.

[23] Eric L. Berlow, Anje-Margiet Neutel, Joel E. Cohen, Peter C. De Ruiter, Bo Ebenman, Mark Emmerson, Jeremy W. Fox, Vincent A. A. Jansen, J. Iwan Jones, Giorgos D. Kokkoris, and et al. Interaction strengths in food webs: issues and opportunities. *Journal of Animal Ecology*, 73(3):585598, 2004.

[24] John H. Vandermeer. The competitive structure of communities: An experimental approach with protozoa. *Ecology*, 50(3):362371, May 1969.

[25] L. V. Nedorezov. The dynamics of the lynxhare system: an application of the lotkavolterra model. *Biophysics*, 61(1):149154, Jan 2016.

[26] Roger Arditi and Lev R. Ginzburg. Coupling in predator-prey dynamics: Ratio-dependence. *Journal of Theoretical Biology*, 139(3):311326, Aug 1989.

[27] Ludek Berec, Elena Angulo, and Franck Courchamp. Multiple allee effects and population management. *Trends in Ecology & Evolution*, 22(4):185191, Apr 2007.

[28] Babak Momeni, Li Xie, and Wenying Shou. Lotka-volterra pairwise modeling fails to capture diverse pairwise microbial interactions. *eLife*, 6:e25051, Mar 2017.

[29] Peter A. Abrams. Arguments in favor of higher order interactions. *The American Naturalist*, 121(6):887891, Jun 1983.

[30] J. Timothy Wootton. Indirect effects and habitat use in an intertidal community: Interaction chains and interaction modifications. *The American Naturalist*, 141(1):7189, 1993.

[31] Wade B. Worthen and Jennifer L. Moore. Higher-order interactions and indirect effects: A resolution using laboratory drosophila communities. *The American Naturalist*, 138(5):10921104, Nov 1991.

[32] Margaret M. Mayfield and Daniel B. Stouffer. Higher-order interactions capture unexplained complexity in diverse communities. *Nature Ecology & Evolution*, 1(3):62, Feb 2017.

[33] T.J. Case and E.A. Bender. Testing for higher order interactions. *American Naturalistl*, 118:920–929, 1981.

[34] Alicia Sanchez-Gorostiaga, Djordje Baji, Melisa L. Osborne, Juan F. Poyatos, and Alvaro Sanchez. High-order interactions dominate the functional landscape of microbial consortia. *bioRxiv*, 2018.

[35] Eyal Bairey, Eric D. Kelsic, and Roy Kishony. High-order species interactions shape ecosystem diversity. *Nature Communications*, 7:12285, Aug 2016.

[36] Jacopo Grilli, Gyrgy Barabs, Matthew J. Michalska-Smith, and Stefano Allesina. Higher-order interactions stabilize dynamics in competitive network models. *Nature*, 548(7666):210213, Aug 2017.

[37] Peter M Letcher, Salvador Lopez, Robert Schmieder, Philip A Lee, Craig Behnke, Martha J Powell, and Robert C McBride. Characterization of Amoeboaphelidium protococcarum, an Algal Parasite New to the Cryptomycota Isolated from an Outdoor Algal Pond Used for the Production of Biofuel. *PloS ONE*, 8(2):e56232–15, February 2013.

[38] Aurelie Chambouvet, Pascal Morin, Dominique Marie, and Laure Guillou. Control of toxic marine dinoflagellate blooms by serial parasitic killers. *Science*, 322(5905):1254–1257, November 2008.

[39] L.G.M. Baas Becking. *Geobiologie of inleiding tot de milieukunde*. Den Haag: W.P. Van Stockum & Zoon, 1934.

[40] Shinichi Sunagawa, Luis Pedro Coelho, Samuel Chaffron, Jens Roat Kultima, Karine Labadie, Guillem Salazar, Bardya Djahanschiri, Georg Zeller, Daniel R Mende, Adriana Alberti, Francisco M Cornejo-Castillo, Paul I Costea, Corinne Cruaud, Francesco d'Ovidio, Stefan Engelen, Isabel Ferrera, Josep M Gasol, Lionel Guidi, Falk Hildebrand, Florian Kokoszka, Cyrille Lepoivre, Gipsi Lima-Mendez, Julie Poulain, Bonnie T Poulos, Marta Royo-Llonch, Hugo Sarmento, Sara Vieira-Silva, Céline Dimier, Marc Picheral, Sarah Searson, Stefanie Kandels-Lewis, Tara Oceans coordinators, Chris Bowler, Colomban de Vargas, Gabriel Gorsky, Nigel Grimsley, Pascal Hingamp, Daniele Iudicone, Olivier Jaillon, Fabrice Not, Hiroyuki Ogata, Stephane Pesant, Sabrina Speich, Lars Stemmann, Matthew B Sullivan, Jean Weissenbach, Patrick Wincker, Eric Karsenti, Jeroen Raes, Silvia G Acinas, and Peer Bork. Ocean plankton. Structure and function of the global ocean microbiome. *Science*, 348(6237):1261359 1–9, May 2015.

[41] Noah Fierer, Jennifer L Morse, Sean T Berthrong, Emily S Bernhardt, and Robert B Jackson. Environmental controls on the landscape-scale biogeography of stream bacterial communities. *Ecology*, 88(9):2162–2173, September 2007.

[42] Stilianos Louca, Laura Wegener Parfrey, and Michael Doebeli. Decoupling function and taxonomy in the global ocean microbiome. *Science*, 353(6305):1272–1277, 2016.

[43] Roman Stocker, Justin R Seymour, Azadeh Samadani, Dana E Hunt, and Martin F Polz. Rapid chemotactic response enables marine bacteria to exploit ephemeral microscale nutrient patches. *Proceedings of the National Academy of Sciences of USA*, 105(11):4209–4214, March 2008.

[44] A Bovallius, B Bucht, R Roffey, and P Anäs. Three-year investigation of the natural airborne bacterial flora at four localities in sweden. *Applied and Environmental Microbiology*, 35(5):847–852, May 1978.

[45] Charles S Elton. *The Ecology of Invasions by Animals and Plants*. Springer, November 2013.

[46] David J Hodgson, Paul B Rainey, and Angus Buckling. Mechanisms linking diversity, productivity and invasibility in experimental bacterial communities. *Proceedings of the Royal Society of London. Series B, Biological Sciences*, 269(1506):2277–2283, November 2002.

[47] Jan Dirk van Elsas, Mario Chiurazzi, Cyrus A Mallon, Dana Elhottova, Václav Kristufek, and Joana Falcão Salles. Microbial diversity determines the invasion of soil by a bacterial pathogen. *Proceedings of the National Academy of Sciences of USA*, 109(4):1159–1164, January 2012.

[48] Zhong Wei, Tianjie Yang, Ville-Petri Friman, Yangchun Xu, Qirong Shen, and Alexandre Jousset. Trophic network architecture of root-associated bacterial communities determines pathogen invasion and plant health. *Nature Communications*, 6:1–9, September 2015.

[49] David Tilman. Community invasibility, recruitment limitation, and grassland biodiversity. *Ecology*, 78(1):81–92, January 1997.

[50] Mikhail Tikhonov. Community-level cohesion without cooperation. *eLife*, 5:e15747–15, June 2016.

[51] Nanxi Lu, Alicia Sanchez-Gorostiaga, Mikhail Tikhonov, and Alvaro Sanchez. Cohesiveness in microbial community coalescence. *bioRxiv*, pages 1–24, January 2019.

[52] Kalin Vetsigian, Rishi Jajoo, and Roy Kishony. Structure and Evolution of Streptomyces Interaction Networks in Soil and In Silico. *PLoS Biology*, 9(10):e1001184, October 2011.

[53] JL Jost, JF Drake, AG Fredrickson, and HM Tsuchiya. Interactions of Tetrahymena pyriformis, Escherichia coli, Azotobacter vinelandii, and glucose in a minimal medium. *Journal of Bacteriology*, 113(2):834, 1973.

[54] Beltran Rodriguez-Brito, LinLin Li, Linda Wegley, Mike Furlan, Florent Angly, Mya Breitbart, John Buchanan, Christelle Desnues, Elizabeth Dinsdale, Robert Edwards, Ben Felts, Matthew Haynes, Hong Liu, David Lipson, Joseph Mahaffy, Anna Belen Martin-Cuadrado, Alex Mira, Jim Nulton, Lejla Pa scaron i cacute, Steve Rayhawk, Jennifer Rodriguez-Mueller, Francisco Rodriguez-Valera, Peter Salamon, Shailaja Srinagesh, Tron Frede Thingstad, Tuong Tran, Rebecca Vega Thurber, Dana Willner, Merry Youle, and Forest Rohwer. Viral and microbial community dynamics in four aquatic environments. *The ISME Journal*, 4(6):739–751, February 2010.

[55] Subbarao V Ravva, Chester Z Sarreal, and Robert E Mandrell. Altered Protozoan and Bacterial Communities and Survival of Escherichia coli O157:H7 in Monensin-Treated Wastewater from a Dairy Lagoon. *PloS ONE*, 8(1):e54782–10, January 2013.

[56] Cyrus Alexander Mallon, Jan Dirk van Elsas, and Joana Falcão Salles. Microbial invasions: the process, patterns, and mechanisms. *Trends in Microbiology*, 23(11):719–729, November 2015.

[57] David L Kirchman. *Processes in Microbial Ecology*. Oxford University Press, 2012.

[58] L Sack, C Zeyl, Graham Bell, T Sharbel, X Reboud, T Bernhardt, and H Koelewyn. Isolation of 4 New Strains of Chlamydomonas-Reinhardtii (Chlorophyta) From Soil Samples. *Journal of phycology*, 30(4):770–773, August 1994.

[59] S Ishii, W B Ksoll, R E Hicks, and M J Sadowsky. Presence and Growth of Naturalized Escherichia coli in Temperate Soils from Lake Superior Watersheds. *Applied and Environmental Microbiology*, 72(1):612–621, January 2006.

[60] Doeke R Hekstra and Stanislas Leibler. Contingency and statistical laws in replicate microbial closed ecosystems. *Cell*, 149(5):1164–1173, May 2012.

[61] Zak Frentz, Seppe Kuehn, and Stanislas Leibler. Strongly deterministic population dynamics in closed microbial communities. *Physical Review X*, 5(4):041014, October 2015.

[62] Zen'ichiro Kawabata, Kazuaki Matsui, K Okazaki, M Nasu, N Nakano, and T SUGAI. Synthesis of a Species-Defined Microcosm with Protozoa. *Journal of Protozoology Research*, 5(1):23–26, January 1995.

[63] Stefanie Widder, Rosalind J Allen, Thomas Pfeiffer, Thomas P Curtis, Carsten Wiuf, William T Sloan, Otto X Cordero, Sam P Brown, Babak Momeni, Wenying Shou, Helen Kettle, Harry J Flint, Andreas F Haas, Béatrice Laroche, Jan-Ulrich Kreft, Paul B Rainey, Shiri Freilich, Stefan Schuster, Kim Milferstedt, Jan R van der Meer, Tobias Grobkopf, Jef Huisman, Andrew Free, Cristian Picioreanu, Christopher Quince, Isaac Klapper, Simon Labarthe, Barth F Smets, Harris Wang, and Orkun S Soyer. Challenges in microbial ecology: Building predictive understanding of community function and dynamics. *ISME Journal*, 10(11):2557–2568, November 2016.

[64] FB Taub, Frieda B Taub, AM Dollar, and Alexander M Dollar. The nutritional inadequacy of Chlorella and Chlamydomonas as food for Daphnia pulex. *Limnol. Oceanogr.*, 13(4):607–617, 1968.

[65] Tom Fenchel. Suspension Feeding in Ciliated Protozoa: Feeding Rates and Their Ecological Significance. *Microbial Ecology*, 6(1):13–25, January 1980.

[66] J F Blom, Y S Zimmermann, T Ammann, and J Pernthaler. Scent of Danger: Floc Formation by a Freshwater Bacterium Is Induced by Supernatants from a Predator-Prey Coculture. *Applied and Environmental Microbiology*, 76(18):6156–6163, September 2010.

[67] Tom Fenchel. Suspension Feeding in Ciliated Protozoa: Functional Response and Particle Size Selection. *Microbial Ecology*, 6(1):1–11, January 1980.

[68] Gianluca Corno and Klaus Jürgens. Direct and indirect effects of protist predation on population size structure of a bacterial strain with high phenotypic plasticity. *Applied and Environmental Microbiology*, 72(1):78–86, January 2006.

[69] P Wojtaszek. Oxidative burst: An early plant response to pathogen infection. *Biochemical Journal*, 322(Pt 3):681–692, 1997.

[70] S Waffenschmidt, J P Woessner, K Beer, and U W Goodenough. Isodityrosine cross-linking mediates insolubilization of cell walls in Chlamydomonas. *The Plant Cell*, 5(7):809–820, July 1993.

[71] Justin R Seymour, Shady A Amin, Jean-Baptiste Raina, and Roman Stocker. Zooming in on the phycosphere: the ecological interface for phytoplankton–bacteria relationships. *Nature Microbiology*, 2:17065–12, May 2017.

[72] Jason Merritt and Seppe Kuehn. Quantitative high-throughput population dynamics in continuous-culture by automated microscopy. *Scientific Reports*, 6:33173–7, September 2016.

[73] Jason Merritt and Seppe Kuehn. Frequency- and Amplitude-Dependent Microbial Population Dynamics during Cycles of Feast and Famine. *Physical Review Letters*, 121(9):098101, August 2018.

[74] M Teplitski. Chlamydomonas reinhardtii Secretes Compounds That Mimic Bacterial Signals and Interfere with Quorum Sensing Regulation in Bacteria. *Plant Physiology*, 134(1):137–146, January 2004.

[75] Leanid Laganenka, Remy Colin, and Victor Sourjik. Chemotaxis towards autoinducer 2 mediates autoaggregation in Escherichia coli. *Nature Communications*, 7:1–10, September 2016.

[76] Eyal Bairey, Eric D Kelsic, and Roy Kishony. High-order species interactions shape ecosystem diversity. *Nature Communications*, 7:1–7, 1.

[77] Jacopo Grilli, György Barabás, Matthew J Michalska-Smith, and Stefano Allesina. Higher-order interactions stabilize dynamics in competitive network models. *Nature Reviews Genetics*, 548(7666):210–213, August 2017.

[78] Daniel Sher, Jessie W Thompson, Nadav Kashtan, Laura Croal, and Sallie W Chisholm. Response of Prochlorococcus ecotypes to co-culture with diverse marine bacteria. *The ISME Journal*, 5(7):1125–1132, February 2011.

[79] JT Wootton and 1994. The nature and consequences of indirect effects in ecological communities. *Annual Review of Ecology and Sytematics*, 25:443–466, January 1994.

[80] J E Losey, RF Denno Ecology, and 1998. Positive predator–predator interactions: enhanced predation rates and synergistic suppression of aphid populations. *Ecology*, 79(6):2143–2152, January 1998.

[81] Jonathan Friedman, Logan M Higgins, and Jeff Gore. Community structure follows simple assembly rules in microbial microcosms. *Nature Ecology & Evolution*, 1(5):109, March 2017.

[82] John H Vandermeer. The competitive structure of communities: an experimental approach with protozoa. *Ecology*, 50(3):362–371, May 1969.

[83] Doeke Hekstra, Simona Cocco, Rémi Monasson, and Stanislas Leibler. Trend and fluctuations: Analysis and design of population dynamics measurements in replicate ecosystems. *Physical Review E*, 88(6):062714, December 2013.

[84] Kazuaki Matsui, Shigeki Kono, Asuka Saeki, Nobuyoshi Ishii, Man-Gi G Min, and Zen'ichiro Kawabata. Direct and indirect interactions for coexistence in a species-defined microcosm. *Hydrobiologia*, 435:109–116, May 2000.

[85] Anthony R Ives, B. Dennis, KL Cottingham, and S.R. Carpenter. Estimating community stability and ecological interactions from time-series data. *Ecological Monographs*, 73(2):301–330, 2003.

[86] Charles K Fisher and Pankaj Mehta. Identifying Keystone Species in the Human Gut Microbiome from Metagenomic Timeseries Using Sparse Linear Regression. *PloS ONE*, 9(7):e102451–10, July 2014.

[87] Richard R Stein, Vanni Bucci, Nora C Toussaint, Charlie G Buffie, Gunnar Ratch, Eric G Pamer, Chris Sander, and Joao Xavier. Ecological modeling from time-series inference: insight into dynamics and stability of intestinal microbiota. *PLoS Computational Biology*, 9(12):e1003388, 2013.

[88] Michael B. Elowitz, Arnold J. Levine, Eric D. Siggia, and Peter S. Swain. Stochastic gene expression in a single cell. *Science*, 297(5584):11831186, Aug 2002.

[89] Tomoya Baba, Takeshi Ara, Miki Hasegawa, Yuki Takai, Yoshiko Okumura, Miki Baba, Kirill A Datsenko, Masaru Tomita, Barry L Wanner, and Hirotada Mori. Construction of Escherichia coli K-12 in-frame, single-gene knockout mutants: the Keio collection. *Molecular Systems Biology*, 2(1):1–11, 2006.

[90] Donna CassidyHanley, Helen R. Smith, and Peter J. Bruns. A simple, efficient technique for freezing tetrahymena thermophila. *Journal of Eukaryotic Microbiology*, 42(5):510515, 1995.

[91] Frieda B. Taub and Alexander M. Dollar. A chlorella-daphnia food-chain study: The design of a compatible chemically defined culture medium 1, 2. *Limnology and Oceanography*, 9(1):6174, 1964.

[92] Doeke Hekstra. *Population Dynamics in a Model Closed Ecosystem.* PhD thesis, The Rockefeller University, 6 2009.

[93] A. Olsén, A Jonsson, and S. Normark. Fibronectin Binding Mediated by a Novel Class of Surface Organelles on Escherichia-Coli. *Nature*, 338(6217):652–655, 1989.

[94] Katherine Dowell Kearns and Mark D. Hunter. Green algal extracellular products regulate antialgal toxin production in a cyanobacterium. *Environmental Microbiology*, 2(3):291297, 2000.

[95] Takefumi Shimoyama, Souichiro Kato, Shunichi Ishii, and Kazuya Watanabe. Flagellum mediates symbiosis. *Science*, 323(5921):15741574, Mar 2009.

[96] Thomas Roach, Chae Sun Na, and Anja Krieger-Liszkay. High light-induced hydrogen peroxide production in chlamydomonas reinhardtii is increased by high co2 availability. *The Plant Journal: For Cell and Molecular Biology*, 81(5):759766, Mar 2015.

[97] Sanders Junglee, Laurent Urban, Huguette Sallanon, and Flicie Lopez-Lauri. Optimized assay for hydrogen peroxide determination in plant tissue using potassium iodide. *American Journal of Analytical Chemistry*, 05(11):730736, 2014.

[98] Thomas Hillen and Amanda Swan. *The Diffusion Limit of Transport Equations in Biology*, page 73129. Lecture Notes in Mathematics. Springer International Publishing, 2016.

[99] Irina Pouneva. Evaluation of algal culture viability and physiological state by fluorescent microscopic methods. *Bulgarian Journal of Plant Physiology*, 23(1-2):67–76, 1997.

[100] Akinobu Ito, Thithiwat May, Koji Kawata, and Satoshi Okabe. Significance of rpoSduring maturation of Escherichia colibiofilms. *Biotechnology and Bioengineering*, 99(6):1462–1471, April 2008.

[101] C Hatzis, P J Sweeney, F Srienc, and Arnie G Fredrickson. Determination of cellular rate distributions in microbial cell populations: feeding rates of ciliated protozoa. *Biotechnology and Bioengineering*, 42(3):284–294, July 1993.

[102] C Hatzis, F Srienc, and Arnie G Fredrickson. Feeding heterogeneity in ciliate populations: Effects of culture age and nutritional state. *Biotechnology and Bioengineering*, 43(5):371–380, March 1994.

[103] J H P Dawes and M O Souza. A derivation of Hollingamp#x00027;s type I, II and III functional responses in predatoramp#x02013;prey systems. *Journal of Theoretical Biology*, 327(c):11–22, June 2013.

[104] C R Curds and A. Cockburn. Studies on the growth and feeding of Tetrahymena pyriformis in axenic and monoxenic culture. *Microbiology*, 54(3):343–358, December 1968.

[105] M Seto and Tazaki T. Carbon dynamics in the food chain system of glucose-Escherichia coli-Tetrahymena vorax. *Japanese Journal of Ecology*, 21(5-6):179–188, December 1971.

[106] M.A. Savageau. Escherichia-Coli Habitats, Cell Types, and Molecular Mechanisms of Gene Control. *American Naturalist*, 122(6):732–744, 1983.

[107] A Celani and M Vergassola. Bacterial strategies for chemotaxis response. *Proceedings of the National Academy of Sciences of USA*, 107(4):1391–1396, January 2010.

[108] O Shoval, H Sheftel, G Shinar, Y Hart, O Ramote, A Mayo, E Dekel, K Kavanagh, and U Alon. Evolutionary trade-offs, Pareto optimality, and the geometry of phenotype space. *Science*, 336(6085):1157–1160, June 2012.

[109] S L Messenger, I J Molineux, and J J Bull. Virulence evolution in a virus obeys a trade-off. *Proceedings of the Royal Society of London. Series B, Biological Sciences*, 266(1417):397–404, February 1999.

[110] Herwig Bachmann, Martin Fischlechner, Iraes Rabbers, Nakul Barfa, Filipe Branco dos Santos, Douwe Molenaar, and Bas Teusink. Availability of public goods shapes the evolution of competing metabolic strategies. *Proceedings of the National Academy of Sciences of USA*, 110(35):14302–14307, August 2013.

[111] R Lande. Quantitative Genetic Analysis of Multivariate Evolution, Applied to Brain: Body Size Allometry. *Evolution*, 33(1):402–416, March 1979.

[112] P R Grant and B R Grant. Predicting Microevolutionary Responses to Directional Selection on Heritable Variation. *Evolution*, 49(2):241–251, April 1995.

[113] Cameron K Ghalambor, Jeffrey A Walker, and David N Reznick. Multi-trait Selection, Adaptation, and Constraints on the Evolution of Burst Swimming Performance. *Integrative and Comparative Biology*, 43(3):431–438, July 2003.

[114] Gregory I Lang, Daniel P Rice, Mark J Hickman, Erica Sodergren, George M Weinstock, David Botstein, and Michael M Desai. Pervasive genetic hitchhiking and clonal interference in forty evolving yeast populations. *Nature*, 500(7464):571–574, August 2013.

[115] V S Cooper and R E Lenski. The population genetics of ecological specialization in evolving Escherichia coli populations. *Nature*, 407(6805):736–739, October 2000.

[116] X Yi and A M Dean. Phenotypic plasticity as an adaptation to a functional trade-off. *eLife*, 5(e19307):1–12, October 2016.

[117] P Righetti, B C W Brost, and R S Snyder. On the Limiting Pore Size of Hydrophilic Gels for Electrophoresis and Isoelectric Focusing. *Journal of Biochemical and Biophysical Methods*, 4(5-6):347–363, June 1981.

[118] Mounir Maaloum, Nadine Pernodet, and Bernard Tinland. Agarose gel structure using atomic force microscopy: Gel concentration and ionic strength effects. *Electrophoresis*, 19(10):1606–1610, July 1998.

[119] J Adler. Chemotaxis in Bacteria. *Science*, 153(3737):708–716, August 1966.

[120] A J Wolfe and H C Berg. Migration of Bacteria in Semisolid Agar. *Proceedings of the National Academy of Sciences of USA*, 86(18):6973–6977, September 1989.

[121] Ottavio A Croze, Gail P Ferguson, Michael E Cates, and Wilson C K Poon. Migration of chemotactic bacteria in soft agar: role of gel concentration. *Biophysical Journal*, 101(3):525–534, August 2011.

[122] Daniel A Koster, Avraham Mayo, Anat Bren, and Uri Alon. Surface Growth of a Motile Bacterial Population Resembles Growth in a Chemostat. *Journal of Molecular Biology*, 424(3-4):180–191, December 2012.

[123] Evelyn F Keller and Lee A Segel. Traveling bands of chemotactic bacteria: a theoretical analysis. *Journal of Theoretical Biology*, 30(2):235–248, February 1971.

[124] M J Tindall, P K Maini, S L Porter, and J P Armitage. Overview of mathematical approaches used to model bacterial chemotaxis II: bacterial populations. *Bulletin of Mathematical Biology*, 70(6):1570–1607, August 2008.

[125] David T Fraebel, Harry Mickalide, Diane Schnitkey, Jason Merritt, Thomas E Kuhlman, and Seppe Kuehn. Environment determines evolutionary trajectory in a constrained phenotypic space. *eLife*, 6:e24669, Mar 2017.

[126] David Jordan, Seppe Kuehn, Eleni Katifori, and Stanislas Leibler. Behavioral diversity in microbes and low-dimensional phenotypic spaces. *Proceedings of the National Academy of Sciences of USA*, 110(34):14018–14023, 2013.

[127] H C Berg and D A Brown. Chemotaxis in Escherichia coli analysed by three-dimensional tracking. *Nature*, 239(5374):500–504, October 1972.

[128] K M Taute, S Gude, S J Tans, and T S Shimizu. High-throughput 3D tracking of bacteria on a standard phase contrast microscope. *Nature communications*, 6(8776):1–9, November 2015.

[129] Dave van Ditmarsch, Kerry E Boyle, Hassan Sakhtah, Jennifer E Oyler, Carey D Nadell, Éric Déziel, Lars E P Dietrich, and Joao B Xavier. Convergent evolution of hyperswarming leads to impaired biofilm formation in pathogenic bacteria. *Cell reports*, 4(4):697–708, August 2013.

[130] Maxime Deforet, Dave van Ditmarsch, Carlos Carmona-Fontaine, and Joao B Xavier. Hyperswarming adaptations in a bacterium improve collective motility without enhancing single cell motility. *Soft Matter*, 10(14):2405–2413, April 2014.

[131] S Taheri-Araghi, S Bradde, J T Sauls, N S Hill, and P A Levin. Cell-size control and homeostasis in bacteria. *Current Biology*, 25:385–391, 2015.

[132] Jason Merritt. *Dynamic aggregation and dispersal of Escherichia coli under cycles of feast and famine*. PhD thesis, University of Illinois at Urbana-Champaign, 8 2018.

Appendix A

Construction and calibration of custom-culture devices

A.1 Introduction

To carry out experiments, we constructed eight custom, low-cost culture devices capable of sustaining cultures of algae, bacteria, and ciliates for periods of weeks while keeping constant temperature (30 °C) and light (typically 1600 or 4200 Lux). Each system houses a culture of inital volume 25 mL in a glass vial in a custom machined aluminum block. The culture vial is in thermal contact with the aluminum block, which is temperature controlled via computer-controlled PID feedback to a thermoelectric heating-cooling element (Peltier). The program for feedback is run on a Raspberry Pi. The vial is heated from underneath with an LED. A magnetic stir bar (SBM-15045-PLA) and commercial inductive stir plate (Cimarec i Mono) mix the culture. These devices follow closely the design created by Dr. Jason Merritt [132] with some minor changes.

A.2 Custom machined and printed parts

Because the culture devices used in our experiments were custom-designed, three elements had to be custom-machined. These three elements are only slightly different from those used and designed by Dr. Jason Merritt [132], the differences being that the connector here has holes in the top for the attachment of fans (whereas Jason's does not) and also that the plate here is attached to an LED and connects the stir-plate to the 3D-printed base (whereas Jason's plate has no LED and connects the optical table to the holder). The machining of these three elements was outsourced to the CNC machining service eMachineShop. They are

- The custom "holder" part (Fig. A.3), which houses the culture vial and the

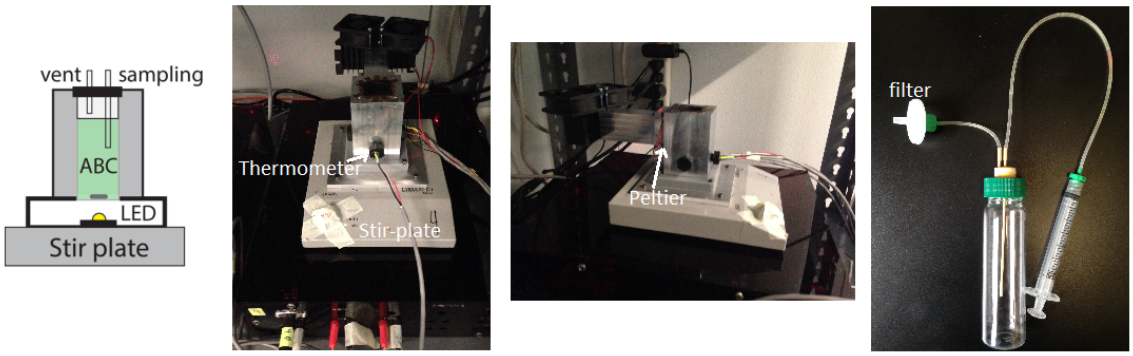

Figure A.1: Custom culture-device. System temperature is set by a Peltier element and feedback to a thermometer and brightness is set by LED. The culture vial is stirred with an inductive stir plate. Gas exchange (venting) with the atmosphere is accomplished with an autoclavable 0.1μm filter (Whatman 6784-2501). Sampling is performed with a syringe attached to 0.04" PEEK tubing (Fisher scientific) that is submerged in the culture in the vial. After a sample is drawn up into the syringe, the syringe is removed and a fresh syringe is quickly attached to minimize chance of contamination. In the pictures here, the vial is not inside the holder metal block like it would be in an experiment.

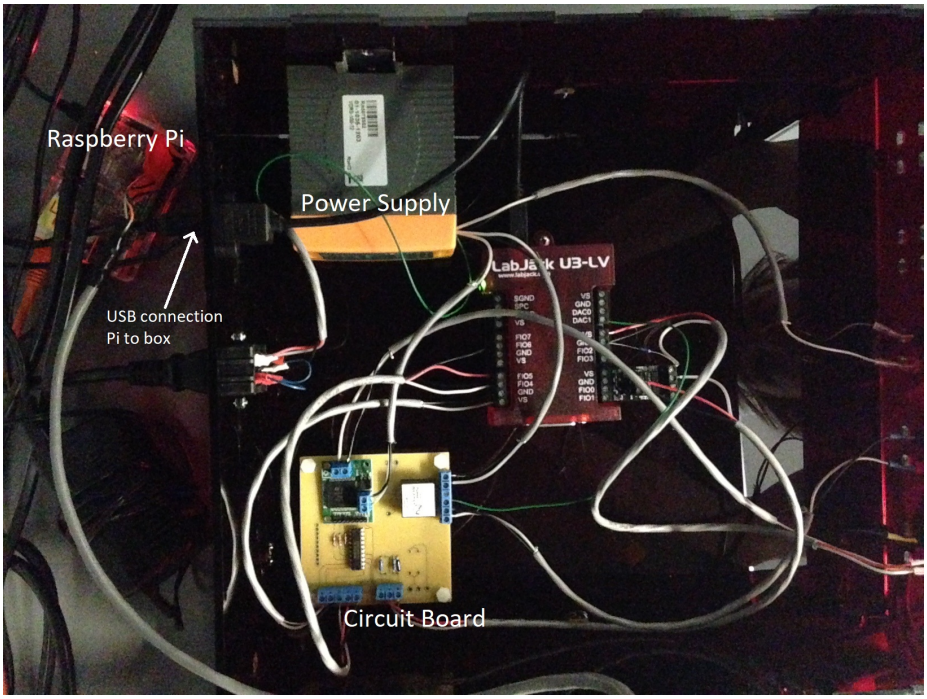

Figure A.2: Electronics box for custom-culture devices with power supply, custom circuit board and LabJack DAQ device. Raspberry Pi is outside the box.

temperature probe used for temperature control. The holder itself is also the direct object of the temperature control used in the experiments, with thermal contact to the culture vial increased by adding strips of copper tape to the vial hole for a tighter fit. The inside of the holder is spray painted black to eliminate reflections from the LED. Copper tape and black paint visible in Fig. A.1.

- The custom "connector" part (Fig. A.4), which is used to mount the peltier heating device (12711-5L31-03CQ Custom Thermoelectric) to the holder and which connects to a large heat sink at the other end. Any heating or cooling applied by the peltier to the holder is applied oppositely to the connector and thus the heat sink is necessary for preventing the connector from reaching extreme temperatures. Additionally, fans which are attached to the connector blow on the heat sink to dissipate and prevent the accumulation of heat/cold.

- The custom "plate" part (Fig. A.5), which is bolted on to the stir-plate and which the LED (Cree XLamp XP-E2 Single 1 Up Neutral White 4000 K color temperature, LED Supply p/n: CREEXPE2-740-1) is screwed into. The plate is further attached to the 3D-printed "base" which attaches to the holder. The vial sits on a piece of acrylic (McMaster Carr Optically Clear Cast Acrylic Sheet 1/16" thick) which is attached to the base. The LED shines up from the plate, through the acrylic, and thus illuminates the vial from the bottom.

As just mentioned, a "base" part (Fig. A.6) was designed and printed on a 3D printer (FormLabs Form 1+ with grey resin FLGPGR02). The base serves to attach the plate to the holder. The holder cannot sit directly on the plate because of the LED on the plate. The base provides distance between the LED and the bottom of the vial. When a vial is inserted into the holder, it comes to sit on the transparent piece of acrylic which is glued into a recessed square on the base. Note that a neutral density filter with ND 0.9 which corresponds to 12.5% transmittance (Lee Filters 211) is sandwiched between the acrylic and vial so as to reduce the intensity of the LED.

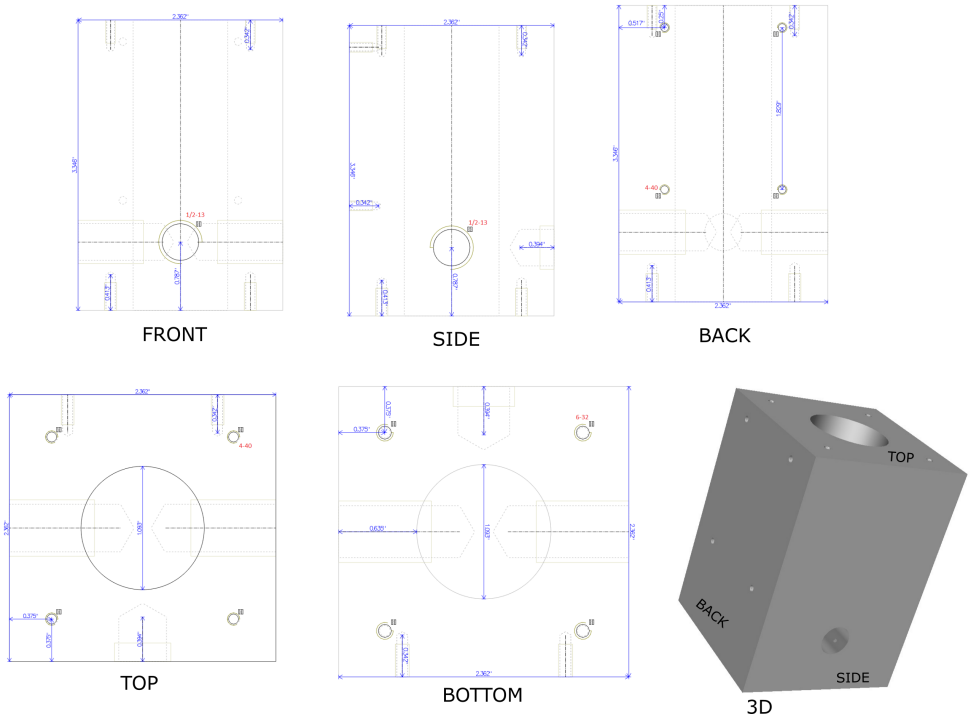

Figure A.3: Custom "holder" machined part manufactured by eMachineShop. Holder houses Chemglass CG-4902-08 40 mL vial (ChemGlass) containing microbial culture. Temperature control is achieved using a Peltier heat pump mounted on the back and a EI1034 temperature probe which is in thermal contact with the front. This thermal contact between the temperature probe and the holder is achieved by hollowing out a 1/2"-13 nylon screw, epoxying the temperature probe into that nylon screw, applying thermal paste into the hole on the front of the holder, and then screwing the hybrid screw/temperature-probe into that hole until the temperature probe sinks into the thermal paste. Side 1/2"-13 mounting holes are not used for measurements are simply plugged up with 1/2"-13 nylon screws. 6-32 holes at bottom mount the holder to the 3D-printed base.

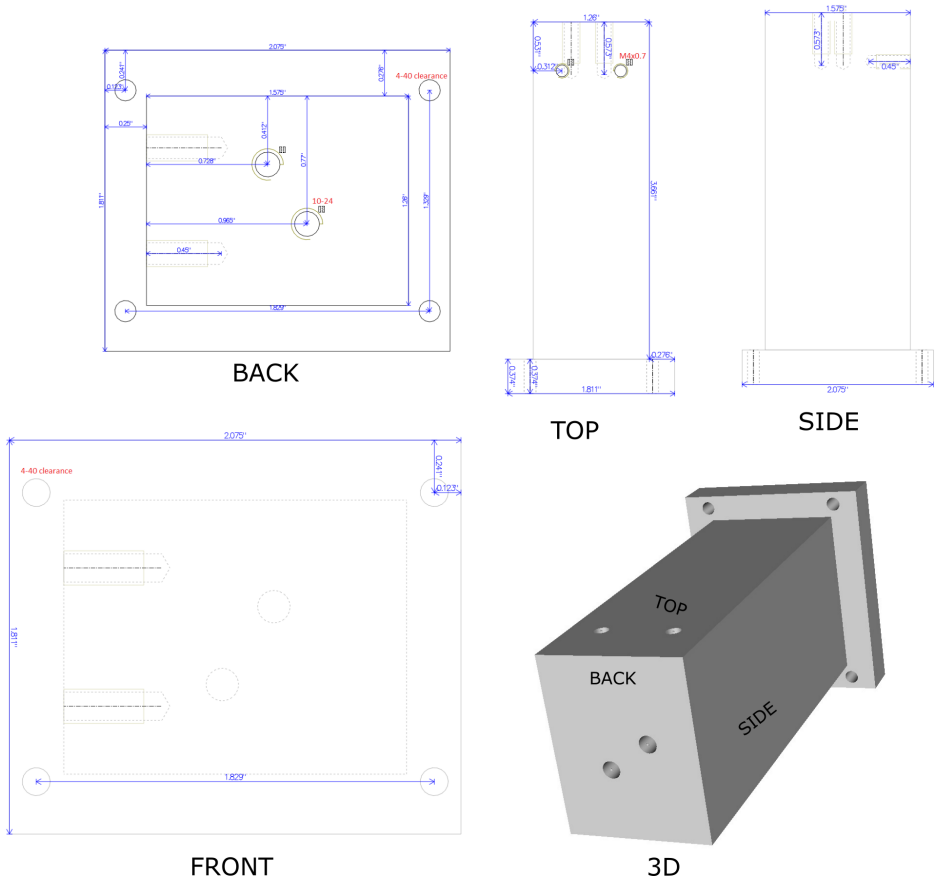

Figure A.4: Custom "connector" machined part manufactured by eMachineShop. Connector functions as a heat conductor from one side of a Peltier heat pump to a Wakefield-Vette 401A heat sink affixed via 10-24 holes at the end. Fans are affixed to the top via M4x0.7 holes to dissipate heat from the heat sink. Through-holes at front allow connection to the machined "holder" part housing the vial, with the Peltier element held between the two by compression. Thermal paste is applied to both sides of the Peltier to facilitate thermal conductivity between the Peltier and the connector and between the Peltier and the holder.

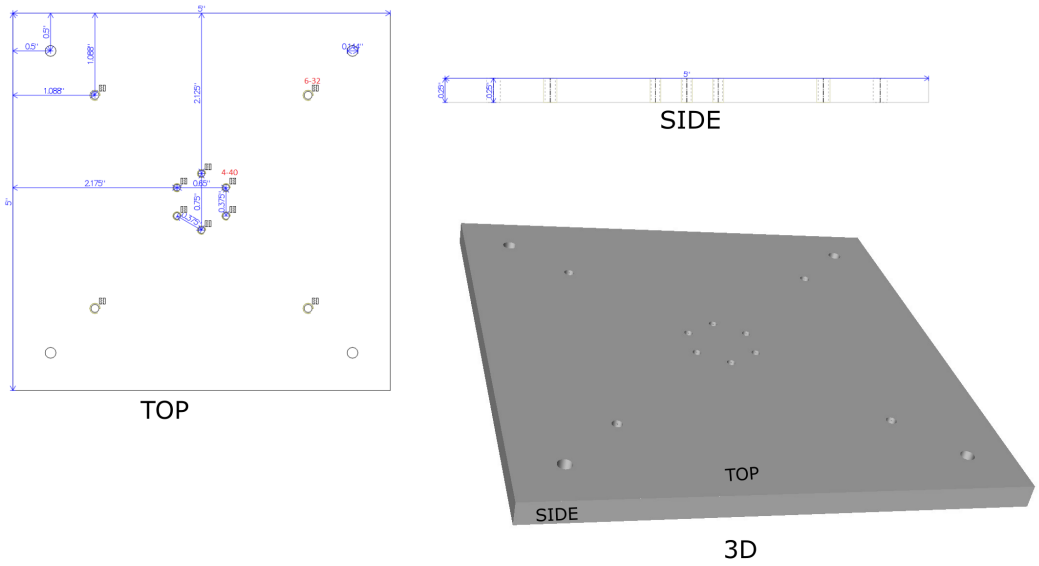

Figure A.5: Custom "plate" machined part manufactured by eMachineShop. 4-40 holes at center allow mounting of LED (Cree XLamp XP-E2 Single 1 Up Neutral White 4000 K color temperature, LED Supply p/n: CREEXPE2-740-1) with thermal paste in between. 6-32 holes allow mounting of 3D-printed base to the plate. 0.144" clearance holes allow mounting of plate to the Cimarec i Mono inductive stir-plate. Holes were machined into the top of the stir-plate with the same geometry as the holes on the plate and the mounting was accomplished via nuts and bolts.

A.3 Electronics box schematics

A custom electronics box was designed to house the electronics used to control each custom-culture device. The design used in this study is a simplified version of that used by Dr. Jason Merritt [132]. Temperature and light-control programs are run on a Raspberry Pi which is connected to the electronics box. The electronics box itself was cut out of 4.5 mm acrylic (Fig. A.7) by the laser cutting company Ponoko, with mounting tabs tapped by hand and epoxied in place to allow the sides to be connected with screws. The electronics box holds three main components:

- A LabJack U3-LV DAQ device for control of other circuitry and internal parts.
- A custom circuit board (Fig. A.10) which contains the circuits used for temperature control and the LED driver. The motor driver (VNH2SP30 Pololu) controlling the Peltier heat pump also mounts directly to this part.
- A high-current VDRS-100-12 12 V power supply which powers the parts used in this custom-culture device, including the peltier heat pump, fans, and LED. To work properly with the LabJack-driven motor driver, the power supply output

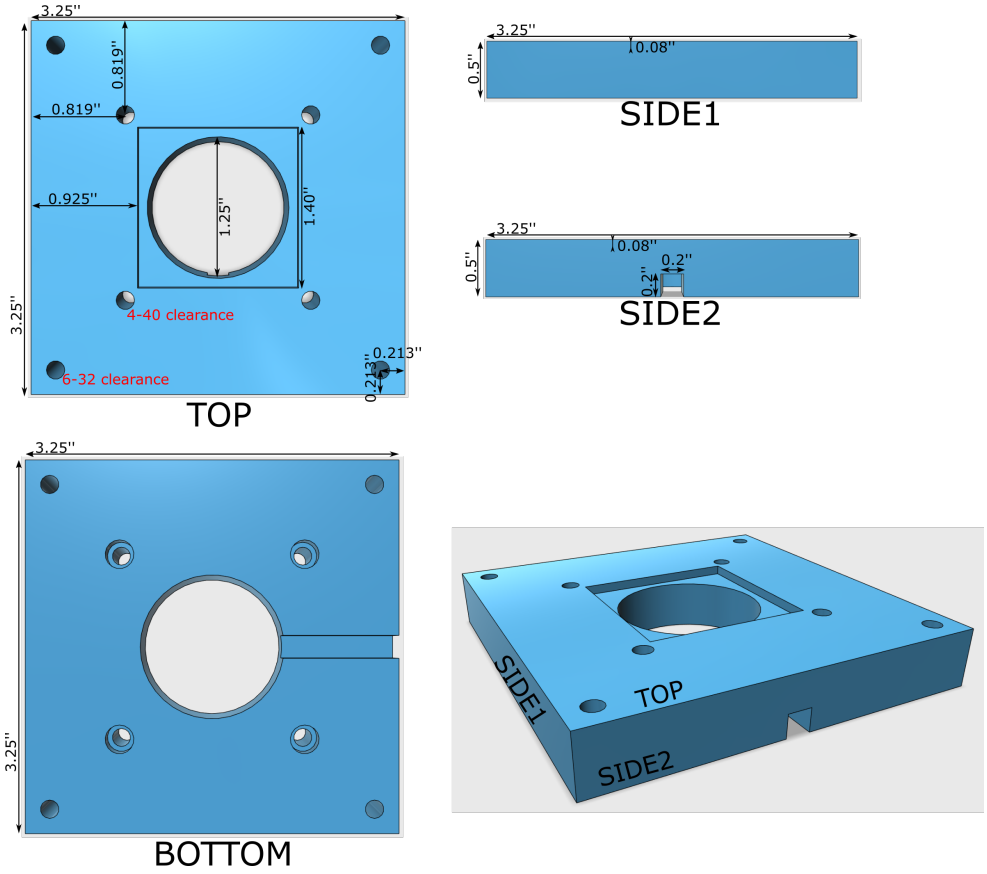

Figure A.6: Custom 3D-printed "base" part. 6-32 holes allow mounting of 3D-printed base to the plate. 4-40 clearance holes allow mounting of base to holder. Extra space is removed from these 4-40 holes at the bottom of the base so that when screws are inserted in at the bottom and up further into the holder, the heads of the screws fit neatly into base and the base can still lay flat against the plate. A 1.40" sided square is cut out of the top of the base to depth 0.08" so that a 1/16" thick square of acrylic (McMaster Carr Optically Clear Cast Acrylic Sheet) can be epoxied in. The vial sits on top of this acrylic. The acrylic is transparent to allow the plate-mounted LED to shine on the bottom of the vial. A trench runs from the center of the base to side2 so as to allow egress of the wires that feed current to the LED. A neutral density filter with 12.5% transmittance (Lee Filters 211) sits on top of the acrylic to reduce intensity of LED.

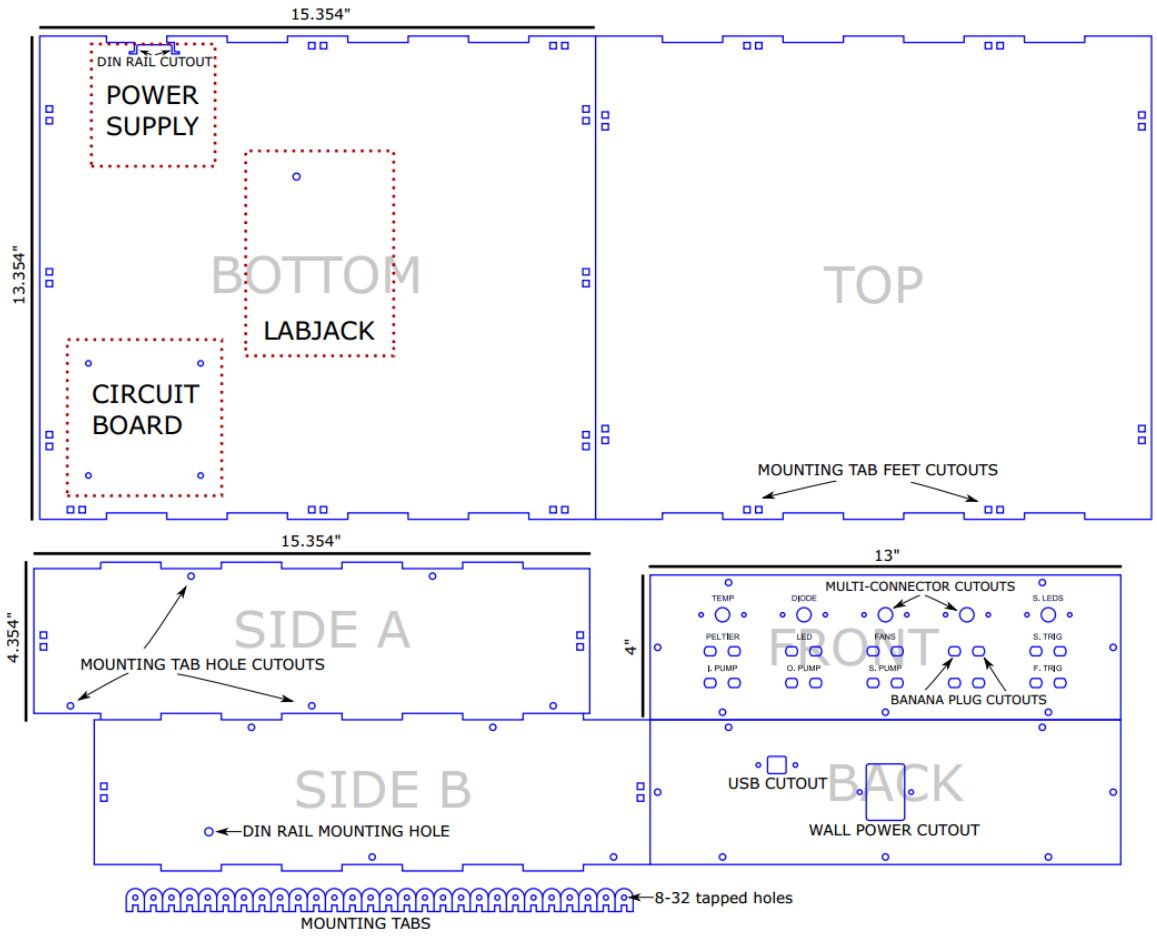

Figure A.7: Electronics box laser cutting schematics. Basic layout of components inside electronics box presented at top left. Laser cut parts produced by Ponoko in 4.5 mm acrylic sheets. Raspberry Pi connects to the electronics box through the USB cutout on back. The only cutouts on front which are used are "TEMP", "PELTIER", "LED", and "FANS".

must be manually grounded by connecting ground to the low voltage output (green wire drawn across power supply in Figs. A.8 and Fig. A.9).

Because the internals of the electronics box are fairly complex (Fig. A.2), included here are separate schematics for LED control and fans (Fig. A.8) and temperature control (Fig. A.9). Also included is a diagram of the custom circuit board used in the experiment (Fig. A.10).

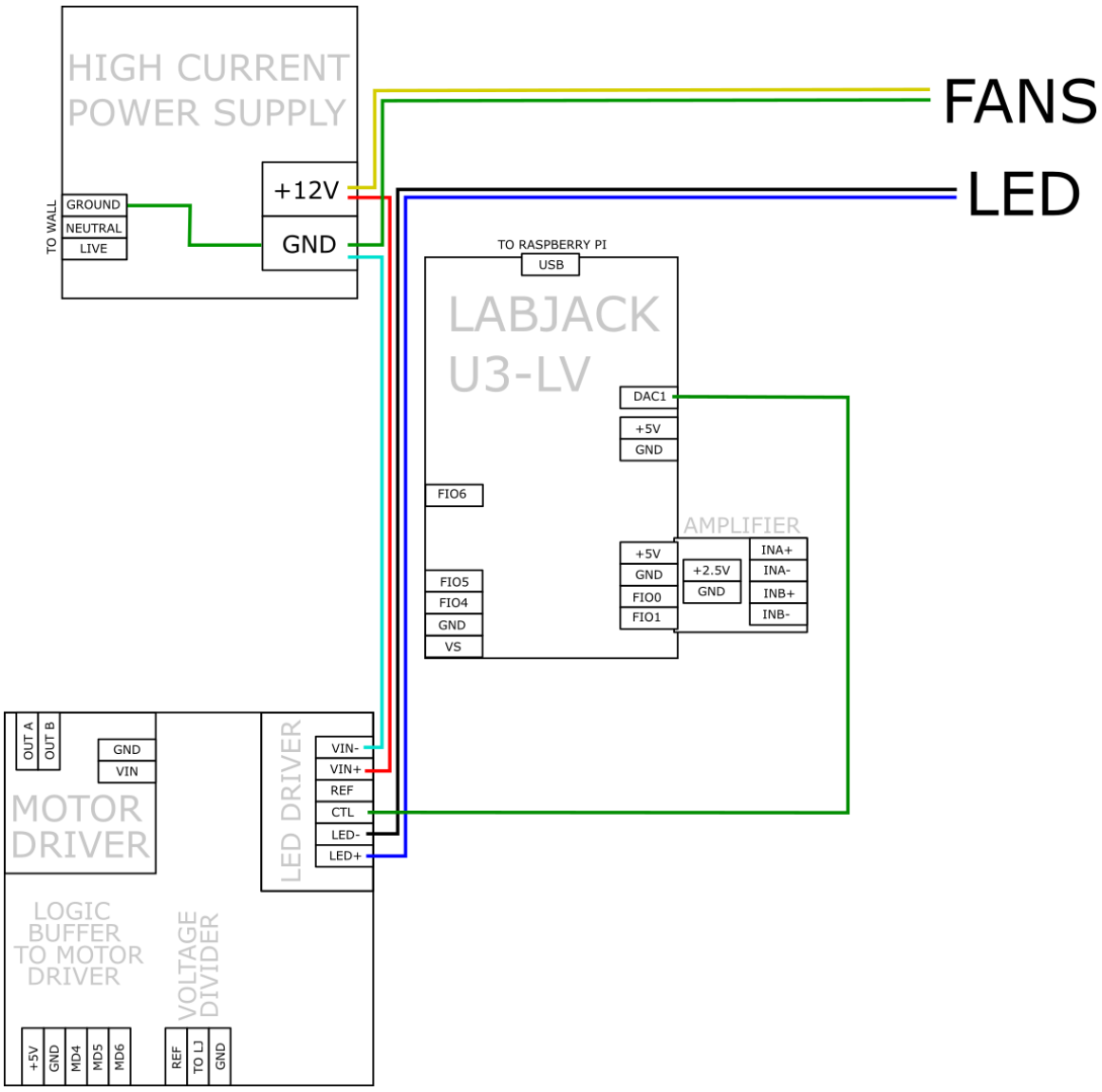

Figure A.8: Schematic for LED and fan wiring inside electronics box. Fans are always on. LED brightness is controlled by differing voltage sent from the analog DAC1 pin of the Labjack to the CTL pin of the LED driver (Buckpuck 03021-d-e-350). That voltage is controlled by the program run on Raspberry Pi.

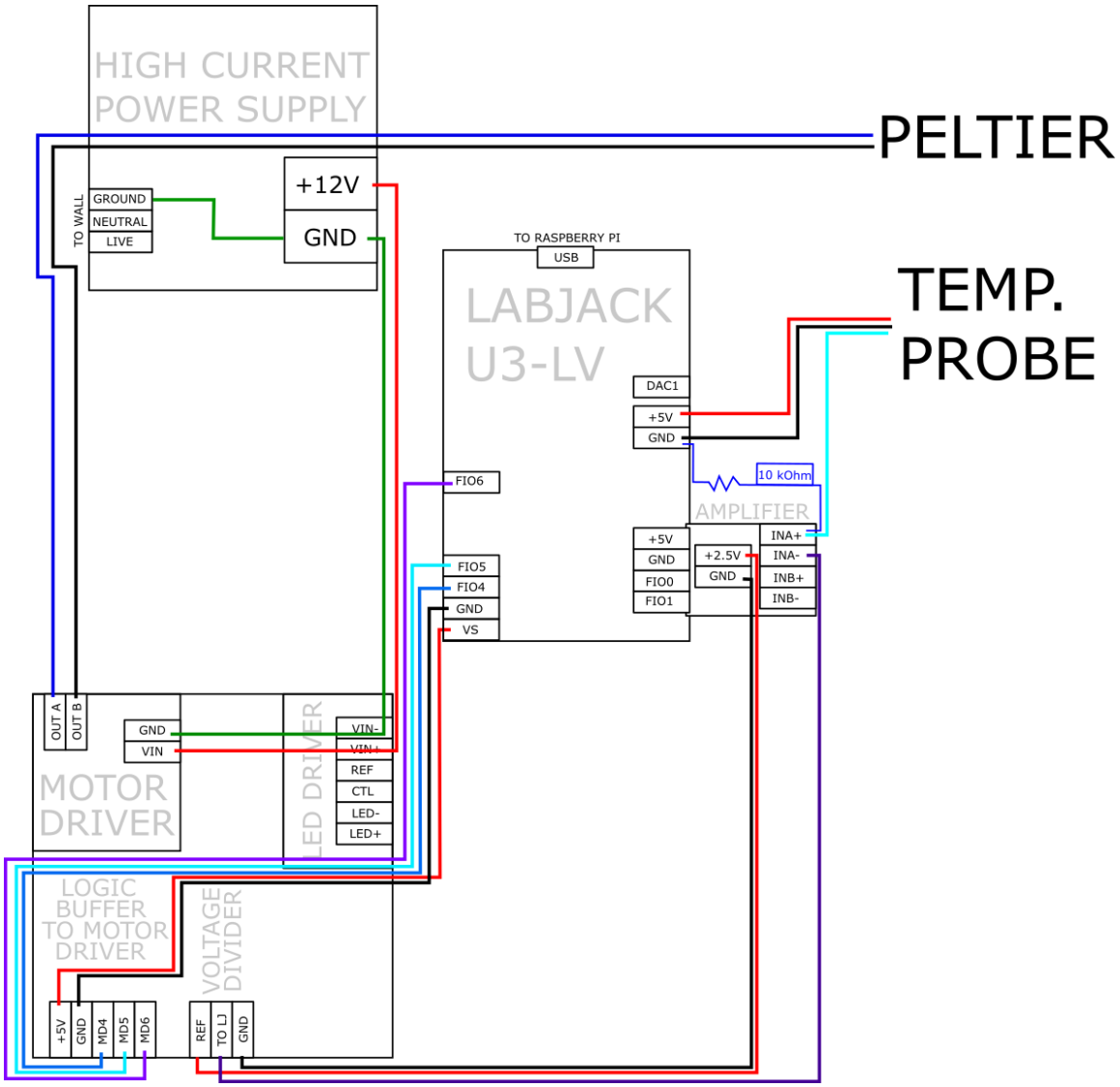

Figure A.9: Schematic for temperature control wiring inside electronics box. LabJack signals to motor driver control direction of Peltier heat pump, with PWM signal controlling Peltier duty cycle. The difference between the output of a voltage divider and the reading from a temperature probe is amplified with LJTick-InAmps (LabJack) to obtain an accurate temperature measurement from the custom-culture device.

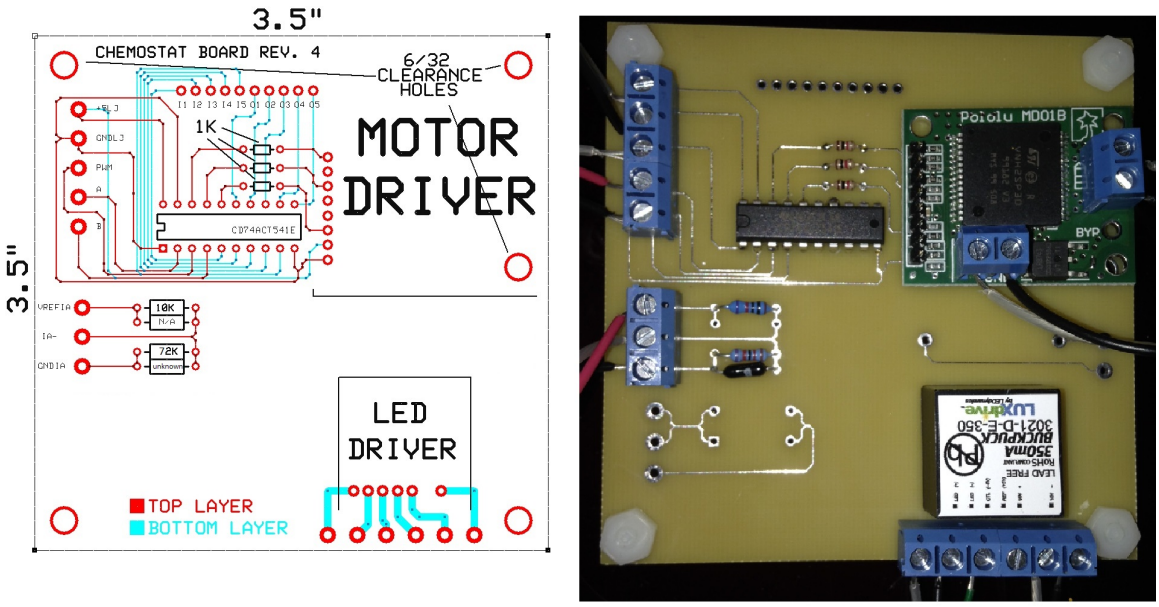

Figure A.10: Custom-culture device custom circuit board. Left: final revision of circuit board schematic, with minor changes including improved hole arrangement and added holes for mounting voltage divider resistors in parallel. Right: actual circuit board appearance as used in experiments.

A.4 Miscellaneous details for building the custom-culture devices

We soldered a "thermal break" on to the LM34 temperature sensors used to perform feedback in the custom-culture devices. We were worried that heat was being conducted along the shielded gray cable that connects the LM34 to the electronics box and that this conducted heat was distorting the measurement the LM34 was making of the temperature of the "holder" metal block. In an attempt to solve this problem, we cut the three metal prongs of the LM34 temperature sensor in half, soldered thin wire on to each prong, and then soldered those thin wires on to the wires in the shielded grey cable. The thinnness of the wire makes for poor thermal conductivity between the shielded grey cable and the LM34. By using an external thermometer to measure the real temperature in the vial, we found that installing the thermal break on the LM34 decreased the noise in the real temperature in the vial by a factor of three. To obtain thin wire, we unbraided # 18-16/30 PVC Type MW-U MIL-W-76B wire and used the single strands that had made up that braid for the thin wire in the thermal break.

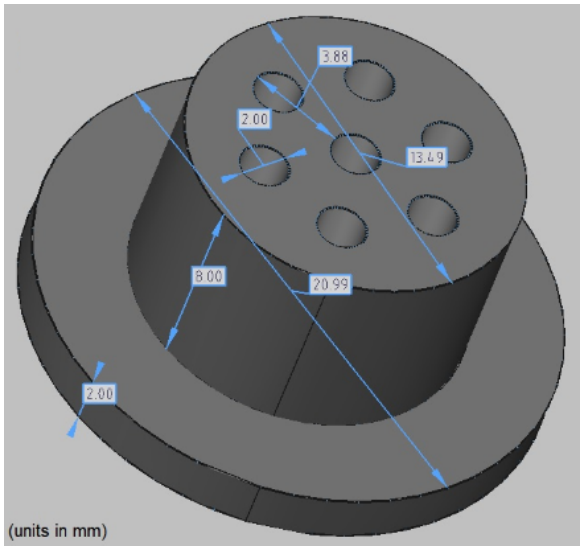

Figure A.11: This is the custom 3D-printed autoclavable nylon 'cap' from Stratasys. PEEK tubing is slid through the cap. One PEEK tube is used for sampling while another is used for venting. The one for sampling extends well below the cap so that it would be submerged in culture. The one for venting extends only a little ways below the cap so that it does not touch culture. The PEEK tubing is secured on to the cap with autoclavable epoxy. The other holes five holes are filled in with the same autoclavable epoxy.

We had found that the temperature of the vial on one system was running especially hot. After many false starts in troubleshooting, we discovered that the power supply for the stir-plate on that system was hot to the touch. Swapping out the power supply fixed the problem. As an additional note on power supplies, there is an option on the physical power supply to be set to stirring power 1 or 5. We set all of ours to 1 for the sake of consistency and also in the hope that they would not run as hot with this setting.

For measuring temperature, the LM34 temperature sensor is obtained by removing the stainless steel tube from a EI1034 temperature probe thus revealing the LM34 underneath. That LM34 temperature sensor is then epoxied into a hollowed out nylon screw and brought into thermal contact with the holder metal block.

We used 40 mL CG-4902-08 glass vials (ChemGlass) to house the cultures. Any plastic connectors or luer fittings were from Nordson Medical. Tubes were mounted into the culture vials using a custom 3D-printed autoclavable nylon 'cap' (Stratasys) (Fig. A.11).

A.5 Temperature Calibration

Recall the setup being used to measure temperature in our systems. An LM34 temperature sensor (which we obtained by removing the stainless steel tube from a EI1034 temperature probe thus revealing the LM34 underneath) is epoxied into a hollowed out nylon screw. This screw is screwed into the "holder" metal block so that the LM34 makes thermal contact with the holder. The holder itself houses and is in thermal contact with the vial which holds the ecosystem. The temperature sensed by the LM34 temperature sensor is turned into a voltage which is then shifted and amplified before being sent to the Labjack. The voltage is continously read by the Labjack and sent to the Raspberry Pi which runs a program "culture_run_ecoPi1" (for the copy on system 1, for example).

Calibration must be performed in order to find the function that relates the voltage read by the Labjack to the actual temperature inside the vial. There are two phases to this calibration. In phase 1 we calibrate a "helper LM34" which is not epoxied into a nylon screw and which will always be plugged into the electronics box of System 2 when in use. The motivation for finding temperature-voltage relationship for this helper LM34 is to be able to place it in the vials of systems *other than System 2* and continuously measure the temperature in those other systems. That way, in phase 2 when we calibrate the temperature-voltage relationship for the actual LM34s which will be used in experiments, we can measure temperature continuously with the helper LM34 rather than manually with the digital thermometer (Fisher Scientific 15-081-102) which would require writing temperatures by hand every minute for hours. We considered buying the software that would allow the digital thermometer to write its temperature to a computer during calibration, but found that software to be prohibitively expensive.

A.5.1 Phase 1: Calibrating the helper LM34

Here are the steps to calibrate the helper LM34.

1. Unplug the LM34 temperature sensor that is native to System 2 from the System 2 electronics box.

2. Plug the helper LM34 into the electronics box of System 2.

3. Place the helper LM34 into a nylon glove and submerge the now-waterproofed helper LM34 into a vial containing 25 mL of water.

4. Place that vial into the holder of System 1.

5. Unplug the System 2 peltier from the Sytem 2 electronics box. This step is done so that System 2 does not actually experience any heating or cooling when we run the program on System 2 and the program tries to feed back on the temperature signal of the helper LM34 (which would, of course, be useless, given that heating or cooling System 2 would not change the temperature of System 1 whose vial is being measured by the helper LM34)

6. Place the digital thermometer into the vial in System 1.

7. In the program on the Raspberry Pi connected to System 1, set the setpoint voltage to 1.1 (it is irrelevant what the setpoint voltage is in the program for System 2).

8. Using Raspberry Pi 1, start the program for System 1.

9. Using Raspberry Pi 2, start the program for System 2.

10. After waiting thirty minutes so that System 1 can reach and maintain its setpoint voltage, write down the temperature on the digital thermometer once a minute for fifteen minutes. Each time you write down a temperature, also write down what the time is on the readout from System 2.

11. While allowing the program for System 2 to run uninterrupted, repeat steps 7, 8, and 10, this time setting the setpoint voltage on System 1 to 1.3. Then 1.5. Then 1.6. (After this point we can ignore the setpoint voltages. They were useful for giving us a spread of temperatures in the vial but will not figure into any calculations)

12. For each time readout on System 2, there is a corresponding voltage readout. Because you know how the temperature you measured with digital thermometer correspond to the time on System 2, you can make a plot of actual temperature in the vial versus the voltage readout on System 2. By calculating a trendline for this plot, you have calibrated the helper LM34. You now know how real

temperature of the helper LM34 is related to the voltage readout by System 2 when System 2 is plugged into that helper LM34.

A.5.2 Phase 2: Calibrating the actual systems

Here are the steps to calibrate for temperature on, for example, System 3.

1. Unplug the LM34 temperature sensor that is native to System 2 from the System 2 electronics box.
2. Plug the helper LM34 into the electronics box of System 2.
3. Place the helper LM34 into a nylon glove and submerge the now-waterproofed helper LM34 into a vial containing 25 mL of water.
4. Place that vial into the holder of System 3.
5. Unplug the System 2 peltier from the Sytem 2 electronics box. This step is done so that System 2 does not actually experience any heating or cooling when we run the program on System 2 and the program tries to feed back on the temperature signal of the helper LM34 (which would, of course, be useless, given that heating or cooling System 2 would not change the temperature of System 3 whose vial is being measured by the helper LM34)
6. In the program on the Raspberry Pi connected to System 3, set the setpoint voltage to 1.1 (it is irrelevant what the setpoint voltage is in the program for System 2).
7. Using Raspberry Pi 3, start the program for System 3.
8. Using Raspberry Pi 2, start the program for System 2.
9. After waiting thirty minutes so that System 3 can reach and maintain its setpoint voltage, write down the time as given by the output of System 2 and wait an additional fifteen minutes so that data is gathered.
10. While allowing the program for System 2 to run uninterrupted, repeat steps 6, 7, and 9, this time setting the setpoint voltage on System 3 to 1.3. Then 1.5. Then 1.6.

11. For each setpoint voltage on System 3, compute the average voltage as read by System 2 during the relevant 15 minutes of data gathering, and use the known calibration from Phase 1 to turn that average voltage into an average real temperature. Plot average real temperature as measured by System 2 versus setpoint voltage on System 3 and calculate a trendline. You now know how the voltage on System 3 is related to actual temperature in the vial of System 3.

The steps in Phase 2 are repeated on all systems to calibrate the temperature for all systems. The reader may wonder how the calibration is performed on System 2 if System 2 is also being used to measure real temperature with the helper LM34. The resolution to this problem is that the Phase 1 helper LM34 calibration was also performed with a different helper LM34 plugged into System 6 and then System 6 was used to measure the real temperature in the vial of System 2 when calibrating System 2.

All calibration was performed in the environmental room with the LEDs off and with the stir-plates on and stir-bars in the vials. It was observed that having the LED shining at brightness 3000 Lux (meaning average light intensity experienced by a cell, the same measure of brightness used in chapter 2) increases the temperature in the vial by 0.05 °C relative to the LED being off. 3000 Lux is about halfway between the two main light levels used in experiments: 1600 and 4200 Lux. The reader may wonder how it is possible for the LED to elevate the temperature of the vial when the whole point of constructing these systems was to perform feedback heating and cooling to maintain set temperatures. The answer is that the thermometer performing temperature measurements is embedded in the "holder" metal block, not the vial, and so any temperature difference between the vial and the holder is inaccessible to temperature feedback. The LED shines directly on the vial, rather than the metal block, and, given that there is not perfect thermal conductivity between the vial and the metal block, the LED preferentially heats the vial.

Minimizing temperature increase due to the LED was one of the motivations for using a neutral density filter with 12.5% transmittance as opposed to a neutral density filter with 6.25% transmittance. Using a neutral density filter with higher transmittance allowed us to achieve our brightness goals with less current applied to the LED and therefore less heat generation. The sacrifice that comes with using a neutral

density filter with higher transmittance is that it limits the minimum brightness we can achieve: the LED has a raw minimum brightness it can reach before turning off and therefore the real minimum brightness experienced by the vial is equal to that raw minimum brightness multiplied by the transmittance of the neutral density filter.

After calibrating the systems, the code (program "culture_run_ecoPi3.py" in the case of System 3 for example) was modified so that the user can input directly the temperature that they want in the line "tempGoal = 30". Then in a later line, that setpoint temperature is converted into a setpoint voltage using the function computed in Phase 2 calibration.

There was a period in time in which we experimented with designs that lacked temperature control and just vented the area underneath the vial with fans, but the prototypes were all unsuccessful.

A.6 Light Calibration

Recall that vials in these systems are illuminated from below with an LED. The LED is driven by an LED driver inside the electronics box. Voltage supplied to the control pin of the BuckPuck by an analog output of the Labjack determines the brightness of the LED. The voltage of this analog output can be set to anywhere between 0 and 5V[1] In code, one sets the output to 0V by calling d.getFeedback([u3.DAC8(1,0)]) and to 5V by calling d.getFeedback([u3.DAC8(1,255)]). A number intermediate between 0 and 255 is used to output a voltage intermediate between 0 and 5V. The brightness of the LED is inversely related to the voltage applied to the control pin, with 0 corresponding to full brightness and 5V corresponding to no light. Calibration is performed to find the function that relates the "control number", which lies between 0 and 255, and the actual brightness of the LED, as measured from the top of the "holder" metal block with a light meter (LED Light Meter PCE-LED 20).

Here are the steps to calibrate light on a system.

1. In code, set the control number to 215.

[1]On a technical note, the output is not true analog but is instead pulse-width modulation (PWM). PWM achieves effective voltages through rapid cycling (732Hz in the case of the DAC1 output on the Labjack). For example, if the output rapidly cycles between 0 and 5V, spending equal time on each voltage in each cycle, that would result in an effective voltage of 2.5V

2. Measure the brightness at the top of the "holder" metal block. This process involves jamming the detector of the light meter against the hole at the top of the block, and slowly translating the detector until one finds the maximum value. Note that there is no vial in the holder during calibration.

3. Repeat measurement for control numbers 210, 205, 200, 190, 180, 170, and 160.

4. Plot control number versus measured brightness and fit a quartic. You now have a function that relates the brightness of the LED to the control number supplied to that LED.

After calibration, the code (program "culture_run_ecoPi4.py" for system 4, for example) was modified so that one can input their desired brightness and the code will use the function from calibration to find the correct control number. For example, if one wanted the brightness at the top of the holder metal block to be 400 Lux, one would edit the code so that a certain line reads "Lux = 400". Brightnesses only went up to about 420 during calibration so values higher than that are not calibrated for.

Over time, the quality of the calibration degraded and I stopped relying on it. I would instead, at the beginning of an experiment, manually change the control number in the code and subsequently measure the brightness until I got the brightness I wanted. This decline in quality was likely due to the neutral density filters degrading. Supporting this hypothesis is the fact that brightnesses would be higher at the end of experiments than the beginning, consistent with a neutral density filter degrading.

While we can only measure brightness at the top of the holder (the light meter does not fit into the inside the hole), this measure is not the most relevant one. No cells are at that height. The more relevant quantity is $\langle B \rangle$, *the average brightness experienced by a cell*. We compute the relation between $\langle B \rangle$ and B_{TH} (the measured brightness at the top of the holder) as follows. Let D_{BL} be the distance between the LED and the bottom of the liquid column in the vial. Let D_{TL} be the distance between the LED and the top of the liquid column in the vial. The distance from the top of the liquid column to the bottom is therefore $D_{TL} - D_{BL}$. Let D_{TH} be the distance between the LED and the top of the holder. $B(z)$, the brightness as a

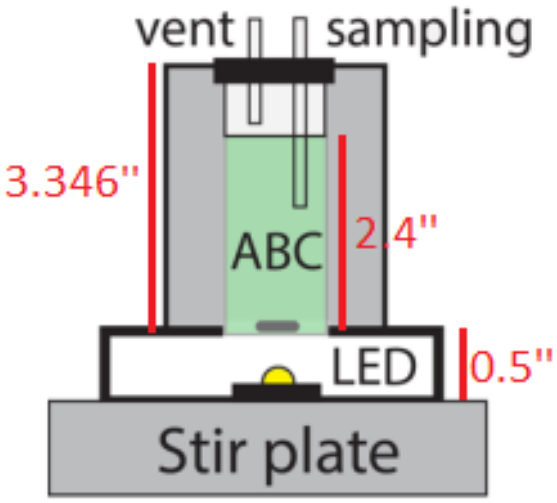

Figure A.12: Diagram of custom-culture device with relevant lengths pictured.

function of height z (where the LED is said to be at height $z = 0$) is then

$$B_{TH} \times (\frac{D_{TH}}{z})^2 \tag{A.1}$$

This function satisfies the two relevant contraints (1) that brightness go as $(\frac{1}{z})^2$ and (2) that $B(D_{TH}) = B_{TH}$. Assuming a cell spends equal time at each height in the liquid column, we can then use the integral formula for average and write

$$\langle B \rangle = \frac{1}{D_{TL} - D_{BL}} \int_{D_{BL}}^{D_{TL}} B(z)dz \tag{A.2}$$

Plugging in $B(z)$, we obtain

$$\langle B \rangle = \frac{1}{D_{TL} - D_{BL}} \int_{D_{BL}}^{D_{TL}} B_{TH}(\frac{D_{TH}}{z})^2 dz \tag{A.3}$$

From Fig. A.12, we can see that $D_{BL} = 0.5$, that $D_{TL} = 0.5 + 2.4 = 2.9$, and that $D_{TH} = 3.346 + 0.5 = 3.846$. Plugging in and solving, we find that $\langle B \rangle = 10 \times B_{TH}$. Whatever brightness you measure at the top of the holder, multiply by ten to obtain the average brightness experienced by a cell. The light levels of 1600 Lux and 4200 Lux reported in chapter 3 correspond to 160 and 420 Lux as measured from the top of the holder. For a time, I was also reporting these light levels as 640 and 1680 Lux respectively. Those numbers were derived from an attempt to calculate

the brightness at the middle of the vial, but we have since retired that convention in favor of reporting $\langle B \rangle$.

Appendix B

Protocols and recipes for ABC experiments

B.1 Invasion experiment protocol

This protocol tells how to do an invasion experiment, where bacteria are introduced at a later time. If one were doing a coculture experiment, one would simply not add bacteria or add bacteria at the beginning with the other organisms.

It is up to the experimentalist how often they want to perform flow cytometry and measure the abundances of each cell.

When the bacteria are washed before invasion, they are washed into 1/2x Taub Stripped, which has almost no nitrogen or carbon. They are washed into this stripped media to prevent growth. If they were growing, then their abundance would change significantly between the time that initial abundance is measured via flow cytometry and the time that they are put in the custom-culture device and the experiment is started. This precaution was taken for bacteria because bacteria grow much faster than the other organisms.

- Day i
    1. Start two cultures of algae in flasks in 25mL TAP each in the shaker incubator at 175RPM and 30C. Light is measured to be about 4000 Lux when light meter is placed at location of algae flask.
    2. Start two cultures of ciliates (the non-fluorescent strain, NOT the yfp-fluorescent strain) in 28mL SSP each in stationary 30C incubator.
- Day ii
    1. Make 1/2x Taub .01%pp3
    2. Make 1/2x Taub .03%pp3

- Day iii

    1. Autoclave vials with stir-bars. Place red luer pieces over sampling port before autoclaving to keep that port sterile. Filter is probably sufficient to relieve pressure build-up, but I loosen caps before autoclaving anyway.
    2. Test light levels on culture-devices to make sure they are programmed in right and as expected.

- Day iv (or Day 0)

    1. Wash algae into experimental media (1/2x Taub .01%pp3) twice.
        (a) Pipette 10mL of algae culture into a falcon tube
        (b) Centrifuge falcon tube for ten minutes at 500RCF
        (c) Immediately pour out supernatant
        (d) Immediately add 10mL of 1/2x Taub .01%pp3.
        (e) Repeat steps b-d
        (f) (Typically I will do two falcon tubes simultaneously)
    2. Wash ciliates into experimental media (1/2x Taub .01%pp3) twice.
        (a) Pipette 10mL of ciliate culture into a falcon tube
        (b) Centrifuge falcon tube for three minutes at 300RCF
        (c) Immediately pour out supernatant
        (d) Immediately add 10mL of 1/2x Taub .01%pp3.
        (e) Repeat steps b-d
        (f) (Typically I will do four falcon tubes simultaneously to maximize the number of cells I get in the end)
    3. Perform flow cytometry on falcon tubes and run code on flow data to calculate cell density
    4. Create master mixes
        – Master mixes are the cultures that one places in the custom-culture devices
        – Master mixes consist of ciliates, algae, or algae & ciliates (or bacteria if doing a coculture experiment rather than an invasion experiment)

- Densities are 500 cells/mL algae and 500 cells/mL ciliates (or 1000 cells/mL bacteria if doing a coculture experiment)
- Densities are obtained by combining falcon tubes with washed cells in correct proportion with 1/2x Taub .01%pp3.

5. In Biosafety Cabinet,
   (a) Add 30mL of master mix to each vial
   (b) Attach syringes to vials
6. Place vials in custom-culture devices
7. Start up python programs
8. Plate all relevant cultures to check for contamination

- Day 1
  1. Make 1/2x Taub Stripped
- Day 2
  1. Run flow cytometry on vials to measure cell abundance.
  2. Plate ns2yfp E. coli on an LB plate and place in 30C stationary incubator.
- Day 3
  1. From ns2yfp plate, inoculate two test tubes each with 5mL 1/2x Taub .03% pp3. Place test tubes in 30C shaker incubator.
- Day 4
  1. Wash bacteria into 1/2x Taub stripped.
     (a) Pipette 5mL of bacteria culture into a falcon tube
     (b) Centrifuge falcon tube for five minutes at max speed
     (c) Immediately pour out supernatant
     (d) Immediately add 5mL of 1/2x Taub stripped.
     (e) Repeat steps b-d
     (f) (Typically I will do two falcon tubes simultaneously)
  2. Run flow cytometry on vials as well as falcon tubes of bacteria to measure cell abundance

3. Make invasion master mix in the biosafety cabinet
   - Invasion master mix is the culture of bacteria that one invades into the custom-culture devices
   - There is some leeway in how to do this. What I would typically do is make an invasion master mix such that, when 500 μL of the invasion master mix is added to a vial, the concentration of bacteria in the vial would be 1000 cells/mL.
4. Invade the bacteria
   (a) Remove plastic cover from a needle and attach needle to a syringe and draw 500 μL from the invasion master mix into the syringe.
   (b) Re-place plastic needle cover on to needle.
   (c) Carry syringe into environmental room.
   (d) Remove needle, attach syringe to sampling port of a vial, and expel invasion master mix into vial.

- Day 5 and onward
  1. Run flow cytometry on vials to measure cell abundance.

B.2 Flow cytometry protocol

The following is a protocol for how to do a flow cytometry measurement for abundance once an experiment is up and running.

B.2.1 Sampling

1. Open a new syringe, leaving the syringe inside the package
2. Draw 500uL into syringe connected to sampling port luer
3. Unscrew syringe and screw in new syringe, being careful not to touch sampling port luer to anything (make sure to elevate sampling port luer before attaching new syringe so that any liquid in the tubing flows back into the vial)
4. Eject 500uL contents of syringe into an eppendorf tube
5. Repeat for all systems

B.2.2 Bring these items to flow cytometry building

- samples
- 200uL syringe and tips
- 1000uL syringe and tips
- fluorescent beads (Spherotech Accucount fluorescent beads ACFP-50-5, 5.0-5.9 μm)

B.2.3 Prepare samples

1. Transfer contents of each sample eppendorf to a labeled flow cytometry test tube (flow tube)
2. Fill a flow tube with 270uL each of distilled water
3. Vortex beads
4. Transfer 30uL of beads to the flow tube with water
5. Repeat b-d for two more flow tubes.

B.2.4 Prepare flow cytometer

1. Follow institutional instructions (refill sheath fluid, run water and bleach through the lines, run the qc beads, etc.)
2. Set the flow cytometer to maximum speed (Set speed to high and dial knob all the way clockwise)
3. Create file structure to house the data for the day.
    - In the parlance of flow cytometry, the "experiment" is a folder where every flow cytometry run within that folder has the same settings. In Fig. B.1, the experiment is "Settings2fire" (the word "fire" is extraneous, feel free to disregard it). Once you have set up an "experiment" folder, you never need to modify it again. On a monthly basis all the subfolders of an experiment will be deleted, but the experiment folder and its settings will remain intact.

The settings for Settings1 and Settings2 are depicted in Table B.1. I pretty much only used two experiment folders, Settings1fire and Settings2fire.

- A subfolder under the "experiment" folder is called a "specimen". The specimen folder will contain all the data for a given day with these settings. You are going to want to create a new specimen, or, on most days, just "duplicate without data" a previous specimen. Name the specimen by the data and the settings, for example, "0402_1600S2" to represent data taken on April 2nd at 4pm (which is 1600 in military time). This formatting will make the data work with the flow cytometry code.
- If you "duplicate without data" in the previous step you should be all set. However, if you made a new specimen, you will need to populate it with "tubes", the final kind of subfolder. Under settings2, name the tubes "Beads1", "Beads2", "Beads3", "V1", "V2", ... , "V8". Under settings1, do the same thing, but omit the beads folders. For each tube, set the "Stopping time" to 30 seconds, and max out the "Events to record" so that runs do not stop prematurely.

B.2.5 Run beads and samples

1. Run each of the beads flow tubes on Settings2, vortexing the tube before running.
2. Run each of V1 through V8 on Settings2, shaking the tube in hand before running.
3. Run each of V1 through V8 on Settings1, shaking the tube in hand before running.
4. Export the data as FCS2.0

B.3 Recipes

B.3.1 Stock Solutions for 1/2x Taub

Link to the original paper where they invented this media:

	Settings1 Voltage	Settings1 Log	Settings2 Voltage	Settings2 Log
FSC	203	No	400	No
SSC	203	Yes	250	Yes
GFP	350	Yes	501	Yes
PE	538	Yes	538	Yes
CHLOROPHYLL-A	176	Yes	176	Yes
CHLOROPHYLL-B	331	Yes	275	Yes
PACIFIC BLUE (CFP)	498	Yes	498	Yes
ALEXA FLUOR 700	719	Yes	500	Yes
PE-Cy7	809	Yes	500	Yes
APC	847	Yes	500	Yes

Table B.1: **Flow Cytometer Settings.** The voltages represent the gain of the detector for that scattering or fluorescence. The Log column represents whether the data is exported on a linear scale or on a log scale. Additional information: for settings1, the thresholds are 6000 FSC, 5000 SSC, and 200 Pacific Blue (CFP). The threshold is set to be an "or" gate meaning that if an object surpasses any of these thresholds, it will be logged. For settings2, the thresholds are 1000 FSC and 200 SSC, also with an "or" gate. Note that I do not believe this "or" gate actually functions properly on the machine and may actually act as an "and" gate.

https://aslopubs.onlinelibrary.wiley.com/doi/epdf/10.4319/lo.1964.9.1.0061

Solution B

- Dissolve 12.35 g MgSO4.7H2O in 500 mL ddH2O and autoclave

Solution C

1. Dissolve 6.80 g KH2PO4 and 1.60 g NaOH (careful!)(or 4mL of 10N NaOH) into 500 mL ddH2O
2. Adjust pH to 7.5 and autoclave

Solution D

- Dissolve 3.33 g CaCl2 (anhydrous, hygroscopic) into 100 mL ddH2O and autoclave
- OR dissolve 4.41 g CaCl2.2H2O in 100 mL ddH2O and autoclave

Solution F

1. Dissolve 26.1 g EDTA into 268 mL 1M NaOH
2. Add 24.9 g FeSO4.7H2O and bring volume to 1 L with ddH2O
3. Aerate overnight in chemical hood (cap loose and stirring)

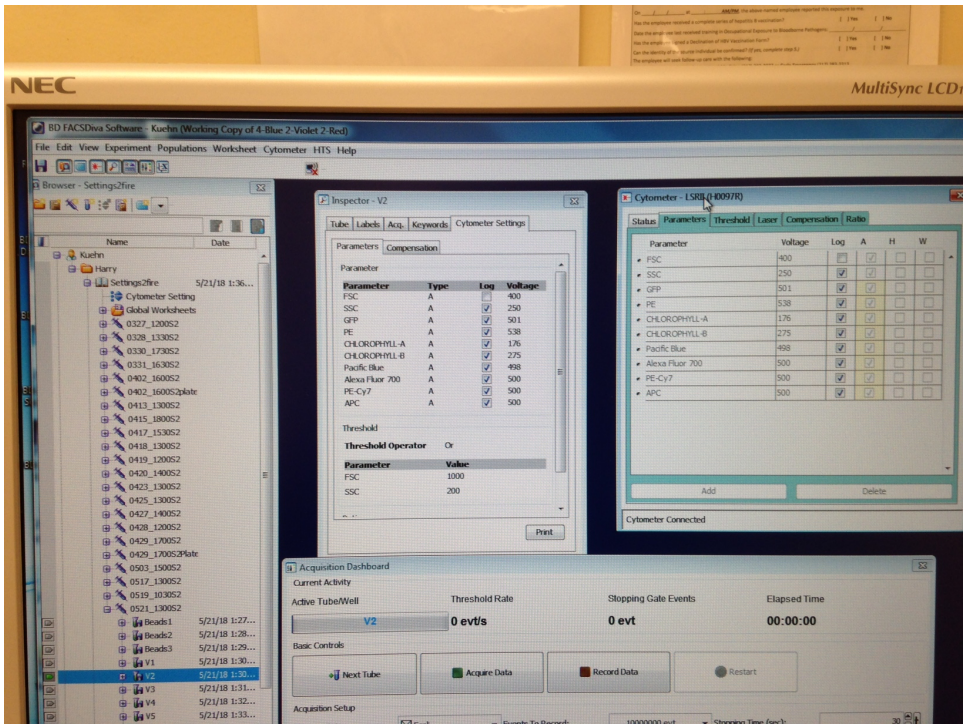

Figure B.1: **Screenshot during flow cytometry**

4. Filter sterilize and store at room temperature shielded from light

5. In the dark the solution appears stable for at least a year

Solution G

Dissolve sequentially in 1 L ddH2O:

1. H3BO3 1.854 g

2. ZnSO4.7H2O 0.287 g

3. MnCl2.4H2O 1.36 g (or 1.98 g MnCl2.9H2O)

4. Na2MoO4.2H2O 0.242 g

5. CuSO4.5H2O 0.0499 g

6. Co(NO3)2.6H2O 0.291 g

7. Filter sterilize and store at room temperature, shielded from light

B.3.2 1/2x Taub .01% pp3

This recipe is specifically for making 1/2x Taub with .01% proteose peptone 3 (pp3). To make media with other concentrations of pp3, adjust amount of pp3 added accordingly.

First make 1x Taub

1. 1.5 mL of 1M NaCl
2. 1.0 mL Solution B
3. 1.0 mL Solution C
4. 0.5 mL Solution G
5. Bring it up to 500 mL and autoclave
6. 3.33 mL Solution D
7. 62.5 uL Solution F
8. filter

Then make unsterile 1% pp3 in H2O

1. 100 mL ddH2O
2. 1 gram pp3

Finally make 1/2x Taub .01% pp3

1. 250 mL 1x Taub
2. 245 mL ddH2O
3. 5 mL unsterile 1% pp3 in H2O
4. Bring pH to 7
5. Filter

B.3.3 1/2x Taub Stripped

1/2x Taub Stripped is used for washing organisms when one does not want them to grow after washing. It has almost no carbon or nitrogen.
First make 1x Taub Stripped

1. 1.5 mL of 1M NaCl
2. .5 mL Solution G
3. Bring it up to 500 mL and autoclave
4. 3.33 mL Solution D
5. 62.5 uL Solution F
6. filter

Then make 1/2x Taub Stripped

1. 250 mL 1x TaubStripped
2. 250 mL ddH2O
3. Bring pH to 7
4. Filter

B.3.4 TAP

2X Filners Beijernicks Solution

1. NH4Cl 8.0 g
2. CaCl2.2H2O 1.0 g
3. MgSO4.7H2O 2.0 g
4. Bring to 500 mL and autoclave. Store at 4 Celsius

Trace Mineral Solution

1. Dissolve 5 g of disodium EDTA in 400 mL water by heating and stirring
2. Neutralize to pH 6.5 with 5N NaOH

3. Add each of the following in order. Allow each to dissolve completely before adding the next

   (a) FeSO4.7H2O 0.5 g

   (b) ZnSO4.7H2O 2.2 g

   (c) H3BO3 1.14 g

   (d) MnCl2.4H2O 0.51 g

   (e) CuSO4.5H2O .016 g

   (f) Na2MoO4.2H2O .073 g

   Co(NO3)2.6H2O .0196 g

4. Bring to 500 mL and autoclave. Solution should be pale green, turning deep orange to purple upon storage.

1M Potassium Phosphate Stock

1. KH2PO4 6.8 g
2. K2HPO4 8.7 g
3. Bring volume to 50 mL and autoclave

TAP (Tris-Acetate-Phosphate)

1. 2X Filners Beijernicks Solution 12.5 mL
2. 1M Potassium Phosphate 0.5 mL
3. Trace mineral solution 2.5 mL
4. Tris-Base 1.21 g
5. Glacial Acetic Acid (use gloves and perform in fume hood) 0.5 mL
6. Bring to 500 mL, adjust pH to 7.2, and autoclave. Store at room temperature

B.3.5 SPP

This recipe calls for sequestrene. After many online searches I am still not sure what that ingredient is. I read in one place that it is EDTA ferric salt and so I decided to use my EDTA ferric sodium salt and it works fine.
Sequestrene stock

- Dissolve 0.6 grams sequestrene in 100mL ddH2O

SPP

1. proteose peptone (regular kind) 5 g
2. yeast extract 0.5 g
3. glucose 1 g
4. sequestrene stock 2.5mL
5. Fill to 500 mL and autoclave

Appendix C

Protocol for tracking *E. coli*

C.1 Brief Protocol

Supplies needed include

- 50 mL centrifuge tubes
- 25 mL pipettes
- Large filters
- Small filters
- PDMS
- weighing boats
- 3mL syringes
- acetone
- isopropanol
- cover slips

C.1.1 Day 1

Start microfluidics baking

C.1.2 Day 2

1. Remove microfluidics from oven
2. Make microfluidics

3. Autoclave
    - LB
    - setup, ensure there is a stir-bar in the vial, and caps are attached to bottles
    - extra 500 mL bottle
4. Make 25 mL of 1% BSA (if there is no stock available)
5. Make about 450 mL of .1% BSA
6. Remove 25 mL of .1% BSA for experiment day
7. Ethanol valve and attach to setup
8. Attach setup to pumps
9. Late at night
    (a) Turn on electronics box and plug in stir plate
    (b) Engage makePumpsGo script to fill vial with .1% BSA
    (c) Mark microfluidics for quality
    (d) Inoculate vial and start turbidostat code
    (e) After several minutes start code again with proper setpoint

C.1.3 Day 3

1. Soak eight microfluidics in 1% BSA for one hour
2. Set proper settings on program
3. Perform experiment!

C.1.4 Day 4

Clean setup!

C.2 Extended Protocol

C.2.1 Day 1

Starting microfluidics baking

1. Combine 40 grams from large PDMS bottle and 4 grams from small PDMS bottle in weighing boat
2. Mix well, stirring for at least 45 seconds
3. Place foil on top and vacuum in bell vacuum for at least 3 hours
4. Attach microfluidic wafer to PVC pipe with masking tape
5. Remove PDMS from vacuum and pour into PVC/wafer
6. Use pipette to move air bubbles that lay directly over chamber if necessary
7. Place foil over PVC/wafer and bake at 100 degrees Celsius over night

C.2.2 Day 2

Preparing PDMS portion of microfluidics

1. Remove PVC/wafer from oven and let cool for one hour
2. Remove PDMS from PVC/wafer
3. Cut PDMS into separate microfluidic devices
4. Punch two holes into each microfluidic device with biopsy punch on rubber stopper

Finishing microfluidics

1. Bring devices, scotch tape, scissors, tweezers, and cover slips to Clegg room
2. Wear gloves for this
3. Prepare coverslips
   (a) Rinse a cover slip with acetone, IPA, DI water, then IPA again
   (b) Dry with nitrogen from fume hood

(c) Place coverslip in plasma cleaner

(d) Do this 3x

4. Prepare PDMS devices

(a) Attach scotch tape to both sides of PDMS device, then pull off

(b) Rinse with IPA, DI water, then IPA again (no acetone)

(c) Dry with nitrogen from fume hood

(d) Cut out small triangle of tape and place directly over chamber of device with tweezers

(e) Place PDMS device in plasmas cleaner with design facing UP

(f) Do this 3x

5. Plasma Bond, the order of operations here is EXTREMELY important, if pumps are turned on or off in the wrong order vacuum grease will be sucked into the plasma cleaner

(a) Close door to plasma cleaner and tighten valve all the wafer

(b) Flip on pump on plasma cleaner

(c) Flip blue lever on external pump

(d) Flip on power on plasma cleaner

(e) Flip RF level to low

(f) After a few seconds, the inside of the plasma cleaner turns purple. When this happens start a timer for 90 seconds.

(g) Sometimes the plasma cleaner will become visually less purple over the course of the 90 seconds, a quick shot of air by slightly loosening and then tightening the valve will reinvigorate the plasma

(h) When timer finishes, flip buttons in opposite order (RF level, power, blue lever, pump on plasma cleaner)

(i) Open valve and let air rush into plasma cleaner

(j) Open door

(k) Remove a PDMS device and remove tape with tweezers

(l) Remove each coverslip and place active side on active side of PDMS device (they should bond)

6. Repeat all steps until all nine of your devices are bonded

Preparing setup

1. Connect all the tubes and bottles of the setup
   - Orange cap with long hanging tube ->pump element->short peak tubing in green cap
   - Orange cap with short tube ->extra luer for valve->pump element->long peak tubing green cap
   - Place stir-bar in vial
   - Attach green cap to vial and 500 mL bottles to the two orange caps
   - Do not attach valve yet (it breaks in the autoclave)
2. Add together ingredients for 500 mL of LB into a 500 mL bottle
3. Autoclave
   - The LB you just made
   - The setup
   - Extra 500 mL bottle
4. Use LB to make 25 mL of 1% BSA in LB
   (a) Wait for LB to cool down before doing so (heat degrades BSA)
   (b) Filter sterilize after adding BSA
   (c) Refrigerate it (heat degrades BSA)
   (d) This will be enough to have some left over for future experiments
5. Use rest of LB to make about 475 mL of .1% BSA
6. Remove about 25 mL of .1% BSA for later use
7. Unscrew long-tube orange cap from empty bottle and transfer to bottle of .1% BSA in LB

8. Sterilize valve in ethanol and attach to setup
    - If luers are too tight to unscrew, use pliers
    - Set valve such that fluid would flow from vial to bottle and not out of valve
9. Tighten all connections in setup
10. Attach setup to pumps and turbidostat
    - Tube element from bottle of .1% BSA in LB goes to I-Pump
    - Tube element from empty bottle goes to O-Pump
    - Ensure directionality of tubes in pumps is correct
11. Turn on electronics box and plug in stir-plate
12. Fill vial with .1% BSA in LB
    (a) Open python and run makePumpsGo
    (b) Pumps will turn on after 120 seconds
    (c) Wait for fluid level to reach the longer peak tubing
    (d) While waiting you can look at microfluidics under microscope and mark quality
    (e) Close python in that split second when both pumps have stopped (otherwise pumps will keep running even after program stops)
    (f) Unplug stir-plate
    (g) Turn off electronics box (turn off box whenever no program is running, otherwise setup might heat or cool to its limit)

Late at night, inoculating bacteria culture and turbidostat

1. Inoculate bacteria
    (a) Remove bacteria from freezer
    (b) Place in box of ice and leave in environmental room
    (c) Sterilize inoculation loop in 389
    (d) Carry inoculation loop into environmental room

(e) Inoculate bacteria into vial of .1% BSA in LB (be careful not to touch peek tubing to anything)

2. Plug in stir-plate and turn on electronics box
3. Start turbidostat running
4. Open python and start "20141117_turbidostat" program
5. Wait ten minutes for OD reading to stabilize
6. Open up spreadsheet with log of the OD
   (a) Its in Documents-¿Python Scripts-¿JasonPython-¿folder with date
   (b) Take note of what OD the the system has stabilized at
   (c) Subtract .2 from that number
   (d) Enter value into the "odThreshold" field of the turbidostat program
7. Hit go on the program!

C.2.3 Day3

Preparation

1. Soak eight microfluidics in 1% BSA in LB for one hour
   (a) Do this in 389
   (b) Attach 5 mL syringe to pink needle tube
   (c) Fill 5 mL syringe with 1% BSA in LB
   (d) Depress plunger until first drop of fluid comes out of pink needle
   (e) Stab needle into microfluidic hole
   (f) Depress plunger until fluid comes up out of other hole
   (g) Stab empty pink needle tube needle into other hole (Make sure valve is not closed on this one)
   (h) Depress plunger until fluid enters a few inches into the tube of the second pink needle tube

(i) Remove syringe and close both valves

(j) The syringe does not need to be refilled before each microfluidic

2. Prepare microscopes and files on computer

(a) Do this while microfluidics are soaking

(b) Plug in illumination source on microscope

(c) Copy and paste empty round/trial folder structure to intended file location

(d) Open flyCapture

(e) Optimize camera settings (Settings-¿Toggle Camera Control Dialog)

i. Custom Video Modes: Make width and height 1300, increase packet size if it turns red, click apply

ii. Camera Settings: Uncheck auto for all fields, set shutter to 1.7, set gain to 0, set fps to 30 (may need to increase packet size if cant do this)

(f) Set recording parameters (red circle button)

i. Click browse and go to location of first video (Round 1 Trial 1)

ii. Set to 9000 frames

iii. Recording mode should already be set to buffered

iv. Change tab from Images to Videos

v. Set Video Recording Type to M-JPEG

vi. Click Use Camera Frame Rate

3. Move switch on vial so that bacteria comes out and place beaker underneath

Performing experiment

1. Bring soaked microfluidic into environmental room.

2. Remove pink needle tubes from microfluidic

3. Eject fluid from pink needle tubes with 3 mL syringe

4. Attach same 3 mL syringe to same pink needle tube

(a) Fill with 750 uL of sterile .1% BSA in LB

(b) Add one drop of bacteria from vial

(c) Replace plunger, but leave a half centimeter of air

5. Pump diluted bacteria into microfluidic until moves two inches into other pink needle tube
6. Put microfluidic on microscope and tape pink needle tubes
7. Adjust stage and focus until chamber is centered on video
8. Pump plunger and pull back until one or two reasonably swimming bacteria are trapped
9. Close valve on pink needle tube without syringe
10. Click start recording (be careful of bumping table while videos are recording)
11. The same syringe of bacteria can be used for five videos (Trials one through five), just open valve on second pink needle tube before pumping more bacteria into chamber
12. Perform eight rounds of the experiment on each microscope (may need to switch out microfluidic every few rounds)

Thank you for reading.